The electron microprobe flank method: A fresh approach to Fe^{3+} quantification in tourmalines

Eva Mrkusová[1*], Radek Škoda[1], Jan Filip[2]

[1] Department of Geological Sciences, Faculty of Science, Masaryk University, Kotlářská 2, 611 37 Brno, Czech Republic
[2]Czech Advanced Technology and Research Institute (CATRIN), Palacký University in Olomouc, Šlechtitelů 27, 783 71 Olomouc, Czech Republic
*Corresponding author: 484435@mail.muni.cz

Ferrous and ferric ions are common in several tourmaline species from various rock types reflecting the oxidation-reduction conditions during the crystallization. Iron enters the tourmaline structure in both the Y and Z octahedral positions, with Fe^{2+} preferentially occupying the Y position, whereas Fe^{3+} is more compatible with the Z position (e.g. Dyar et al. 1998). Quantifying $Fe^{3+}/\Sigma Fe$ in iron-bearing tourmalines is crucial for mineralogical, geochemical and petrological studies. Quantification of the iron valence state is essential for accurately estimating the hydrogen content in tourmaline and for correct mineral identification. Precision in quantifying the iron valence state leads to more accurate derivations of other petrological variables, such as pressure, temperature, $fO2$, or pH. Incomplete or limited chemical analysis of tourmalines can result in incorrect conclusions or misinterpretation of formation conditions.

The electron probe microanalyzer (EPMA) is a widely accessible tool for elemental analysis in geosciences; however, it does not directly provide information on the oxidation state of transition metals. The flank method, pioneered by Höfer et al. (1994), Höfer (2002) and Höfer and Brey (2007), and initially applied on garnets, serves as an analytical tool developed for quantitative determination of the Fe oxidation state in solid phases using EPMA. It utilizes the shift in peak positions and differences in the Fe$L\alpha$ and Fe$L\beta$ intensities as functions of the total iron content and $Fe^{3+}/\Sigma Fe$ ratio. The measured emission spectra of Fe$L\alpha$ and $L\beta$ peaks for Fe^{2+} differ from those for Fe^{3+} due to variations in the crystallographic environment, including bond types and coordination polyhedra, and distinct absorption edge positions. The method relies on measuring X-ray intensities in differential mode at specific spectral positions (Fe$L\alpha$ a Fe$L\beta$ flank) using a TAP monochromator, targeting the regions with the most pronounced differences between X-ray spectra of Fe^{2+} and Fe^{3+} phases.

Two types of well-characterized tourmaline samples were selected for this study: 1) calibration standards: chemically homogeneous tourmalines used to establish the calibration space for the flank method; 2) control samples: series of natural tourmalines with known and varying Fe^{3+} and FeO_{tot} contents, used to verify the accuracy of the developed calibration and the dependence relationship.

Tourmaline calibration standards were chosen to have a minimal Fe^{2+} and cover the range from ~7 to ~20 wt.% FeO_{tot}. Their crystals were cut in half perpendicular to the c-axis, with one half annealed in air atmosphere to fully oxidize Fe^{2+} to Fe^{3+} (Filip et al. 2012). The content of Fe^{3+} in standards was determined by Mössbauer spectroscopy (MS) and revealed ≤6.5 rel.% of Fe^{3+} in natural standards and 100 rel.% of Fe^{3+} in annealed ones. The calibration of the flank method is based on measurement of Fe$L\alpha$/Fe$L\beta$ flank X-ray intensities ratio on natural tourmaline calibration standards with low or no Fe^{3+} content and on their annealed fully oxidized equivalents. An accelerating voltage of 15 kV, beam current of 50 nA and 30x22.5 μm area were selected as optimal analytical conditions. The equation for $Fe^{3+}/\sum Fe$ calculation was derived from the parameters defining the calibration space for the tourmalines.

Natural tourmaline control samples with known $Fe^{3+}/\sum Fe$ ratios, were analyzed to assess the reliability of the method. X-ray intensities at flank positions and chemical compositions were measured at seven points per sample, table present the means of X-ray $L\alpha/L\beta$ flank intensities ratio per sample and the means of $Fe^{3+}/\Sigma Fe$ ratios calculated from the established equation for the flank method. The calculated values were compared with MS data, and the absolute error, assessing the accuracy of the flank method, was determined as the difference between the calculated results and the MS data. For the control samples with up to ~10 wt.% FeO_{tot}, the absolute error does not exceed 6 abs.% of Fe^{3+}. As the FeO_{tot} content increases, the absolute error decreases. An error 3-4 abs.% $Fe^{3+}$is typical for samples with

~13-19 wt.% FeO_{tot} and does not exceed 1 abs.% for sample with ~20 wt.% FeO_{tot}. The developed methodology for determining the iron oxidation state in tourmaline-supergroup minerals is most reliable for tourmalines with >5 wt.% FeO_{tot}.

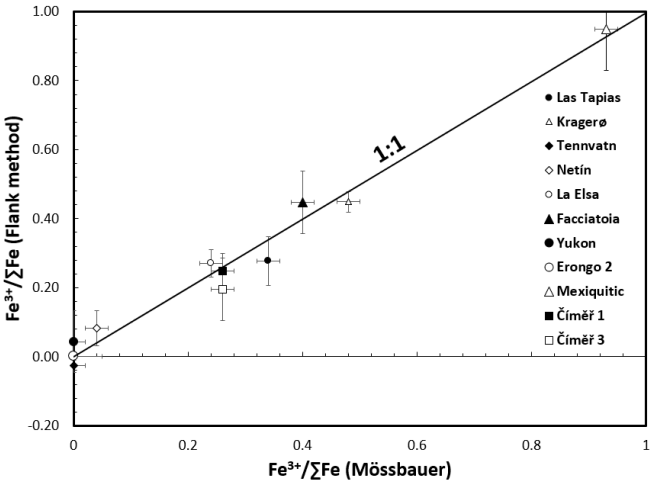

Comparison of the $Fe^{3+}/\Sigma Fe$ calculations via derived equation for the flank method with MS data.

Flank method is a non-destructive tool allowing to study small objects and also monitoring the changes in the oxidation state of Fe during tourmaline crystal growth. The iron oxidation state can be estimated with microscale spatial resolution in thin section in combination with chemical WDS or EDS in situ analysis.

References

Dyar, M. D., Taylor, M. E., Lutz, T. M., Francis, C. A., Guidotti, C. V., and Wise, M. (1998) - Inclusive chemical characterization of tourmaline; Mossbauer study of Fe valence and site occupancy. *American mineralogist*, 83(7-8), 848-864.

Filip, J., Bosi, F., Novák, M., Skogby, H., Tuček, J., Čuda, J., and Wildner, M. (2012) - Iron redox reactions in the tourmaline structure: High-temperature treatment of Fe3+-rich schorl. *Geochimica et Cosmochimica Acta*, 86, 239-256.

Höfer, H. E., Brey, G. P., Schulz-Dobrick, B., and Oberhaensli, R. (1994) - The determination of the oxidation state of iron by the electron microprobe. *European Journal of Mineralogy*, *6*(3), 407-418.

Höfer, H. E., Weinbruch, S., Mccammon, C. A., and Brey, G. P. (2000) - Comparison of two electron probe microanalysis techniques to determine ferric iron in synthetic wüstite samples. *European Journal of Mineralogy*, 12(1), 63-71.

Höfer, H. E., and Brey, G. P. (2007) - The iron oxidation state of garnet by electron microprobe: Its determination with the flank method combined with major-element analysis. *American Mineralogist*, 92(5-6), 873-885.

Acknowledgement: This work was supported by research project MUNI/A/1725/2024. Thank to Prof. Ferdinando Bosi, PhD. (Department of Earth Sciences Sapienza University, Rome, Italy), and Prof. RNDr. Milan Novák, CSc. (Department of Geological Sciences, Masaryk University, Brno, Czech Republic) for providing samples and MS data.

Cu isotope composition of Paraíba tourmaline indicates hydrothermal processes follow pegmatite crystallization

Sarah E. Brooker*[1], Kenneth S. Befus[1], Ryan Mathur[2], Barbara L. Dutrow[3], Jaime D. Barnes[1]

[1]Department of Earth and Planetary Sciences, University of Texas at Austin, Austin, TX 78712, USA
[2]Department of Geological Sciences, Juniata College, Huntingdon, PA 16652, USA
[3]Department of Geology and Geophysics, Louisiana State University, Baton Rouge, LA 70803, USA
*Corresponding author: sbrooker@utexas.edu

Pegmatite crystallization is complex and commonly enigmatic, with the relative contributions of magmatic processes versus hydrothermal fluids remaining uncertain. Stable isotope measurements of pegmatite minerals offer a method to recognize if crystallization occurred from evolved magma or from hydrothermal fluids. Such isotopic data can be used to address outstanding geologic questions regarding mineral growth and geochemical diversity. Isotopic data may also help economic geologists recognize which pegmatite systems may be prospects for further development as hydrothermal fluids can mobilize metals and potentially enrich pegmatites. Cu stable isotopes are a discriminating geochemical tracer in various applications, including to describe fluid processes in Cu porphyry deposits (i.e., Larson et al., 2003).

Cu isotopes fractionate significantly during oxidation and reduction reactions associated with the precipitation and dissolution of hydrothermal sulfide minerals (e.g. chalcopyrite). Precipitation and dissolution in hydrothermal environments produce large fractionations that range up to 25‰. In contrast, studies have found that magmatic processes are inefficient at fractionating Cu isotopes (i.e., Sullivan et al., 2022 and references therein). Ultramafic (δ^{65}Cu = +0.11 ± 0.28‰), mafic (δ^{65}Cu = +0.09 ± 0.10‰), intermediate (δ^{65}Cu = +0.10 ± 0.16‰), and felsic (δ^{65}Cu = +0.01 ± 0.15‰) igneous rocks are indistinguishable from the bulk silicate earth (δ^{65}Cu = +0.07 ± 0.10‰). Magmatic differentiation and crystallization have little to no impact on the Cu stable isotope composition.

Given the significant fractionation of Cu isotopes in hydrothermal systems, and its homogeneity in magmatic systems, Cu isotopes in Paraíba tourmaline may provide insights into their origin. Paraíba tourmaline is a rare Cu-bearing variety of elbaite (fluor-elbaite or the rarer liddicoatite), which is known for a vivid electric blue to green color produced by Cu (Dutrow et al. 2024). These stones are of significance to the gem trade. The geologic source of Cu in these tourmalines remains unresolved largely. Studies speculate on either Cu-enriched melt or hydrothermal fluids as a Cu source (i.e., Wilson, 2002). By analyzing the Cu stable isotope composition in Paraíba tourmaline from Brazil, Mozambique, and Nigeria, we aim to investigate the processes responsible for Cu that is available for incorporation into the elbaite. Our results identify the source of Cu and provide insight into pegmatite mineralization driven by secondary processes.

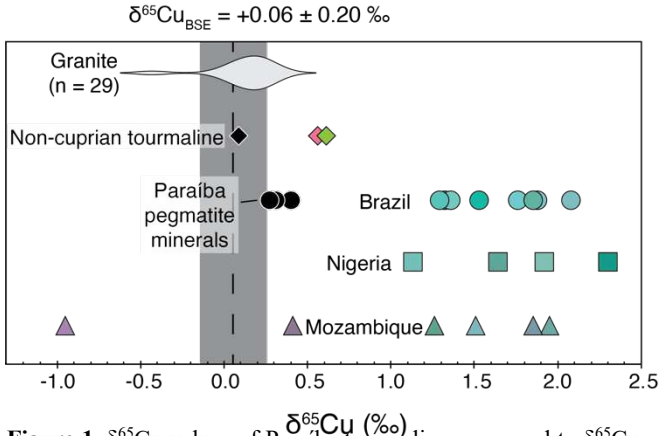

Figure 1. δ^{65}Cu values of Paraíba tourmaline compared to δ^{65}Cu values of Paraíba pegmatite minerals, non-cuprian tourmaline, from this study and granites from Li et al. (2009). Symbol color is representative of sample color.

Eighteen samples of Paraíba tourmaline from the 3 localities have been analyzed. Also analyzed were four samples of non-cuprian tourmaline, the sulfide bismuthanite and the mica lepidolite, from Paraíba-bearing Borborema pegmatites from Brazil. All samples were crushed and dissolved for ion chromatography, and were then analyzed for their Cu isotope compositions using a MC-ICP-MS. The δ^{65}Cu values of the blue to blue/green Paraíba tourmaline from all three localities range from +1.13‰ to +2.30‰, with an average of +1.66 ± 0.34‰ (1σ; n = 16; Fig. 1). Values from each geographic locality are indistinguishable from one another. Two samples of pink/purple-pink from Mozambique have much lower δ^{65}Cu values than those of blue to blue/green Paraíba tourmalines (-0.95‰ and +0.41‰). The Cu isotope composition of non-cuprian tourmaline ranges from +0.09 to +0.61‰ with an average of +0.41 ± 0.23‰ (1σ; n = 4; Fig. 1; Table 1), much lower than values of the blue to blue/green Paraíba tourmalines. Borborema pegmatite minerals have much lower δ^{65}Cu values than the Paraíba tourmaline taken from the same sample (e.g., +0.32 ± 0.07‰ and +2.07‰, respectively; Table 1).

Table 1. Cu isotope composition of non-cuprian minerals.

Mineral	δ^{65}Cu (‰)
Borborema Pegmatite Minerals	
Schorl	+0.39
Bismuthanite	+0.26
Lepidolite	+0.30
Cuprian elbaite	**+2.07**
Non-cuprian tourmaline	
Schorl (Erongo, Namibia)	+0.09
Elbaite (green, Himalaya, CA)	+0.61
Elbaite (pink, Himalaya, CA)	+0.56

The δ^{65}Cu values of the blue to blue/green Paraíba tourmaline from all locations exhibit a considerable range distinctly higher than those of non-cuprian magmatic tourmaline, mineral phases in the Paraíba pegmatite, and granites (Fig. 1). This discrepancy suggests that the Cu in Paraíba tourmaline is not associated with a Cu-enriched granitic magma. Instead, the higher δ^{65}Cu values of the blue to blue/green Paraíba tourmaline likely reflects a hydrothermal process. Partial sulfide dissolution in an oxidizing environment preferentially releases ^{65}Cu in the fluid phase, resulting in hydrothermal waters with elevated δ^{65}Cu values (e.g., Mathur et al. 2005). This study suggests that the Cu in the Paraíba tourmalines was incorporated from such hydrothermal fluids, perhaps released from chalcopyrite in the local host quartzites. These pegmatites are all hosted within the discontinuous Equador Formation, a Neoproterozoic unit of mica-rich quartzites and metaconglomerates. Cu isotopes provide evidence for the presence of hydrothermal fluids in the crystallization of Paraíba tourmaline, offering new insights into late-stage mechanisms active during pegmatite evolution. The source, timing, and extent of the fluid responsible for the observed isotopic differences between pink and blue tourmaline remain unknown, leaving open whether they reflect distinct crystallization episodes, changing fluid conditions, or metasomatic overprint.

References

Dutrow, B., et al., (2024) – A multivariate statistical approach for mineral geographic provenance determination using laser-induced breakdown spectroscopy and electron microprobe chemical data: A case study of copper-bearing tourmalines, *American Mineralogist*, v.109, p. 1085-1095.

Larson, P., et al., (2003) – Copper isotope ratios in magmatic and hydrothermal ore-forming environments, *Chemical Geology*, v. 201, 337–350.

Li, W., et al., (2009) – The Cu isotopic signature of granites from the Lachlan Fold Belt, SE Australia: *Chemical Geology*, v. 258, p. 38-49.

Mathur, R., et al., (2005) – Cu isotopic fractionation in the supergene environment with and without bacteria, *Geochimica et Cosmochimica Acta*, v. 69 (22), 5233-5246.

Sullivan, K., et al., (2022) – Emerging applications of high-precision Cu isotopic analysis by MC-ICP-MS, *Science of The Total Environment*, v. 838, 156084.

Wilson, W. (2002) – Cuprian elbaite from the Batalha Mine, Paraiba, Brazil: *Mineralogical Record*, v. 33, p. 127–137.

Boron sources of tourmaline-rich Nb-Y-F-pegmatites in south Norway: Implications for pegmatite melt origin

E. De La Cruz[1], A. Müller[1,*], R.B. Trumbull[2], P. Faria[1], T. Andersen[1,3], M. Erambert[4], M. Kristoffersen[4]

[1] Natural History Museum, University of Oslo, PO Box 1172 Blindern, N-0318 Oslo, Norway
[2] GFZ German Research Centre for Geosciences, Telegrafenberg, 14473 Potsdam, Germany
[3] University of Johannesburg, Department of Geology, PO Box 524, Auckland Park, 2006 Johannesburg, South Africa
[4] University of Oslo, Department of Geosciences, P.O. Box 1047 Blindern, 0316 Oslo, Norway
*Corresponding author: a.b.muller@nhm.uio.no

Tourmaline is the most prevalent borosilicate mineral in the Earth's crust and serves as the primary mineral host for boron (B) in most rocks. During hydrothermal processes or partial melting, B is preferentially partitioned into fluid or melt phases, resulting in distinct B isotopic signatures due to fractionation of the two stable isotopes ^{11}B and ^{10}B between coexisting phases. Consequently, the chemical composition and B isotopic signatures of tourmaline formed from these fluids and melts are increasingly utilized to trace the origins, pathways, and interactions of the aqueous fluids and/or melts related to orogenic processes and ore formation (e.g. Marschall et al., 2011; Trumbull and Slack, 2018).

Tourmaline is common in rare element pegmatites of the Nb-Y-F (NYF) type of the Bamble, Kongsberg and Idefjorden lithologic units in the south-central part of the Proterozoic Sveconorwegian orogen in southern Norway. In the global context, however, tourmaline appears rare in this type of pegmatite and is much more abundant in Li-Cs-Ta (LCT) pegmatites. Consequently, the Norwegian occurrences raise important general questions about B sources and B enrichment in this family of pegmatites and this has motivated the present study. This study aims to explain the unusual tourmaline abundance in these pegmatites and the origin of B in the respective melts, and to raise awareness of tourmaline in NYF pegmatites generally. Tourmalines from six pegmatites in three Sveconorwegian lithotectonic units: Bamble, Kongsberg and Idefjorden, were investigated in terms of their tourmaline chemistry and $\delta^{11}B$ values, in addition to bulk rock analyses of pegmatites and host rocks. Recent studies have suggested that most of the Sveconorwegian rare-element pegmatites derived from partial melting (anatexis) of their host rocks rather than fractionation of a parental granite. Indeed, within our study areas of Bamble, Modum and Nesodden most tourmaline-bearing NYF pegmatites occur where no coeval granite pluton is exposed. By constraining the B source in the Sveconorwegian NYF pegmatites with complementary whole rock and mineral chemistry data, this tourmaline study also sheds light on the idea of an anatectic origin for the pegmatite melts.

The B-isotope values of tourmaline from the investigated Sveconorwegian pegmatites show a high variability overall. However, the value ranges for samples from individual lithologic units (Bamble, Kongsberg and Idefjorden) are relatively narrow and regionally distinct (Figure 1). Importantly, only the pegmatite at Spro of the Idefjorden unit has tourmaline with a negative B-isotopic signature typical for the continental crust and S-type granites (− 13.8 to − 12.5 ‰) and in good agreement with the host rock gneiss (− 14.8 to − 12.9 ‰). Tourmalines from all other pegmatites of the Bamble and Kongsberg lithologic units have much heavier isotope signatures (− 1.9 to + 9.9 ‰) than either the continental crust or unaltered MORB and the upper mantle. Such heavy isotope signatures are typical for a marine-related B source. Thus, B sources are different for pegmatites in different Sveconorwegian lithologic units. The heavy B-isotope signature observed in the Bamble and Kongsberg lithologic units was most likely inherited from the Na-metasomatised source rocks. Regional fluid plumes in these units, sourced from metamorphic dehydration of Mesoproterozoic shallow marine sediments at greater depth, caused hydration in permeable lithologies and along fault zones over large areas of the basement prior to pegmatite formation. We suggest that the marine source of hydration fluids caused the heavy B-isotope composition of pegmatite melts. This is supported by previously published $\delta^{11}B$ ratios from metasomatized Bamble host rocks (Bast et al., 2014). Furthermore, the metasomatism enhanced partial melting of the affected rocks, which explains the preferential occurrence of Kragerø and Modum pegmatites in areas with Na-metasomatism.

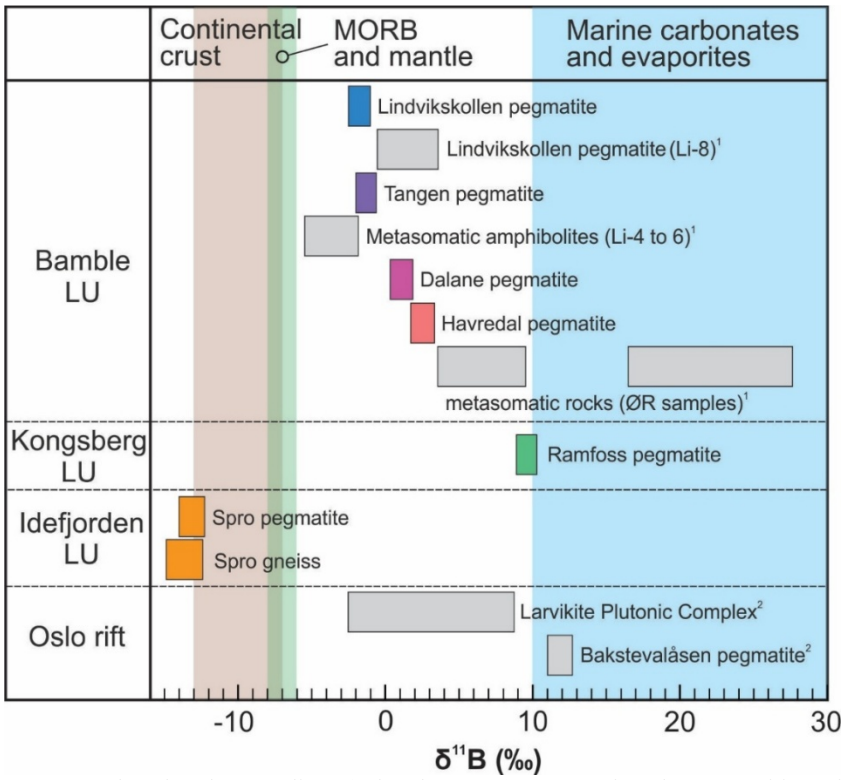

Figure 1. $\delta^{11}B$ value ranges of analysed tourmalines (colored squares) compared to the composition of different B source reservoirs (continental crust and marine evaporates: Van Hinsberg et al. (2011); MORB and mantle: Marschall, 2018) and to published $\delta^{11}B$ data from the Sveconorwegian Bamble lithotectonic unit and the Permian Oslo rift (grey squares): [1] Bast et al. (2014) and [2] Sunde et al. (2020), respectively. LU- Lithotectonic unit. From De La Cruz et al. (2024).

Our findings reveal an additional significant occurrence of tourmaline in NYF-type pegmatites, supplementing the few that have been recently documented. This suggests that tourmaline may be more widespread, and that B enrichment could play a more critical role in the formation of NYF-type pegmatites than previously thought. This study, along with similar research affirms that tourmaline can be a valuable mineral for assessing genetic models not only of LCT pegmatites, where it has typically been studied, but also of NYF pegmatites.

References

Bast, R., Scherer, E.E., Mezger, K., Austrheim, H., Ludwig, T., Marschall, H.R., Putnis, A. and Löwen, K. (2014) - Boron isotopes in tourmaline as a tracer of metasomatic processes in the Bamble sector of Southern Norway. *Contributions to Mineralogy and Petrology*, 168, 1069.

De La Cruz, E., Müller, A., Trumbull, R.B., Faria, P., Andersen, T., Erambert, M. and Kristoffersen, M. (2024) - Boron sources of tourmaline-rich Nb-Y-F-pegmatites in south Norway: Implications for pegmatite melt origin. *Precambrian Research*, 410, 107474.

Marschall, H.R. and Jiang, S.-Y. (2011) - Tourmaline isotopes: No element left behind. *Elements*, 7, 313–319.

Marschall, H.R. (2018) - Boron isotopes in the ocean floor realm and the mantle. In: Marschall, H. and Foster, G. (Eds.) Boron Isotopes – The Fifth Element. Advances in Geochemistry, vol. 7, Springer, Heidelberg, 189-215.

Sunde, Ø., Friis, H., Andersen, T., Trumbull, R.B., Wiedenbeck, M., Lyckberg, P., Agostini, S., Casey, W.H. and Yu, P. (2020) - Boron isotope composition of coexisting tourmaline and hambergite in alkaline and granitic pegmatites. *Lithos*. 352–353, 105293.

Trumbull, R. B. and Slack, J. F. (2018) - Boron isotopes in the continental crust: granites, pegmatites, felsic volcanic rocks, and related ore deposits. In: Marschall, H.R. and Foster, G.L. (Eds.) Boron Isotopes - The Fifth Element. Advances in Geochemistry, vol. 7, Springer, Heidelberg, 249-272.

Van Hinsberg, V., Henry, D.J. and Marschall, H. (2011) - Tourmaline: An ideal indicator of its host environment. *The Canadian Mineralogist*, 49, 1–16.

Mineralogy and Fluid Inclusion Characteristics of the Tourmaline-Bearing Pegmatite from Bonče, Selečka Mts., North Macedonia

Čobić A.[1]*, Šmajgl D.[2], Strmić Palinkaš S.[3], Palinkaš L.A.[1], Kampić Š.[1], Boev B.[4]

[1]University of Zagreb, Faculty of Science, Department of Geology, Horvatovac 102b, 10000 Zagreb;
*corresponding author: andrea.cobic@geol.pmf.unizg.hr
ladislav.palinkas@geol.pmf.unizg.hr; stefica.kampic@geol.pmf.unizg.hr
[2]App&Tech Consulting d.o.o., Andrilovečka ulica 62, 10000 Zagreb, Croatia; danijela.smajgl@apptech-consulting.hr
[3]UiT The Arctic University of Norway, Faculty of Sciences and Technology, Department of Geosciences, Dramsvegen 201, N-9037 Tromsø, Norway; sabina.s.palinkas@uit.no
[4]Goce Delčev University, Faculty of Natural and Technical Sciences, Goce Delčev 89, MK-2000 Štip, North Macedonia; blazo.boev@ugd.edu.mk

Introduction and Geological setting

The Bonče pegmatite is situated on the western slopes of the Selečka Mts., a part of the Eastern Pelagonian tectonostratigraphic unit of the Dinaride-Hellenides. The Pelagonian tectonostratigraphic unit is app. 420 km long and 60 km wide NNW-SSE striking part of the central Hellenides. Granitoids intruded the Precambrian crystalline basement of ortho- and paragneisses, micaschists and amphibolites and according to the QAP classification are mainly granodioritic in composition and range from granite to quartz-diorite (Dumurdzanov, 1985). A sedimentary sequence, comprising carbonate and clastic rocks, was deposited during the Triassic and Jurassic.

The Bonče pegmatite is one of the numerous pegmatite occurrences in the Eastern Pelagonian zone which vary in size and differ in terms of mineralogical characteristics, internal structures and degree of fractionation. The lens-shaped and up to 5 m wide pegmatite body of Bonče with weakly developed internal zoning, and a predominance of tourmaline in the wall zone and massive quartz in the core cuts Precambrian gneisses.

Results and discussion

Mineralogical and chemical composition of tourmaline

The tourmaline unit cell parameters, calculated with the least-square refinement program UNITCELL (Holland & Redfern, 1997) on the basis of XRPD patterns are following: a= 15.961(0) Å, c = 7.189(7) Å, and V = 1586.21(4) Å3. According to the a vs. c ratio (Donnay & Barton, 1972), the results of classical chemical analysis and classification proposed by Henry et al. (2011) tourmaline from the Bonče pegmatite is classified as dravite with following structural formula calculated on the basis of B=3 *apfu*:

$$(Na_{0.664}Ca_{0.349}K_{0.082})\,(Mg_{1.405}Fe^{3+}_{0.878}Ti^{4+}_{0.070}Al_{0.038}Fe^{2+}_{0.033})\,Al_6[(Si_{5.652}Al_{0.348})O_{18}]\,(BO_3)_3(OH)_3O$$

Fluid inclusion studies

Fluid inclusions in tourmaline crystals have been classified as either primary or secondary according to the criteria proposed by Roedder (1984). Primary fluid inclusions are sub-rounded to irregular shaped, are up to 25 μm in size and occur in individual clusters or isolated. Based on the number of phases primary tourmaline-hosted fluid inclusions can be divided into two categories: 1) polyphase (L+V+S) and 2) two-phase (L+V) inclusions.

Polyphase inclusions consist of up to 50 vol. % of solid phases, highly saline aqueous solution and vapor bubbles (Fig. 1a). The solid phases are usually transparent and inactive in the Raman spectra. According to the Raman microspectroscopy data, the vapor bubbles contain only water vapor. Total homogenization occurs when the vapor phase disappears at a temperature higher than 450°C.

Two phase inclusions contain a liquid and a vapor phase at room temperature (Fig. 1b). Degree of fill (F) varies between 0.70 and 0.85. The eutectic temperature (Te) around -52°C suggests $CaCl_2$ and NaCl as dominant dissolved salts. The final ice melting temperature ($T_{m\ ICE}$) was measured between -7.0 and -8.0°C, and the clathrate melting temperature between 9.5 and 10.0°C. The total homogenization (T_H) spans from 145 to 200°C. Raman microspectroscopy revealed the presence of water, nitrogen and methane. Salinity estimated from the ice melting and clathrate melting temperatures is between 4.2 and 4.8 wt.% NaCl equ.

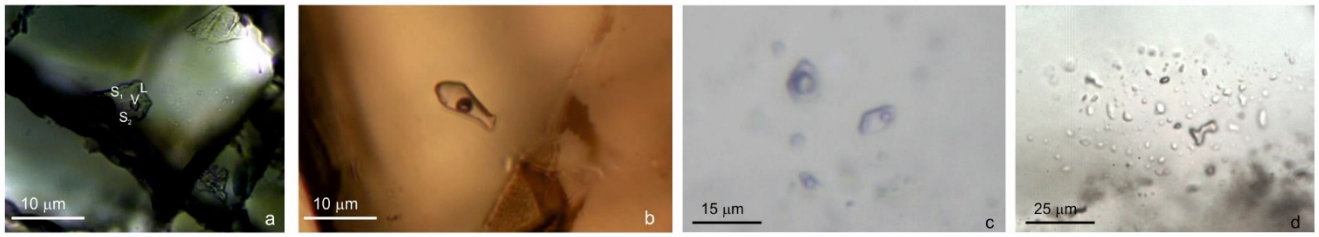

Fig. 1. Photomicrographs of representative primary fluid inclusions from the Bonče tourmaline-bearing pegmatite: a) hydrosaline (L+V+S1,2) inclusion in tourmaline; b) two-phase (L+V) inclusion in tourmaline; c) two-phase inclusion (L+V) in the massive quartz core; d) clusters of monophase inclusions in the massive quartz core

Fluid inclusions from the massive quartz core have an irregular to round shape and a size of up to 25 μm (Fig. 1c). They occur either isolated or in clusters of 5 to 10 inclusions arranged in three-dimensional, non-planar arrays. The inclusions mostly consist of two phases (liquid and vapor) and have degree of fill between 0.6 and 0.85. Raman microspectroscopy showed traces of N_2 and CH_4 within the vapor phase (Fig. 2). The eutectic temperature (≈ -52°C) suggests a Ca-Na-Cl system. The final ice melting temperatures are between -3.4 and -8.1°C (salinity between 5.6 and 11.8 wt.% NaCl equ.). The temperatures of homogenization into a liquid phase were recorded within the wide range between 173 and 400°C. The clusters of monophase inclusions (Fig. 1d) indicate the resorption and partial recrystallization of silica-rich melt inclusions within the quartz host. According to Raman microspectroscopy, the monophase inclusions contain only water.

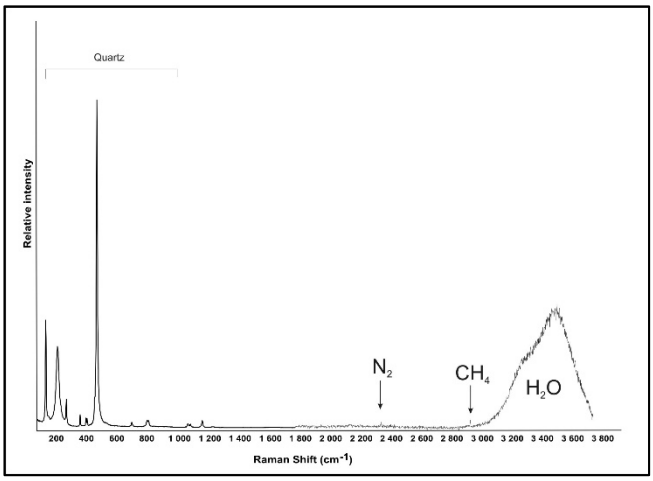

Fig. 2. Raman spectrum of the vapor bubble from two-phase inclusion hosted by quartz reveals the presence of H_2O, N_2 and CH_4

Conclusions

Textural features and fluid inclusion data suggest that the Bonče tourmaline-bearing pegmatite formed as a result of subsequent crystallization from a granitic melt.

References

Donnay G. & Barton R. Jr. (1972) - Refinement of the crystal structure of elbaite and the mechanism of tourmaline solid solution. *Tschermaks mineralogische und petrographische Mitteilungen*, 18, 273-286.

Dumurdzanov N. (1985) - Petrogenetic characteristics of the high metamorphic and magmatic rocks of the Central and Western part of the Selečka Mts. (Pelagonian massif), SR Macedonia, Yugoslavia. *Geologica Macedonica*, 2, 173-220.

Holland T.J.B. & Redfern S.A.T. (1997) - Unit cell refinement from powder diffraction data: The use of regression diagnostics. *Mineralogical Magazine*, 61, 65-77.

Roedder E. (1984) - Fluid inclusions. *Reviews in Mineralogy*, 12, 644 p.

Crystal chemistry of tourmalines from Mozambican pegmatites

Bomal, F.[1*], Hatert, F.[1], Philippo, S.[2] and Guennou, M.[3]

[1]Laboratory of Mineralogy, University of Liège B18, B-4000 Liège, Belgium

[2]Natural History Museum of Luxembourg, Münster street 25, L-2160 Luxembourg

[3]Materials Research and Technology Department, Luxembourg Institute of Science and Technology, rue du Brill 41, L-4422 Belvaux, Luxembourg

Correspondence to: Florent Bomal (florent.bomal@doct.uliege.be)

Minerals of the tourmaline supergroup are constituted by rhombohedral borosilicates with a R3m space group, and the general formula $XY_3Z_6[T_6O_{18}](BO_3)_3V_3W$ (Hawthorne & Henry, 1999).

Over the last decades, Mozambique has established itself as one of the important producers of high-quality tourmalines in the world. Although still poorly referenced, the tourmaline diversity encountered in the pegmatites of the Alto Ligonha region (Fig. 1), in the northeastern part of the country, challenges the one found in Brazil. Mozambique can therefore be considered as one of the richest contexts to study the crystal chemistry of pegmatitic tourmalines.

With this in mind, a set of 68 tourmaline samples from several pegmatites of the Alto Ligonha area (Fig. 1) were investigated by several techniques including single-crystal X-ray structure refinements, electron-microprobe, and Laser Ablation Inductively Coupled Plasma Time-Of-Flight Mass Spectrometry (LA-ICP-TOF-MS). 19 of these samples were selected amongst the collections of the National Natural History Museum of Luxembourg. The remaining 49 crystals were collected on the field in order to refine the sampling. 15 pegmatites ranging from well-known to new deposits are represented. A cartography of the pegmatites has been made whenever it was possible and the position of each sample in its respective pegmatite is known.

Tourmaline varieties observed mainly display different shades of green, pink and blue colors. Unusual red, yellow and colorless tourmalines, as well as several elbaites showing a neon-blue colour similar to that observed in Paraiba tourmalines, are also under investigation. Optical zonations along and across the *c*-axis are common amongst the samples.

Chemically, most samples are Na dominant on the X site, and therefore belong to the alkali group. They correspond to fluor-elbaites or elbaites, where similar proportions of Al and Li are sharing the Y-positions. Elbaites are located close to the elbaitic end-member, with Fe^{2+} strongly depleted and the schorlitic component negligible, while fluor-elbaites tend to align along the fluor-elbaite to fluor schorl solid-solution.

For most samples, single-crystal data indicate *a* unit-cell parameters varying between 15.8647 and 15.9503 Å, and *c* parameters ranging from 7.107 to 7.1545 Å. These values are similar to those obtained for Brazilian tourmalines of the elbaite-schorl solid solution. However, two crystals from the Marinia pegmatite display very high unit-cell parameters values ($16.008 < a < 16.0474$ Å; $7.2193 < c < 7.2338$).

A detailed cation distribution has also been established, indicating that the B site is fully occupied by boron, that the T site is mainly occupied by Si and sometimes by minor amounts of Al, and that the Z site is mainly occupied by Al with sometimes minor amounts of Si. The X site contains vacancies, Na, K, and Ca, and the Y site is occupied by Li, Al, Fe^{2+}, and minor amounts of Mn^{2+}, Ti, and Mg.

Finally, the trace element contents, including REE, are discussed in detail, and appear to be influenced by both the geochemical pegmatitic context, and by crystal-chemical constraints.

References:

Hawthorne, F.C. and Henry, D.J. (1999). *European Journal of Mineralogy* 11(2): 201-215.

Figure 1: Location of the pegmatites studied in the Alto Ligonha area

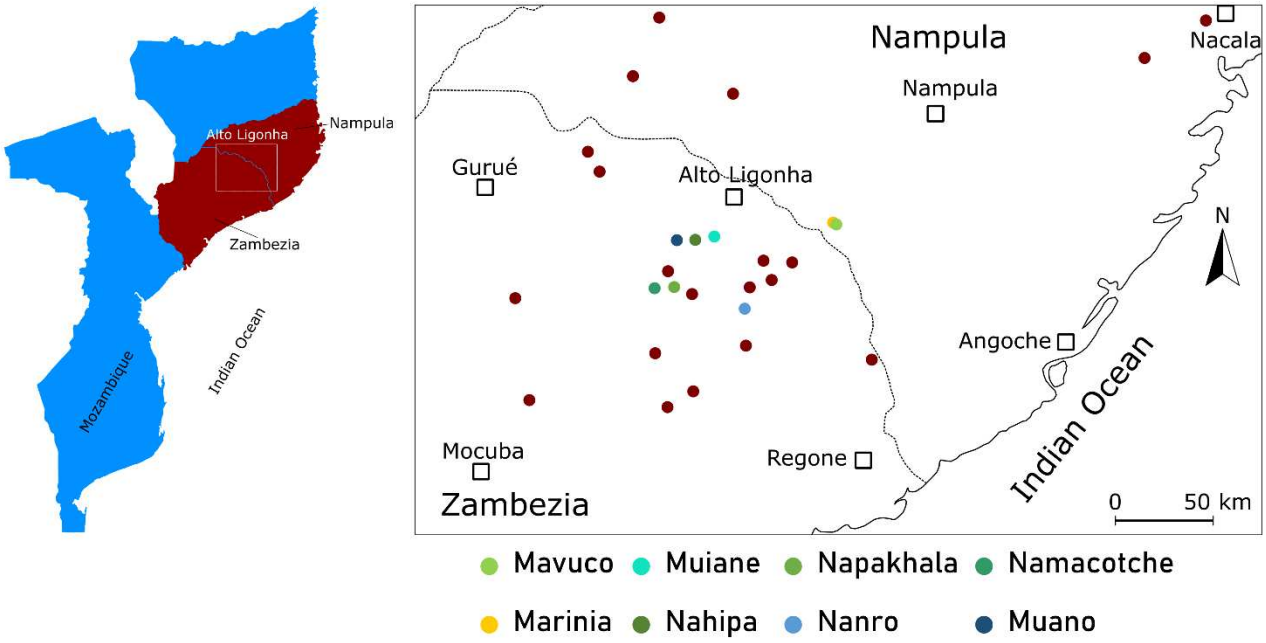

Table 1: Location and unit-cell parameters measured in the studied tourmalines from the Alto Ligonha region

	MOZ001	MOZ002-J	MOZ002-N	MOZ003	MOZ004-A	MOZ004-B	MOZ004-C
a (Å)	15.95	15.90	16.01	16.05	15.93	15.95	15.86
b (Å)	15.95	15.90	16.01	16.05	15.93	15.95	15.86
c (Å)	7.15	7.12	7.23	7.22	7.14	7.11	7.12
V (Å^3)	1576.3	1562.0	1605.4	1610	1568.7	1565.9	1552.21
Location	Mavuco	Marinia	Marinia	Marinia	Muiane	Muiane	Muiane

	MOZ006-V	MOZ008	MOZ009-B	MOZ010-V	MOZ011-B	MOZ012
a (Å)	15.92	15.91	15.89	15.94	15.94	15.91
b (Å)	15.92	15.91	15.89	15.94	15.94	15.91
c (Å)	7.13	7.12	7.12	7.14	7.13	7.13
V (Å^3)	1564.65	1560.7	1557.04	1571.17	1569.61	1561.49
Location	Nahipa	Napakhala	Nanro	Namacotche	Muano	Maria II

Tourmaline thermodynamics and excursions to other borosilicates

Vincent van Hinsberg[1,2,*], Stan Roozen[2]

[1] Geotop Research Centre, McGill University, Montreal, Canada
[2] Earth and Planetary Sciences, McGill University, 3450 University Street, Montreal, Quebec, H3A0E8, Canada
[*] Corresponding author: *hinsberg@eps.mcgill.ca*

Tourmaline is a singularly powerful petrogenetic indicator mineral. It is able to provide information on the *P-T* conditions of its formation through geothermobarometry (van Hinsberg & Schumacher 2007a; 2009) and compositional systematics (Henry & Dutrow 1996; Ertl *et al.* 2008); the major and trace element composition of the melt or fluid from which it formed from element partition coefficients (von Goerne *et al.* 2001; van Hinsberg 2011; van Hinsberg *et al.* 2017); the source reservoirs of its constituent elements from isotope signatures (Marschall & Jiang 2011; Slack & Trumbull 2011); and the age of its formation from geochronology (Bea *et al.* 2009). It combines this recording ability with a large *P-T-X* stability field that covers most crustal conditions, typical bulk-rock compositions, and geotectonic settings. This combination makes tourmaline a truly unique petrogenetic recorder. However, a fundamental set of properties is missing, which limits tourmaline realising this potential: We currently lack the thermodynamic data and models to include tourmaline in thermo-chemical modelling. This prohibits predictive modelling of its progressive formation and compositional evolution in prograde metamorphism or igneous fractionation, its stability in a diversity of hydrothermal fluids, or its impact on the phase relations of coexisting phases. This is essential information to interpret data on *P-T-X-t* derived from tourmaline in light of the geotectonic history of its host rocks.

In this presentation, we will provide a historical overview of the progress in constraining tourmaline thermodynamic properties, and will then present new volumetric and calorimetric data for a comprehensive suite of tourmalines that allows us to define a thermodynamic solid solution model that spans the full range of common, Li-free tourmaline compositions. We further use this basis set to create an extension to Li-bearing tourmalines, as well as other borosilicates, and showcase a number of applications of this new thermodynamic database in petrological modelling.

Tourmaline thermodynamics – A full thermodynamic description of a mineral needs to capture the calorimetric, structural and volumetric contributions to its Gibbs free energy, which are combined in the equation $\Delta G_f = \Delta H_f^0 + \int_{T_0}^{T} C_P dT - T\left\{S^0 + \int_{T_0}^{T} \frac{C_P}{T} dT + S_{conf}\right\} + P\int_{P_0}^{P} V_T dP + \Delta G_{exc}$ where ΔH is enthalpy, S entropy, V molar volume and C_P heat capacity. Only a few direct measurements of ΔH, S, C_P and compressibility exist (Kuyunko *et al.* 1984; Hemingway *et al.* 1996; Ogorodova *et al.* 2004; Berryman *et al.* 2019), but more data are available for molar volume (*e.g.,* Bosi & Lucchesi 2004). These data have been used to derive partial thermodynamic properties for ^{III}B and ^{IV}B to expand summation estimation methods to tourmaline (*see* Garofalo *et al.* 2000; van Hinsberg & Schumacher 2007b). These estimates agree within error with those derived from phase relations (Dutrow *et al.* 1999). Despite providing a full thermodynamic description of tourmaline, these approaches come with large uncertainty, and only provide a qualitative to semi-quantitative modelling capability (*cf.* van Hinsberg & Schumacher 2007b). Tourmaline presents additional thermodynamic complexity owing to multiple elements residing on a given site (*e.g.,* Mg and Al on the Y-site of uvite) and elements distributing over multiple sites (*e.g.* Mg, Fe and Al over the Y and Z-sites). This results in a configurational entropy term (S_{conf}), and, if this element mixing on a site is non-ideal, a further excess Gibbs free energy term (G_{exc}). Natural tourmalines' compositional range necessitates a large set of endmembers to thermodynamically capture this full diversity. Given that we have not been successful in synthesizing endmember tourmalines (*cf.* von Goerne *et al.* 2001), we need to extrapolate to these endmembers from measurements on intermediate compositions. This involves further challenges related to obtaining tourmaline's molecular formula, which requires a full chemical characterization combined with crystal-structural data to determine the distribution of the elements over the tourmaline sites. However, multiple solutions are generally valid within uncertainties, and site assignment moreover depends on our understanding of the tourmaline structure. Ambiguity still exists in the latter, including whether

vacancies can exist on the Y and Z sites, and what elements can distribute over the sites and with what preferences. Our work indicates that ambiguity in the molecular formula is the largest contributor to the uncertainty in thermodynamic properties.

A thermodynamic model for tourmaline – Volumetric and calorimetric measurements of >50 natural and synthesized tourmalines allowed us to define a thermodynamic solid solution model for Li-free tourmalines. Using the approach of van Hinsberg & Schumacher (2007b), we then estimated the properties of Li-bearing tourmalines and other borosilicates to derive a database suitable for modelling the stability, abundance and compositions of tourmaline and associated borosilicates in natural rocks under hydrothermal and metamorphic conditions. Results indicate that tourmaline has a major impact on mineral parageneses, mineral abundance, and compositions, in agreement with field observations. Future work will focus on validating estimated Li-tourmaline thermodynamic data, optimizing the thermodynamic properties and interaction parameters using natural and experimental constraints, and improving data for other borosilicate phases. Meaningful modelling of tourmaline element exchange with fluids at high temperature and melt-bearing systems is still challenging and will require a better understanding and thermodynamic data for B-species in fluids and melts.

Bea, F, Pesquera, A, Montero, P, Torres-Ruiz, J, Gil-Crespo, PP (2009) Tourmaline $^{40}Ar/^{39}Ar$ chronology of tourmaline-rich rocks from Central Iberia dates the main Variscan deformation phases. Geologica Acta 7, 399–412.

Berryman, EJ, Zhang, D, Wunder, B, Duffy, TS.(2019) Compressibility of synthetic Mg-Al tourmalines to 60 GPa. American Mineralogist 104, 1005–1015.

Bosi, F, Lucchesi, S (2004) Crystal chemistry of the schorl-dravite series. European Journal of Mineralogy 16, 335–344.

Dutrow B, Foster, C, Henry, DJ (1999) Tourmaline-rich pseudomorphs in sillimanite zone meta-pelites: Demarcation of an infiltration front. American Mineralogist 84, 794–805.

Ertl, A, Tillmanns, E, Ntaflos, T, Francis, C, Giester, G. Körner, W, Hughes, JM, Lengauer, C, Prem, M (2008) Tetrahedrally coordinated boron in Al-rich tourmaline and its relationship to the pressure–temperature conditions of formation. European Journal of Mineralogy 20, 881–888.

Garofalo, P, Audétat, A, Günther, D, Heinrich, CA, Ridley, J (2000) Estimation and testing of standard molar thermodynamic properties of tourmaline end-members using data of natural samples. American Mineralogist 85, 78–88.

Hemingway, B, Evans, H, Mazdab, F, Anovitz, L (1996) Thermal expansion of some borate and boro-silicate minerals between 25 and about 1200˚C. USGS open file report 96-100.

Henry, DJ, Dutrow, BL (1996) Metamorphic tourmaline and its petrologic applications. In: E Grew and L Anovitz, Eds., Boron. Reviews in Mineralogy 33, 503–557.

Kuyunko, N, Semenov, Y, Gurevich, V, Kuzmin, V, Topor, N, Gorbunov, V (1984) Experimental-determination of thermodynamic properties of dravite tourmaline. Geokhimiya, 1458–1465.

Marschall, HR, Jiang, S-Y (2011) Tourmaline isotopes: No element left behind. Elements, 7, 313–319.

Ogorodova, L, Melchakova, L, Kiseleva, I, Peretyazhko, I (2004) Thermodynamics of natural tourmaline-elbaite. Thermochimica Acta 419, 211–214.

Slack, JF, Trumbull, RB (2011) Tourmaline as a recorder of ore-forming processes. Elements 7, 321-326

van Hinsberg, V, Schumacher, J (2007a) Intersector element partitioning in tourmaline: a potentially powerful single crystal thermometer. Contributions to Mineralogy and Petrology 153, 289–301.

van Hinsberg, VJ (2011) Preliminary experimental data on trace-element partitioning between tourmaline and silicate melt. Canadian Mineralogist 49, 153–163.

van Hinsberg, VJ, Schumacher, JC (2007b) Using estimated thermodynamic properties to model accessory phases: the case of tourmaline. Journal of Metamorphic Geology 25, 769–779.

van Hinsberg, VJ, Schumacher, JC (2009) The geothermobarometric potential of tourmaline, based on experimental and natural data. American Mineralogist 94, 761–770.

van Hinsberg, VJ, Franz, G, Wood, BJ (2017) Determining subduction-zone fluid composition using a tourmaline mineral probe. Geochemical Perspectives Letters, 160–169.

von Goerne, G, Franz, G, Heinrich, W (2001) Synthesis of tourmaline solid solutions in the system Na_2O-MgO-Al_2O_3-SiO_2-B_2O_3-H_2O-HCl and the distribution of Na between tourmaline and fluid at 300 to 700°C and 200 MPa. Contributions To Mineralogy and Petrology, 141, 160–173

Evolution of magnesio-lucchesiite in calc-silicate rock from Černá v Pošumaví, Czech Republic

Jakub Vácha[1,*], Jan Cempírek[1], Milan Novák[1]

[1]Department of Geological Sciences, Masaryk University, Kotlářská 267/2, 611 37 Brno, Czech Republic

* Corresponding author: *jvacha@mail.muni.cz*

The Ca-Mg members of the tourmaline supergroup (fluor-uvite, uvite, magnesio-lucchesiite), occasionally occur in hydrothermal or pegmatite veins cross-cutting Ca-Mg rich rocks, such as marbles, amphibolites, or serpentinites (e.g. Scribner et al. 2021, Sęk et al. 2023, Bosi et al. 2022). Records of magnesio-lucchesiite are published from O´Grady lamprophyre (Canada) and San Piero in Campo serpentinite-hosted hydrothermal veins (Italy; Scribner et al. 2021), Manjaka pegmatite (Madagascar; Gadas et al. 2023), Budniki amphibolite-hosted quartz veins (Poland; Sęk et al. 2023) and Zlatá Idka tourmalinite (Slovakia; Bačík et al. 2022). Fluor-uvite and uvite belong among more common tourmalines in such lithologies (e.g. Bosi et al. 2022).

The Černá v Pošumaví quarry, South Bohemia, Czech Republic, exploits biotite gneiss, calc-silicate rocks and marble, with occasional pegmatite veins cutting all lithologies. Four evolved, lithium-bearing pegmatites (Černá I and II, Bližná I and II) are known from Černá v Pošumaví and neighbouring Bližná. A large variety of tourmalines was recorded from these four bodies, namely schorl, foitite, dravite, oxy-dravite, fluor-dravite, elbaite, fluor-elbaite, liddicoatite, fluor-liddicoatite, uvite, fluor-uvite, olenite, and tsilaisite (Novák et al. 1999, Vácha & Novák 2022, and references therein).

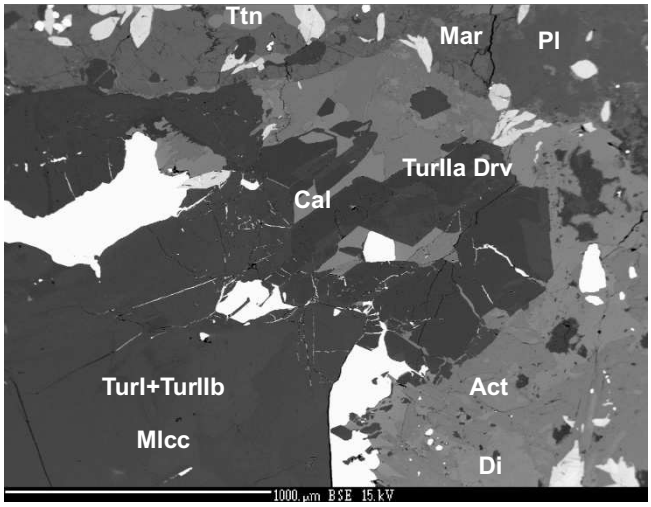

TurI and TurIIb magnesio-lucchesiite (Mlcc) and TurIIa dravite (Drv) with marialite (Mar), plagioclase (Pl), calcite (Cal), titanite (Ttn), actinolite (Act) and sulphides (BSE bright).

Fragments with contact of grey to green, medium grained calc-silicate rock and biotite gneiss were collected in the Černá v Pošumaví quarry. The calc-silicate rock consists of abundant diopside, marialite, plagioclase ($Ab_{57–80}An_{43–20}$), K-feldspar, phlogopite, large grains (2 cm) of dark brown tourmaline, amphibole, chlorite, calcite, and accessory titanite, apatite, clinozoisite, prehnite, muscovite, zircon, galena and pyrite/pyrrhotite.

Two chemically distinct tourmaline types are observed in the assemblage. The volumetrically dominant cores of tourmaline grains are mostly ^{X}Ca-dominant (0.43–0.86 apfu), with significant ^{X}Na content (0.15–0.59 apfu), trace K and negligible *X*-site vacancy. The *Y*-site is dominated by Mg (2.34–2.81 apfu), with minor Fe (0.14–0.52 apfu) and relatively high Ti (0.05–0.26 apfu). The Fe valence was not analysed, and at least partial oxidation to Fe^{3+} is expected. The ^{Z}Al (5.35–5.74 apfu) is partly substituted by ^{Z}Mg (0.25–0.63 apfu). The ^{T}Si ranges from 5.90 to 6.01 apfu, with minor ^{T}Al. The ^{W}F is relatively low (0.22–0.54 apfu), and only rarely dominant constituent at the *W*-site. The tourmaline can be mostly classified as **magnesio-lucchesiite**, along with minor **uvite**, **fluor-uvite**, **dravite**, and **fluor-dravite**. Minor dark (both optically and in BSE) irregular tourmaline zones are present along rims of the large grains. The tourmaline in the rim zones is significantly richer in ^{X}Na (0.59–0.76 apfu) and ^{Z}Al (5.88–6.23 apfu), while being poorer in ^{X}Ca (0.13–0.39 apfu), ^{Y}Ti (0.02–0.10 apfu), ^{Z}Mg (≤0.13 apfu), and ^{W}F (≤0.21 apfu). It is classified as **dravite** to minor **fluor-dravite**. The Mg/(Mg+Fe) ratios are consistent among tourmaline generations and range from 0.84 to 0.96.

Amphibole does not show any significant zoning. It is Na-poor (≤0.11 apfu), with elevated Fe (0.36–0.81 apfu), low Ti (≤0.10 apfu) and F ranging from 0.10 to 0.30 apfu. It can be classified as actinolite to tremolite. The associated diopside is very close to the end member, with negligible Na, Fe, Ti, and Al contents. The Mg/(Mg+Fe) ratio in pyroxene is slightly higher than in amphibole (0.91–0.97 vs. 0.83–0.93).

The scapolite (marialite) is chemically homogenous, with average formula $(Na_{1.92}K_{0.14}Ca_{1.91})_{\Sigma 3.97}(Si_{7.77}Al_{4.23})_{\Sigma 12.00}O_{24.39}Cl_{0.86}F_{0.01}$.

Representative tourmaline analyses

Classification	magnesio-lucchesiite	uvite	fluor-uvite	dravite
Generation	TurI	TurI	TurI	TurIIa
SiO_2	35.90	36.33	35.33	37.36
TiO_2	1.24	1.70	0.41	0.21
B_2O_3*	10.57	10.71	10.66	10.88
Al_2O_3	28.90	29.02	29.76	32.55
FeO	3.61	2.14	1.00	2.32
MgO	11.60	12.61	13.71	10.76
CaO	3.19	3.49	4.90	1.20
Na_2O	1.41	1.04	0.59	2.40
K_2O	bdl	0.06	bdl	bdl
H_2O*	3.08	3.13	2.96	3.45
F	0.63	0.57	1.05	0.09
O=F	-0.26	-0.24	-0.44	-0.04
Total	99.86	100.54	99.91	101.19

* calculated values; bdl (below detection limit)

The textural relations among minerals show that the metamorphogenic plagioclase-diopside-titanite-apatite-clinozoisite assemblage was penetrated by boron- and fluorine-rich fluids, forming large grains of Ca-Mg tourmaline I (**TurI**). The second generation of fluids was Na-rich, altering TurI to dravitic **TurIIa**. The TurIIa is depleted of Ca, Mg, and F. Simultaneously, diopside was altered to actinolite and the plagioclase was albitized. The primary TurI was partly re-crystallized to unevenly zoned **TurIIb**. The TurIIb is hardly distinguishable in BSE and chemically very similar to TurI. Calcite, pyrite/pyrrhotite, and galena belong to the youngest hydrothermal event recorded in the rock. The relative timing of phlogopite chloritization to clinochlore, origin of prehnite, and scapolite formation (possibly after plagioclase) is unclear; these processes occurred either within the sodic alteration phase, or during the last (calcite-sulphide) event.

Similar diopside-rich, calc-silicate lithology with multi-generational tourmalines are known e.g. from Portage du Fort, Québec, Canada. The tourmalines have variable composition, ranging from uvite to dravite, with variable Ti and significant fluorine contents positively correlated with calcium (Belley et al. 2014).

The studied mineral assemblage shows that magnesio-lucchesiite can be an important species in calc-silicate rocks where its compositional changes allow deciphering part of the rock evolution. However, due to its visual similarity to dark garnet or dravite, its presence can be easily overlooked or underestimated.

References

Bačík P., Odzín D., Uher P. and Chovan M. (2022) - Crystal chemistry and evolution of tourmaline in tourmalinites from Zlatá Idka, Slovakia. - *Journal of Geosciences*, 67, 209-222

Belley P. M., Grice J. D., Fayek M., Kowalski P. M. and Grew E. S. (2014) – New Occurrence of the Borosilicate Serendibite in Tourmaline-Bearing Calc-Silicate Rocks, Portage-du-Fort Marble, Grenville Province, Québec: Evolution of Boron Isotope and Tourmaline Compositions in a Metamorphic Context. – *The Canadian Mineralogist*, 52, 595-616.

Bosi F., Biagioni C., Pezzotta F., Skogby H., , Halenius U., Cempírek J., Hawthorne F., Lussier A. J., Abdu Y. A., Day M. C., Fayek M., Clark C. M., Grice J. D. and Henry D. J. (2022) - Uvite, $CaMg_3(Al_5Mg)(Si_6O_{18})(BO_3)_3(OH)_3(OH)$, a new, but long-anticipated mineral species of the tourmaline supergroup from San Piero in Campo, Elba Island, Italy. - *Mineralogical Magazine*, 86, 767-776.

Gadas P., Novák M., Vašinová Galiová M. and Pezzotta F. (2023) - Chemical composition of tourmalines from the Manjaka pegmatite and its exocontact, Sahatany Valley, Madagascar. - *Journal of Geoscienc*, 68, 185-202.

Novák M., Selway J., Černý P., Hawthorne F. and Ottolini L. (1999) - Tourmaline of the elbaite-dravite series from an elbaite-subtype pegmatite at Bližná, southern Bohemia, Czech Republic. - *European Journal of Mineralogy*, 11, 557-568.

Scribner E. D., Cempírek J., Groat L. A., Evans R. J., Biagioni C., Bosi F., Dini A., Hålenius U., Orlandi P. and Pasero M. (2021) - Magnesio-lucchesiite, $CaMg_3Al_6(Si_6O_{18})(BO_3)_3(OH)_3O$, a new species of the tourmaline supergroup. *American Mineralogist*, 106, 862-871.

Sęk M. P., Włodek A., Stachowicz M., Woźniak K. and Pieczka A. (2023) - Magnesio-lucchesiite from the Kowary vicinity, Karkonosze Mountains, SW Poland: the third occurrence worldwide. - *Mineralogical Magazine*, 87, 60-68.

Vácha J. and Novák M. (2022) - Tsilaisit z Černé v Pošumaví, nový mineral pro ČR (in Czech). - *Minerál*, 30, 230-233.

Overview of the geology and metallogeny of Madagascar (PGRM 2012)

RAZAFIMAROSON Yvan Tommy [1,*], RAMIANDRISOA Njararivelo Louisa[2] , RAFEDISON Mandimbisoa Jocelyn[3]

1 University of Antananarivo, Faculty of Science, Geology Applied to Development and the Environment[1]

2 University of Antananarivo, Faculty of Science, Geology Applied to Development and the Environment[2]

3 University of Antananarivo, Faculty of Science, Geology Applied to Development and the Environment[3]

* Corresponding author: yvanto22@gmail.com

The Mining Resources Governance Programme (PGRM) has highlighted the geological richness and complexity of Madagascar, whose subsoil is dominated by a Precambrian basement. This is divided into six major geological domains: Antongil-Masora, Antananarivo, Ikalamavony, Androyen-Anosyen, Bemarivo and Vohibory.

Geological and tectonic context

The Antongil-Masora Domain, dating from the Meso- to Neoarchean, is a fragment of the Western Dharwar Craton (India). The fact that it was joined to the Antananarivo Domain in the Terminal Archean calls into question the 'Betsimisaraka Suture'. These two domains, together with the Tsaratanana Complex, form an ensemble comparable to the Greater Dharwar Craton, testifying to a geological heritage shared with India. To the south, the Anosyen-Androyen Domain is a Palaeoproterozoic entity marked by the Beraketa shear. The Ikalamavony Domain is a complex volcanosedimentary transition zone. To the north, the Bemarivo Domain is a Neoproterozoic magmatic arc, while the Vohibory Domain, to the south-east, is an exotic island arc of East African affinity. These blocks were formed and fused during crustal accretion, deformation and intense magmatic episodes (such as the Dabolava, Imorona-Itsindro and Ambalavao-Kiangara-Maevarano suites).

Metallogenic potential

Madagascar's geological diversity is exceptionally rich in minerals. Nickel, Cr, Cu, PGE, Pb, Zn, barite and stratiform copper are found. Gold is present in 14 districts, and VMS deposits, Cu-U-Th skarns, rare earths, uranium and Nb-Ta-REE pegmatites have been identified. Diamond potential has also been noted in the Antongil-Masora Domain.

Resources of Precious, Fine and Industrial Gemstones

Madagascar is world-renowned for its wealth of precious and semi-precious stones, both in diversity and quality, these gems being found mainly in skarns, pegmatites, metamorphic rocks and alluvial deposits. Among gemstones, Madagascar is a major producer of sapphires, with renowned deposits at Ilakaka-Sakaraha, Andranondambo, Didy and Andilamena, and also produces rubies (mainly at Andilamena and Didy), emeralds (at Mananjary and Ilakaka), as well as abundant garnets and spinels. Fine and ornamental stones include tourmalines, beryl (aquamarine, morganite), and various varieties of gem quartz (amethyst, citrine, rose quartz), not forgetting other minerals such as zircons, apatites, diopsides, scapolites and cordierites. Industrial resources are also exploited, such as industrial quartz, ornamental calcite and aragonite, and olivine, feldspar and micas from pegmatites.

Other Resources and Potential

Laterite formations provide nickel, cobalt, bauxite and kaolin. Alluvial deposits mine gold, PGE, precious stones and titanium. Other key industrial resources include graphite, quartz, clay, talc, magnesite, mica, silica, salt, gypsum, limestone, barite and potentially potash. In conclusion, Madagascar's Precambrian geology, with its Indian links, offers exceptional mining potential, the development of which is strategic for the country's economy.

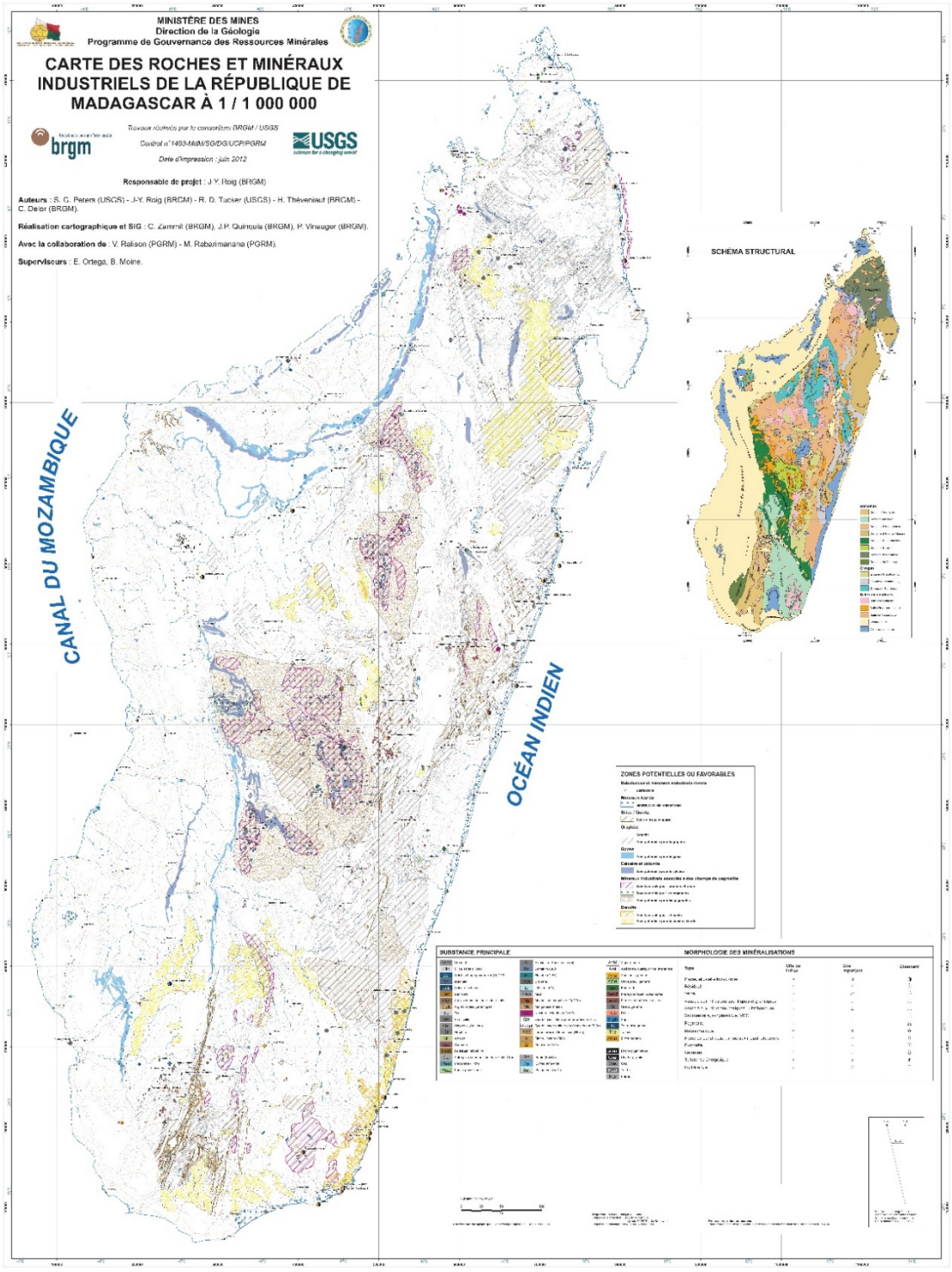

FIGURE : Geological and strategic mineral map of Madagascar 1,000,000

References

- Collins, A. S., & Windley, B. F. (2002). The Neoproterozoic accretionary history of Madagascar and its bearing on the assembly of Gondwana. ***Earth-Science Reviews***, ***59***(1-4), 1-13.

- Handelsman, D. (2014). ***Mineral Resources of Madagascar: A Review***. U.S. Geological Survey Open-File Report 2014–1110.
- Ramambazafy, H., Madiro, R., & Raharimahefa, T. (2007). ***Géologie de Madagascar: Notice explicative de la carte géologique au 1/1 000 000***. Ministère de l'Énergie et des Mines, Direction Générale des Mines et de la Géologie.
- Schwarz, D., Schmetzer, K., & Bank, H. (1996). Emeralds from Madagascar. ***Gems & Gemology***, ***32***(2), 80-87.

Theoretical mineralogy and tourmalines: possibilities of the Bond Valence Topological Modelling

Peter Bačík[1,2,*], Jana Fridrichová[1], Andreas Ertl[3,4]

[1] Comenius University in Bratislava, Faculty of Natural Sciences, Department of Mineralogy, Petrology and Economic Geology, Ilkovičova 6, 842 15, Bratislava, Slovak Republic

[2] Earth Science Institute, Slovak Academy of Sciences, Dúbravská cesta 9, SK-845 28 Bratislava, Slovakia

[3] Mineralogisch-Petrographische Abt., Naturhistorisches Museum, Burgring 7, 1010 Wien, Austria

[4] Institut für Mineralogie und Kristallographie, Universität Wien, Josef-Holaubek-Platz 2, 1090 Wien, Austria

*Correspondencing author: peter.bacik@uniba.sk

Crystal chemistry is influenced by other sciences, especially mathematics, physics, and chemistry. The effects of physics and chemistry are mainly in the application of quantum mechanics to solve crystal-chemical problems, which has led to theories such as bond valence theory. The mathematical apparatus for crystallography and crystal chemistry expanded along with group theory to include topology and graph theory. These concepts form the basis for the structural topology, which primarily utilizes topological graphs for the systematic analysis of crystal structures. Since the structure topology deals with the topological representations of crystal structures and uses unweighted graphs, the approach using weighted graphs to solve bond properties (bond valence, bond length) in smaller fragments can be defined as bond-valence topology. The bond-valence topology utilizes concepts such as bond-valence topological graphs, bond-valence topological maps, and structural arrangements. The bond-valence topological graph represents a segment of the structure that can be chosen based on the studied phenomena. In bond-valence topological graphs, atoms or structural sites are vertices, and bonds are edges of the graphs. The bond-valence topological model (BVTM) is the specific structural fragment represented as a bond-valence topological graph with attached values of bond valences or lengths.

Theoretical bond-length calculations from ideal bond valences for each ion and coordination allowed for the prediction of site preference in tourmaline structures at low-pressure conditions. The calculations provided the following conclusions: the *B*-site occupancy is strictly limited to B^{3+}; the *T* site can freely accommodate Si^{4+}, B^{3+}, and Al^{3+}; the Be^{2+} substitution results in a significant difference in charge. Satisfactory bond lengths for octahedral sites were calculated for Al^{3+} (Z-site preference), Ti^{4+}, Mn^{3+}, Ga^{3+}, V^{3+}, Fe^{3+} (mixed preference), Mg^{2+}, Fe^{2+}, Li^{+}, Mn^{2+}, Ni^{2+}, Zn^{2+}, Cu^{2+}, Sc^{3+} and Zr^{4+} (*Y*-site preference). Cations such as U^{4+}, Th^{4+}, Y^{3+}, lanthanoids from Tb to Lu, and Ce^{4+} have significantly longer bonds than typical Y-O and short bonds for the *X* site; their preference for an octahedron is assumed. The empirical bond length for the *X* site is met with Na^{+}, Ca^{2+}, Sr^{2+}, Pb^{2+}, and lanthanoids from La to Gd, while K, Rb, and Cs are too large in the low-pressure conditions (Bačík and Fridrichová, 2021).

Bond-valence topological models can be used to create a bond-valence topological map of real mineral structures. This map is a composite of BVTM added together, which, as a result, should have identical properties to the real structure. Tourmaline from Forshammar, Sweden (Bačík et al., 2012), was chosen for the bond-valence topological mapping because of the very low Fe and Mn content and relatively simple composition. The composition of dravite from Forshammar can be expressed as the sum of different components: ordered and disordered pairs of dravite, oxy-dravite, uvite, magnesio-foitite, magnesio-dutrowite, schorl, and schorl-dravite. Two factors were used for testing them: (1) long-

range stability and (2) local bond valence stability. Considering long-range stability based on the difference between the average sizes of the *Y*- and *Z*-site octahedra (Bosi, 2018), ordered dravite, uvite, and magnesio-dutrowite can be considered unstable. Taking a local bond valence stability into account, ordered dravite, schorl-dravite, schorl, oxy-dravite, and magnesio-dutrowite can be considered unstable due to the large difference in the sum of BVS at various sites compared to their FV. The final bond-valence topological map revealed that dravite from Forshammar is composed of the disordered dravite (ratio of 0.186), schorl-dravite (0.084), schorl (0.089), oxy-dravite (0.412), uvite (0.045), magnesio-foitite (0.024), and magnesio-dutrowite (0.024) components.

Bond-valence topological graphs can also allow for the dealing of more complex crystal-chemical problems by visualizing structural fragments and calculating the properties of bonds in the specific fragment. We can treat the bond-valence topological graph as a representation of the bond-valence topological field, and bond valences or lengths in the topological segments can be treated as discrete topological (bond-length, bond-valence) field values. The edges of the topological graph (bonds) are transformed into points of the discrete topological field. Moreover, the subtraction of two bond-valence topological fields results in the gradient bond-valence topological field, which shows changes between two compositional arrangements.

The incorporation of trivalent and divalent cations at the tetrahedral sites of tourmaline can be studied with the bond-valence topological field modeling. Four types of substitutions were proposed: TS1 – charge-balanced at the *Y* site, i.e., ${}^{T}\mathrm{Al}({}^{T}\mathrm{B}) + {}^{Y}\mathrm{Al} \rightarrow {}^{T}\mathrm{Si} + {}^{Y}\mathrm{Mg}$, and ${}^{T}\mathrm{Be} + 2{}^{Y}\mathrm{Al} \rightarrow {}^{T}\mathrm{Si} + 2\ {}^{Y}\mathrm{Mg}$; TS2 – charge-balanced at the *X* site, i.e., ${}^{T}\mathrm{Al} + {}^{X}\mathrm{Ca} \rightarrow {}^{T}\mathrm{Si} + {}^{X}\mathrm{Na}$, and ${}^{T}\mathrm{Be} + {}^{X}\mathrm{Y} \rightarrow {}^{T}\mathrm{Si} + {}^{X}\mathrm{Na}$; TS3 – charge-balanced at the *Y* site containing Li, i.e., ${}^{T}\mathrm{B} + 2{}^{Y}\mathrm{Al} + {}^{Y}\mathrm{Li} \rightarrow {}^{T}\mathrm{Si} + 3{}^{Y}\mathrm{Mg}$; TS4 – doubled substitution charge-balanced at the *Y* site, i.e., $2{}^{T}\mathrm{B} + 2{}^{Y}\mathrm{Al} \rightarrow 2{}^{T}\mathrm{Si} + 2{}^{Y}\mathrm{Mg}$. There are differences in the structural effects between substitutions. Substitution of ${}^{T}\mathrm{B}$ requires a compressed structure, because B causes compression of the B-bearing tetrahedron, and lower ${}^{T}\mathrm{B}$–O bond valence results in compression of neighboring polyhedra. The Al substitution causes the expansion of the substituted tetrahedron, which can be effectively compensated by the compression of neighboring polyhedra. The substitution of Be^{2+} results in the large instability of the structure due to its bond valence requirements.

Structural arrangements around the *Y* site in the Li-bearing tourmaline structure were investigated to determine its stability. Possible short-range ordering including Al and Li at the *Y* sites, with Na, Ca, or (vacancy) at the *X* site, Si (and Al or B) at the *T* sites, and either (OH) or F at the *W* site was investigated. Tourmaline with varying amounts of Na but no Ca can only contain up to 1 *apfu* ${}^{Y}\mathrm{Li}$. Tourmaline with higher Li content (Li >1 apfu) can form when Ca is included. Such tourmaline requires fluorine because more Li results in O1 underbonding, whereas more Al at the *Y* site leads to O1 overbonding. Underbonding of O1 is preferable for F because OH at the O1 site usually has a bond valence sum higher than 1.00 *vu* due to hydrogen bonding of H to ring oxygen atoms. Therefore, liddicoatitic tourmaline is enriched in F and is usually F-dominant.

Acknowledgement: This work was funded by the EU NextGenerationEU through the Recovery and Resilience Plan for Slovakia under the project No. 09I03-03-V04-00060 (PB, JF) and in part (AE) by the Austrian Science Fund (FWF) project P 35585.

References

Bačík P. and Fridrichová J. (2021) – Cation partitioning among crystallographic sites based on bond-length constraints in tourmaline-supergroup minerals. *American Mineralogist*, 106, 851-861.

Bačík P., Uher P., Ertl A., Jonsson E., Nysten P., Kanický V. and Vaculovič T. (2012) – Zoned REE-enriched dravite from a granitic pegmatite in Forshammar, Bergslagen Province, Sweden: An EMPA, XRD and LA-ICP-MS study. *The Canadian Mineralogist*, 50, 825–841.

Bosi F. (2018) – Tourmaline crystal chemistry. *American Mineralogist*, 103, 298-306.

Heat treatment of Paraìba tourmalines from Mozambique: a study of color changes

R. Luppi[1], F. Pezzotta[2], H. Skogby[3], and F. Bosi[1]

[1] Dipartimento di Scienze della Terra, Sapienza Università di Roma, Piazzale Aldo Moro 5, I-00185, Rome, Italy
[2] MUM – Mineralogical Museum Luigi Celleri, San Piero in Campo, Elba Island, Italy
[3] Department of Geosciences, Swedish Museum of Natural History, P.O. Box 50 007, 104 05 Stockholm, Sweden
* Corresponding author: riccardo.luppi@uniroma1.it

Tourmalines, chemically complex borosilicates, represent a perfect example of the extreme color variability exhibited by minerals (Bosi, 2018). Through various physicochemical mechanisms, they can display a wide range of colors across the entire visible spectrum, from red to violet. This distinctive and highly valued characteristic gives tourmalines significant gemological value (Pezzotta and Laurs, 2011). The most appreciated variety of tourmaline for its bright colors, ranging from turquoise-green to neon blue, is Paraíba. This rare Cu-bearing tourmaline, found in Brazil, Nigeria, and Mozambique, is currently one of the most expensive gemstones on the market, with prices reaching up to USD 50,000 per carat (Pezzotta and Laurs, 2011). Specimens exhibiting intense blue hues are due to Cu, present at concentrations of several hundred ppm by weight, whereas Fe contents are typically below 1 wt% (Katsurada et al., 2019). In tourmaline, the transition elements Ti, V, Cr, Mn, Fe, and Cu act as primary chromophores, occupying octahedrally coordinated sites in the structure and thus influencing both the hue and saturation of the color (Rossman et al., 1991; Pezzotta and Laurs, 2011; Li et al., 2018). However, defects induced by impurities and polyhedral distortions may also affect the perceived color (Li et al., 2018). Therefore, understanding the natural causes of color and the mechanisms responsible for color variations induced by heat treatment is important for accurately distinguishing between natural coloration and that resulting from laboratory treatments, a challenge that remains open in the tourmaline crystal chemistry. In this study, in order to investigate the influence of heat treatment on tourmaline color, more than 40 Cu-bearing tourmaline samples of various hues were subjected to heating under controlled atmosphere conditions. The samples were sourced from the Mavuco area (Alto Ligonha, Mozambique), which hosts the world's largest and most recently discovered alluvial deposit of Cu-bearing tourmalines (Laurs et al., 2008). The color of each sample was classified using the Munsell Color System (World of Color), both in transmitted and incident light, and observed along the crystallographic **a** and **c** axes before and after each heating cycle. Samples that developed improved neon-blue hues after treatment, along with a representative selection of major color categories, were subjected to crystal-chemical characterization via electron microprobe analysis (EMPA), optical absorption spectroscopy (OAS), and Fourier-transform infrared spectroscopy (FTIR). The results indicate that the studied Paraíba tourmalines exhibit elbaitic and liddicoatitic compositions, and that their color is primarily determined by the combination, concentration, and oxidation state of Cu, Mn, Fe, and Ti.

The chromatic response of the samples to heating was heterogeneous. Purple and bicolored (purple and gray-blue) tourmalines shifted most effectively toward neon-blue hues (Fig. 1). This color evolution is attributed to the reduction of Mn^{3+}, responsible for reddish-purple tones, to Mn^{2+}, a much less intense chromophore. In the absence of significant amounts of Fe and Ti, this allows the blue color due to Cu^{2+} to emerge. In contrast, heat treatment of Cu-bearing tourmalines with high Ti and Fe contents tends to induce green coloration. Green samples heated up to 600°C exhibited only slight color variations, shifting toward yellowish-green tones, attributed to the strong absorption associated with the Mn^{2+}–Ti^{4+} pair.

Figure 1: Heat treatment of a Cu-bearing violet tourmaline in a reducing environment, with increasing temperatures at each heating cycle, until the desired color is achieved.

Further analyses, including single-crystal X-ray diffraction and electron paramagnetic resonance (EPR) spectroscopy, are currently planned to refine the crystal-chemical model of color origin in both natural and heat-treated Cu-bearing tourmalines.

A similar approach was recently successfully applied to the colorless neotype elbaite from Elba Island (acroite variety), to study the transition to the red rubellite variety induced by electron irradiation, and its subsequent return to colorless upon heating. The development of a high-resolution crystal-chemical model would allow for a deeper understanding of the physicochemical processes governing the characteristic neon-blue color of Paraíba tourmalines. Furthermore, it would support the elaboration of an analytical protocol capable of describing color evolution as a function of chemical composition and treatment conditions. Such an approach could also help differentiate treated material from natural specimens, contributing to greater transparency and regulation within the gem market.

References:

Bosi, F. (2018): Tourmaline crystal chemistry. American Mineralogist, **103**, 298–306.

Katsurada, Y., Sun, Z., Breeding, C.M., Dutrow, B.L. (2019): Geographic Origin Determination of Paraíba Tourmaline. Gems e Gemology, **55**, 648–659.

Laurs, B.M., Zwaan, J.C., Breeding, C.M., Simmons, W.B., Beaton, D., Rijsdijk, K.F., Befi, R., Falster, A.U. (2008): Copper- bearing (Paraíba-type) tourmaline from Mozambique. Gems & Gemology, **44**, 4-30.

Li, M., Hong, H., Yin, K., Wang, C., Cheng, F., Fang, Q. (2018): The Chemical States of Color-Induced Cations in Tourmaline Characterized by X-Ray Photoelectron Spectroscopy. Journal of Spectroscopy, ID 3964071.

Pezzotta, F. & Laurs, B.M. (2011): Tourmaline: The Kaleidoscopic Gemstone. Elements, **7(5)**, 333-338.

Rossman, G.R., Fritsch, E., Shigley, J.E. (1991): Origin of color in cuprian elbaite from São José de Batalha, Paraíba, Brazil. American Mineralogist, **76**, 1479-1484.

Light boron isotopic compositions of tourmaline from Jack Hills, Australia: Growth from multiple fluid sources

Dutrow, B.L.*[1], Gerdes, A.[2], Marschall, H.[2], Henry, D.J.[1], Loocke, M.[1], Cavosie, A.J.[3], Valley, J.W.[4]

[1]Department of Geology & Geophysics, Louisiana State University, Baton Rouge, LA, USA
[2]FIERCE Lab, Goethe-Universität, Frankfurt am Main, Germany
[3]School of Earth and Planetary Sciences, Curtin University, Perth, Australia
[4]Department of Geoscience, University of Wisconsin, Madison, WI, USA
* Corresponding author: *dutrow@lsu.edu*

Archean metaconglomerates and meta-sandstones of Jack Hills (JH), Western Australia, contain the oldest zircon recognized on Earth. After deposition between ca. 3050 – 2650 Ma, at least three metamorphic / fluid events are postulated with peak metamorphism of the JH metasediments about 2650 Ma. The fluid events likely included infiltration of an evolved, B-bearing fluid that enabled tourmaline (tur) to crystallize. To further understand the Neoarchean evolution of this part of the Narryer Terrane, a chemical, textural and isotopic study of the tourmaline that coexists with the Hadean detrital zircons was undertaken.

Heavy minerals separated from metaconglomerate sample 01JH42-2 (Cavosie et al. 2004) were examined with an associated thin section of the rock to provide a contextual basis for the occurrence of tourmaline. In thin section, the sample consists primarily of flattened quartz clasts with minor Cr-bearing muscovite defining the pervasive fabric. Trace detrital minerals in the section include chromite ($Chr_{39.3}Hc_{24.2}Zchr_{15.6}Ghn_{9.9}$), zircon, rutile, and monazite. Whole rock chemistry with SiO_2 = 96.4 wt% and K_2O = 0.62 wt % indicates a mature sedimentary protolith, consistent with the mineral assemblage (Cavosie et al. 2004). Additionally, two ~ 200 μm zoned tourmaline grains lie within the plane of the foliation and are oriented perpendicular to the apparent *c* axis. Mineral chemistry and textural analyses of these grains reveal five compositionally distinct zones with no detrital cores (Zones 1-5; Fig. 1a). Compositionally, all zones are alkali-group tourmalines and OH rich. Tourmalines are highly magnesian dravites with < 0.75 apfu Fe, variable Cr – $0.16 \leq Cr^{3+} \leq 0.52$ apfu, and 0.01 V apfu. Each zone (Z) has a distinct composition and when plotted on the AFM suggest equilibrium host rock compositions (Henry & Guidotti 1985): zones 1 and 2 have the highest X_{Mg} = 0.922 and 0.916, respectively, and have compositions consistent with formation in Cr-, V- metasediments, are concentric and likely reflect prograde growth; zone 3 contains the highest Fe and lowest X_{Mg} = 0.75, and cross cuts zones 1 and 2. Zones 4 and 5 have X_{Mg} = 0.80 and 0.77, are consistent with compositions in Al-rich metapsammites and replace earlier generations. Using $\delta^{18}O$ in tur and quartz, determined by laser fluorination (Cavosie et al. 2005) and the Matthews et al. (2003) temperature (T) formulation, yields T = 430 – 455°C. These data provide the background for additional B isotopic studies on the grain mounts.

Boron, a fundamental element for tourmaline formation, is a fluid-mobile element with two stable isotopes ($^{11}B/^{10}B$) that have a large relative mass difference. Such a difference results in isotopic fractionation during mineral-fluid interactions. As such, B isotopes are used to investigate fluid-mediated processes and are ideal for evaluating elusive fluids interacting with tourmaline. Heavy minerals separated from ~ 2 kg of the same sample yield an additional 52 grains of tourmaline that were mounted, imaged in BSE, and analyzed for major and minor element chemistry by EMP prior to B isotopic analyses. All grains are of similar size, ≤ ca. 250 μm, chemically zoned, and oriented both parallel and perpendicular to an apparent *c* axis. Thirty-two grains were suitable for isotopic analyses and 45 measurements were obtained using a 193 nm RESOlution ArF excimer laser (COMpex Pro 102) coupled to a ThermoScientific Neptune Plus multi-collector ICP-MS at the FIERCE Laboratory at the Goethe University. $\delta^{11}B$ is reported relative to NIST SRM951 in ‰ via normalizing to IAEA B4 schorl as a primary reference material. Propagated uncertainties (excess variance of primary RM over > 10 hrs plus analytical error) of the analyses are near 0.16 ‰ (2 sd; standard deviations). Nineteen analyses on Harvard elbaite yielded a weighted mean $\delta^{11}B$ =

-10.82 ± 0.04 ‰ (2 sd = 0.17 ‰). Standard deviations calculated for each JH analysis are near 0.13‰ (1 sd). The analytical spot was a 10 μm square.

δ^{11}B values ranged from -19.23 ± 0.13 to -9.57 ± 0.13 with most analyses from -17.5 to -16.5. One tourmaline grain with an obvious core and rim in BSE (Fig. 1b) displays significant chemical and B isotopic zoning: the outer core (Z1) has X_{Mg} = 0.94 and δ^{11}B = -14.24 ± 0.19; an average for the rim (Z2) has X_{Mg} = 0.92, and δ^{11}B = -17.41 ± 0.16 (Fig. 1b). Chemical composition, determined for Zones 1-5 in thin section, was used to infer the zonal relationships. This dramatic shift in δ^{11}B follows the clear change in the mineral chemistry, including an increase in Cr_{tot} and a decrease in Al_{tot} ($CrAl_{-1}$). The outer rim, with its lighter δ^{11}B than the core (Z 1 and 2), could reflect tur formation by prograde dehydration with B supplied by clays or micas, as has been noted in high temperature-pressure rocks (e.g. Marschall et al. 2009). Episodic availability of chemically and isotopically distinct fluids suggests that the later generations of tourmaline (Z 3- 5) that crosscut Z 1-2 result from hydrothermal / magmatic, externally derived fluids. A substantial 12‰ variation across the measured δ^{11}B supports fluid-mineral interactions. These data provide the first boron isotopic analyses of late Archean tourmaline from the metaconglomerates of the Jack Hills area.

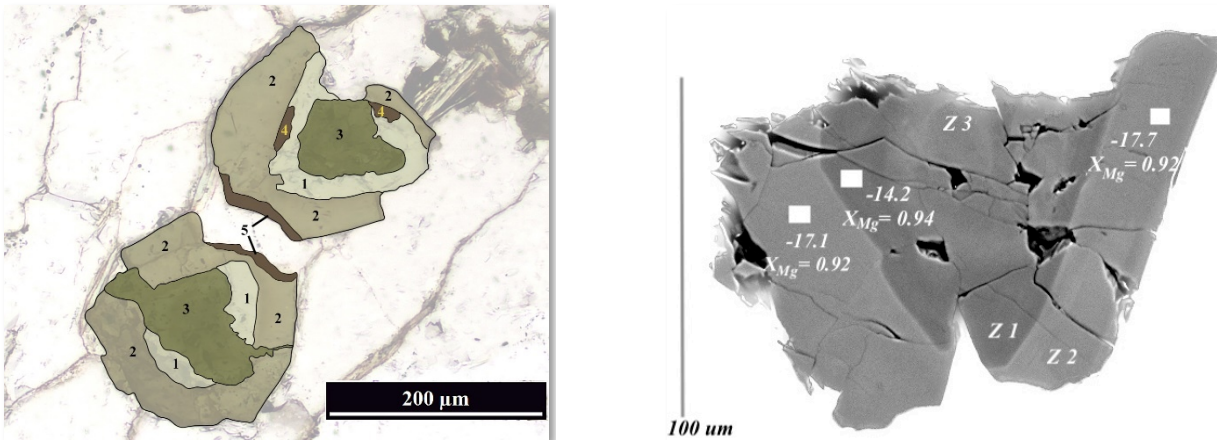

Figure 1: Tourmaline grains from Jack Hills, Australia, sample 01JH42-2. (a. left) Two small tourmaline grains in thin section, PPL, showing an interpretive overlay of the five generations of tourmaline (labeled 1-5) distinguished by major and minor element chemistry. Matrix is quartz with minor muscovite. (b. right) Backscattered electron image of a zoned tourmaline grain with a distinct inner and outer core, and rim, labeled with δ^{11}B values and X_{Mg} of the EMP analyses. Zone chemistry correlates with those on the right; Z 1 is the outer core, Z 2 the rim, Z3 replaced core.

References

Cavosie A., Valley J., Wilde S. and E.I.M.F. (2005) Magmatic δ^{18}O in 4400-3900 Ma detrital zircons: A record of the alteration and recycling of crust in the Early Archean. *Earth and Planetary Science Letters,* 235, 663-681.

Cavosie A., Wilde S, Liu D., Weiblen P. and Valley J. (2004) Internal zoning and U-Th-Pb chemistry of Jack Hills detrital zircons: a mineral record of early Archean to Mesoproterozoic (4348-1576 Ma) magmatism. *Precambrian Research*, 135, 251-279.

Henry, D.J. and Guidotti, C.V. (1985) tourmaline as a petrogenetic indicator mineral: an example. From the staurolite-grade metapelites of NW Maine. *American Mineralogist*, 70, 1-15.

Marschall, H., Korsakov, A., Luvizotto, G., Nasdala, L. and Ludwig, T. (2009) On the occurrence and boron isotopic composition of tourmaline in (ultra)high-pressure metamorphic rocks. *J. Geological Society, London,* 166, 811-823.

Matthews A., Putlitz B., Hamiel Y. and Hervig R. (2003) Volatile transport during the crystallization of anatectic melts: Oxygen, boron and hydrogen stable isotope study on the metamorphic complex of Naxos, Greece. *Geochimica et Cosmochimica Acta,* 67, 3145–3163.

A potentially new tourmaline of liddicoatite composition

Skřápková, L.[1*], Cempírek, J.[1], Škoda, R.[1], Holá, M.[2], Novotný, F.[1] and Bosi, F.[3]

[1]Department of Geological Sciences, Faculty of Science, Masaryk University, Kotlářská 2, 611 37 Brno, Czech Republic
[2]Department of Chemistry, Faculty of Science, Masaryk University, Kotlářská 2, 61137 Brno, Czech Republic
[3]Dipartimento di Scienze della Terra, Sapienza Università di Roma, Piazzale Aldo Moro 5, I–00185, Rome, Italy

*Corresponding author: lenkas@sci.muni.cz

Tourmaline of liddicoatite composition, ideally $Ca(Li_2Al)Al_6(Si_6)(BO_3)_3O_{18}(OH)_3(OH)$, is a potentially new tourmaline species from the elbaite-subtype pegmatite Dolní Rožínka, Czech Republic. The name liddicoatite was formerly used for a species that is F-dominant and was therefore redefined as fluor-liddicoatite (Henry et al., 2011). Liddicoatite is currently not an approved species. In Dolní Rožínka, liddicoatite formed during the final stages of pegmatite crystallisation; the residual fractionated fluids escaped from the pegmatite pockets and reacted with minerals in the graphic unit (plagioclase and primary schorlitic tourmaline). Liddicoatite was found as colourless oscillatory zoned rims of green (fluor-liddicoatite) and brown (Fe-rich fluor-elbaite) tourmaline; it is associated with elbaite, albite, and K-feldspar (Fig. 1).

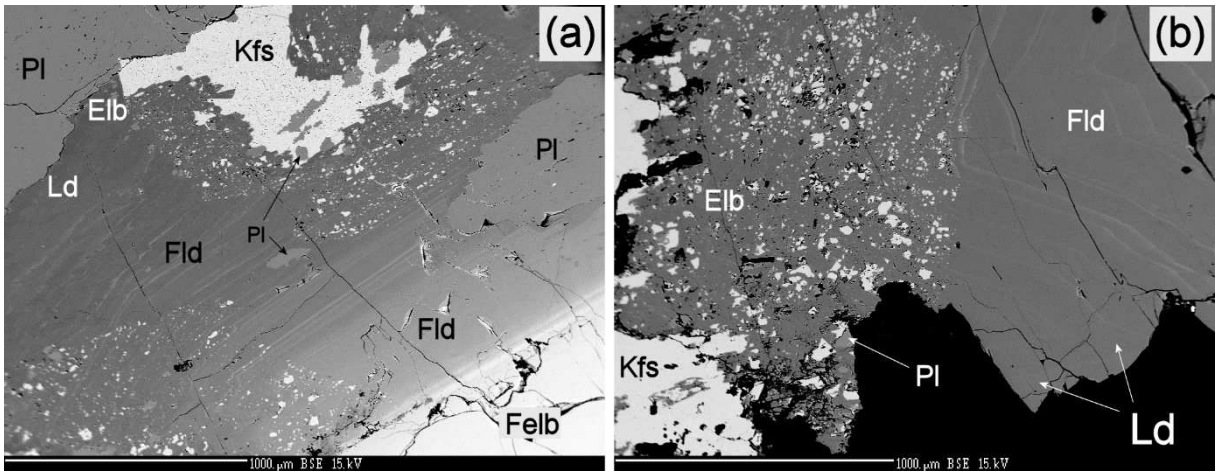

Figure 1. The back-scattered electron (BSE) image of liddicoatite (Ld) associated with fluor-liddicoatite (Fld), elbaite (Elb), plagioclase (Pl), K-feldspar (Kfs) and fluor-elbaite (Felb).

The tourmaline forms anhedral crystals ca. 1 mm in diameter, colourless with a vitreous to transparent lustre, conchoidal fracture and white streak. It has the Mohs hardness of ca. 7, the calculated density of 3.047 $g.cm^{-3}$ and is uniaxial with $\omega = 1.641(1)$, $\varepsilon = 1.634(1)$ at 589 nm white LED light, pleochroism was not observed.

The tourmaline has trigonal symmetry, space group *R3m*, $a = 15.8277(3)$ Å, $b = 15.8277(3)$ Å, $c = 7.09850(10)$ Å, $V = 1540.07\ (6)$ $Å^3$ and $Z = 3$. The crystal structure was refined to $R_1 = 1.44$ % using 1846 unique reflections collected with Mo*K*α X-ray source. The chemical composition was analysed using EPMA and LA-ICP-MS.

The empirical formula calculated on the basis of Y+Z+T = 15 apfu and 31 apfu (OH, F, O). The structural refinement showed full occupancies of the Y-, Z-, and T-sites, resulting in the final empirical formula: $^{X}(Ca_{0.432}Na_{0.378\ \ 0.190})_{\Sigma 1.000}\ ^{Y}(Li_{1.519}Al_{1.415}Fe_{0.051}Mn_{0.015})_{\Sigma 3.000}\ ^{Z}Al_6\ ^{T}(Si_{5.874}Al_{0.126})_{\Sigma 6.000}O_{18}\ ^{B}(BO_3)_3\ ^{V}(OH)_3\ ^{W}(OH_{0.592}F_{0.390}O_{0.018})_{\Sigma 1.000}$

The structurally constrained OH-content at the W position in the general tourmaline formula (corresponding to the O1 site), observed by Raman spectroscopy, was verified and calculated using the equation provided by Bosi (2013): $^{W}(OH) = 2 - [1.01\ BVS(O1)] - 0.21 - F$. The equation proved an OH-content of 0.50 apfu, which is slightly lower than the value obtained by EMPA and LA-ICP-MS (0.59 apfu) yet still supports the presence of significant $^{W}(OH)$ at the O1 site.

The ideal formula of the potentially new tourmaline conforms to both the dominant-valency and dominant-constituent rules (Bosi et al., 2019). The dominant end-member approach (Hawthorne, 2023) provided an identical result. Based on the analysis, the structural formula contains 43.2 mol. % of the end-member (limited by the 0.432 apfu Ca at the X-site). However, the studied thin section showed a great compositional variability of the crystal (Fig. 2), reflecting the progressive trend of fractionation.

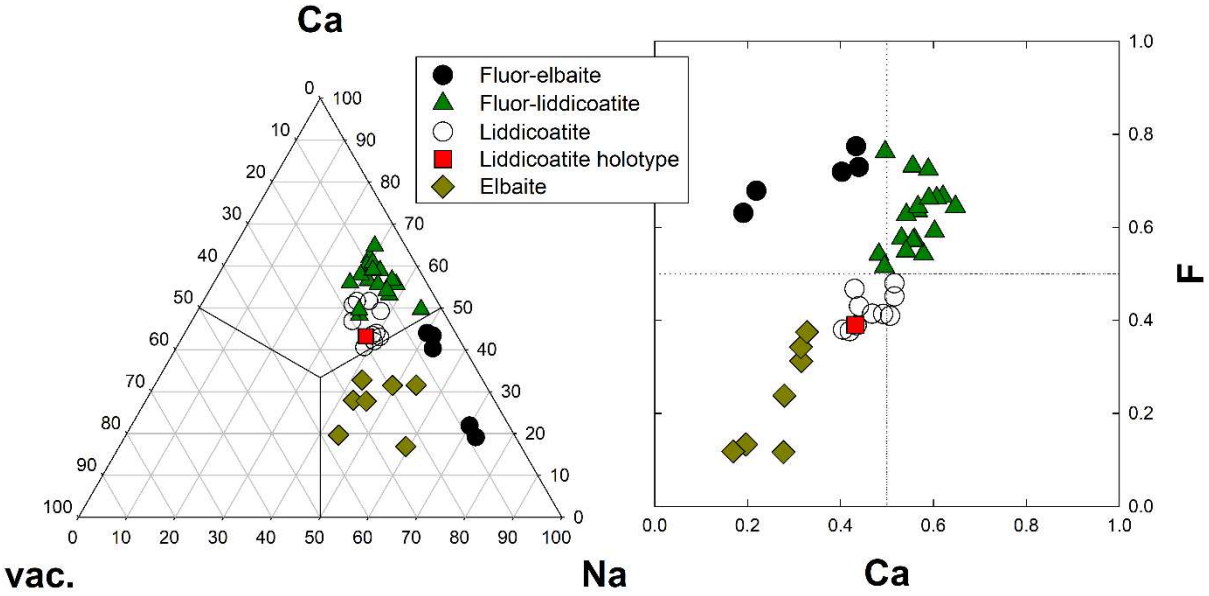

Figure 2. The diagrams showing the compositional variations of tourmaline in the analysed thin section.

The closest end-member compositions of valid tourmaline species are fluor-liddicoatite, elbaite, rossmanite, and darrellhenryite, related by the substitutions: $^{W}F^{-} \rightarrow {}^{W}(OH)^{-}$; $^{X}Na^{+} + {}^{Y}0.5Al^{3+} \rightarrow {}^{X}Ca^{2+} + {}^{Y}0.5Li^{+}$; $^{X}\square + {}^{Y}Al^{3+} \rightarrow {}^{X}Ca^{2+} + {}^{Y}Li^{+}$; and $^{X}Na^{+} + {}^{Y}Al^{3+} + {}^{W}O^{2-} \rightarrow {}^{X}Ca^{2+} + {}^{Y}Li^{+} + {}^{W}(OH)^{-}$; respectively.

Proposal for potential new mineral species of the tourmaline supergroup, liddicoatite, was submitted for approval to IMA-CNMNC in May 2025. The research was supported by the project Horizon - Li4Life (no. 101137932)

References:

Bosi, F. (2013) – Bond-valence constraints around the O1 site of tourmaline. *Mineralogical Magazine*, 77, 343-351.

Bosi, F., Biagioni, C. and Oberti, R. (2019) – On the chemical identification and classification of minerals. *Minerals*, 9, 591.

Hawthorne, F. (2023) – On the definition of distinct mineral species: A critique of current IMA-CNMNC procedures. *Mineralogical Magazine*, 87, 494-504.

Henry, D.J., Novák, M., Hawthorne, F.C., Ertl, A., Dutrow, B.L., Uher, P., and Pezzotta, F. (2011) – Nomenclature of the tourmaline-supergroup minerals. *American Mineralogist*, 96, 895–913.

Tourmaline associated with orogenic gold prospects in the Silet terrane, South Algeria: contrasting composition and redox state during hydrothermal evolution

Ismahen Chaouche[1,2*], Jan Cempirek[3], Mohamed Talbi[1,2], Riad Ben El Khaznadji[1,2], Nadjet Ait Taleb[1,2], Yves Fuchs[4]

[1]Laboratoire de métallogénie et de magmatisme d'Algérie (LMMA). Geology department, *FSTGAT/ USTHB.* BP 32, El Alia, 16111, Bab Ezzouar, Algiers, Algeria
[2] Faculté des Sciences de la Terre, Géographie et de l'Aménagement du Territoire, Geology department, *(FSTGAT)* Université des Sciences et Technologie Houari Boumediène (*USTHB)*. BP 32, El Alia, 16111, Bab Ezzouar, Algiers, Algeria.
[3]Department of Geological Sciences, Masaryk University, Kotlářská 2, 611 37 Brno, Czech Republic
[4]Université Gustave Eiffel, 2 allée du Promontoire, 93160 Noisy-le-Grand, France.
* Corresponding author: *ismahane.chaouche@usthb.edu.dz; chasane@gmail.com*

Tourmaline frequently occurs in close association with gold-bearing hydrothermal systems in various deposits worldwide, including the Hoggar gold occurrences in southern Algeria (Chaouche et al., 2025). The two terranes of Silet and LATEA (**L**aouni, **A**zrou-n-Fad, **T**efedest, and **E**géré-**A**leksod) contain numerous gold occurrences/prospects (Figure 1), where tourmaline is the most common mineral associated with the quartz lodes. Similar to the studied Idreksi, Seldrar and Assouf Mellen occurrences in **Silet Terrane,** tourmaline was also observed at In-Abeggui prospects in **Laouni Terrane**.

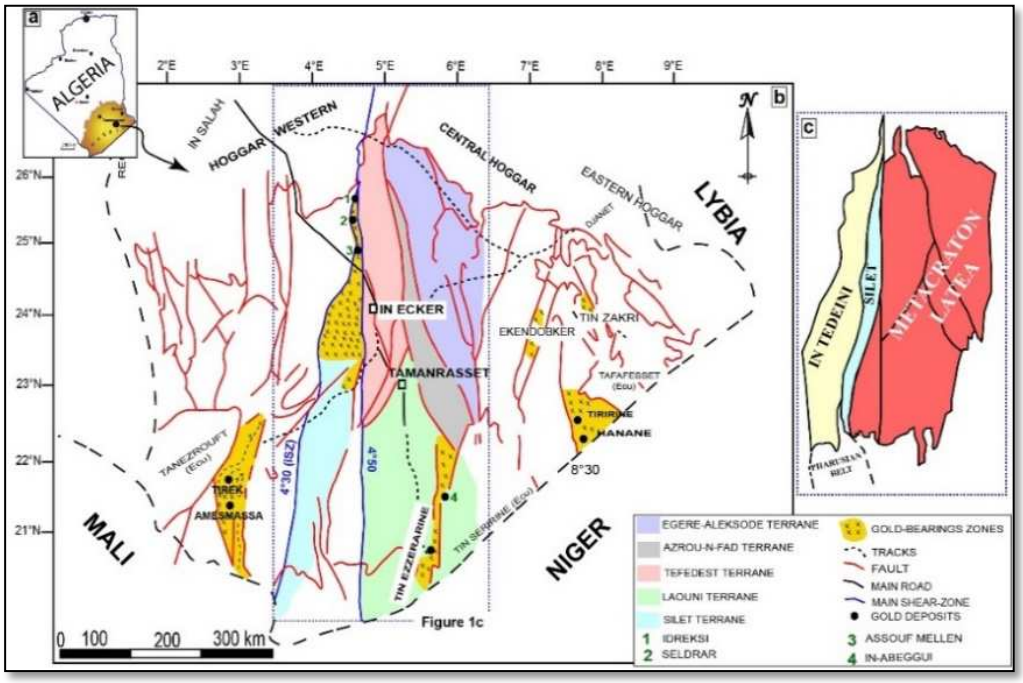

Figure 1: Location of major gold deposits in Hoggar. (a) Geographic location of Hoggar. (b) Locations of gold deposits and occurrences along the main shear zones 4◦50 and 4◦30 (ORGM, 2004). (c) Simplified map showing the locations of the Silet Terrane and the metacraton LATEA (blue rectangle).

In the Assouf Mellen, Seldrar, and Idreksi, gold-bearing veins cut diorite and granodiorite complexes of the pre-orogenic Tonalite-Trondhjemite-Granodiorite group (868–840 Ma). The localities typically feature two quartz generations (Chaouche, 2008; Marignac et al., 2016; Chaouche et al., 2025): early quartz I was thoroughly brittle-deformed, yielding saccharoidal microcrystalline quartz II. New data show that quartz II typically hosts fibrous tourmaline (Chaouche et al., 2025), frequently

representing the only tourmaline generation in Idreksi and Assouf Mellen occurrences. However, the tourmaline from Seldrar has two textural generations (Tur I and Tur II), distinct in texture and composition (Figs. 2a-b). The style of zoning (patchy and sector zoning in their cores, fibrous rims) and presence of fine-grained aggregates (Fig. 2b) found in the studied samples are commonly observed in hydrothermal orogenic gold deposits (Sciuba et al., 2021; Gauriau et al., 2022).

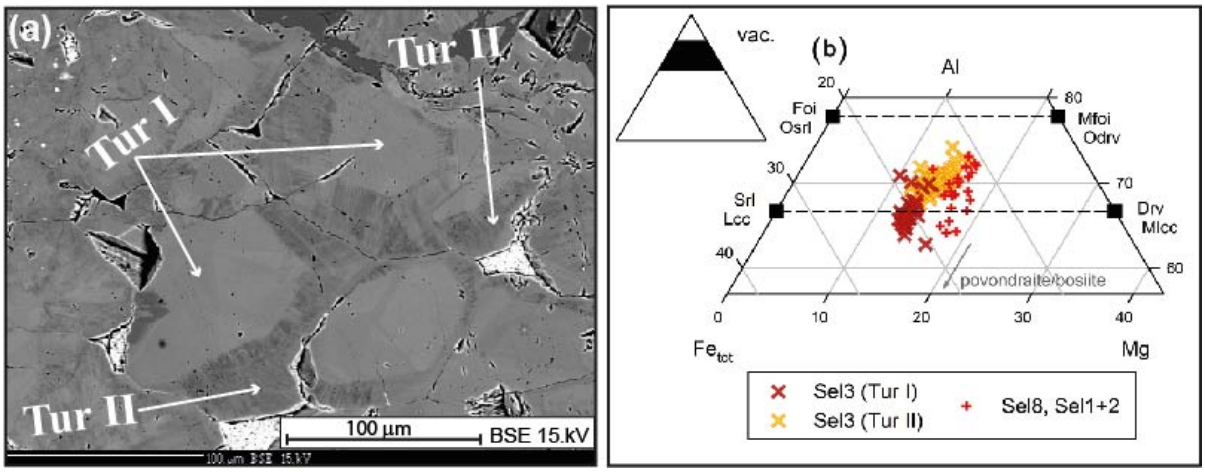

Figure 2: Seldrar tourmaline texture and composition (a)Sector zoning of tourmaline crystals in cuts perpendicular to their prisms. (b) The occupancy of octahedral Y + Z sites (Mg vs. Al vs. total Fe) in Seldrar tourmaline

Based on the mineral chemistry, the Silet tourmaline belongs to the alkali group and represents the schorl–dravite and foitite–oxy-foitite series and shows evolution trends to bosiite/povondraite; tourmaline components from the calcic group (lucchesiite, magnesio-lucchesiite) are minor only. Tourmaline in Silet Terrane was likely formed as Al- deficient Fe^{3+}-enriched schorl (Tur I), later recrystallized (Tur II) and enriched in Mg and Al with higher X- site vacancy (Mg-rich schorl to Fe-rich dravite).

In the studied region, free gold is present as inclusions disseminated in quartz and tourmaline and as fissure-fillings in deformed tourmaline crystals. It was also found as inclusions in chalcopyrite and iron oxides. In the Seldrar occurrences, gold is associated with tourmaline with high initial Fe^{3+}-contents (Tur I), while the assemblage of the later Tur II is barren. The evolution towards Fe^{3+}-rich schorl may be explained as a result of more oxidizing conditions in the late stage of formation of the mineralized quartz veins. Furthermore, the presence of native gold on fractures in quartz II and in fibrous tourmaline II shows that it formed very late during the two-stage formation process. Low-temperature weathering processes remobilized part of the gold.

References

Chaouche I (2008) - Apport de la minéralogie des tourmalines a la métallogénie de l'or. Exemples des indices du terrane d'Iskel (Hoggar occidental) USTHB-Alger, Algeria, 90p. Unpublished Magister Thesis.

Chaouche, I., Cempírek, J., Talbi, M., El Khaznadji, R. B., Ait Taleb, N., and Fuchs, Y. (2025) - Tourmaline associated with orogenic gold occurrences in the Silet terrane, South Algeria: Evolution of composition and redox state during hydrothermal crystallization. *Geochemistry*, 126259.

Gauriau, J., Harlaux, M., André-Mayer, A.S., Eglinger, A., Richard, A., Fontaine, A., Lefebvre, M.G., Villeneuve, J. and Lemarchand, D. (2022) - Chemical and boron isotope composition of tourmaline from the Kiaka orogenic gold deposit (Burkina Faso, west African craton) as a proxy for ore-forming processes. *Mineral. Deposita* 1-20.

Marignac, C., Aissa, D.E., Bouabsa, L., Kesraoui, M. and Nedjari, S. (2016) - The Hoggar gold and rare metals metallogenic province of the Pan-African Tuareg shield (Central Sahara, South Algeria): An early Cambrian echo of the late Ediacaran Murzukian event? In: Bouabdellah, M., Slack, J.F. (Eds.), Mineral Deposits of North Africa. Springer, Cham, pp. 371–404

Sciuba, M., Beaudoin, G., Grzela, D., Makvandi, S. (2021)- Chemical composition of tourmaline in orogenic gold deposits. Mineral. Deposita 56, 537–560.

Stable isotopes in tourmaline

Robert B. Trumbull*

GFZ Helmholtz Centre for Geosciences, Telegrafenberg, 14473 Potsdam, Germany

*Corresponding author: bobby@gfz.de

For the 3rd International Conference on Tourmaline, Marschall (2021) reviewed progress in isotope studies since Marschall and Jiang (2011). This contribution reviews advances since then, with emphasis on the fluid-mobile elements B, O, Li, H for which tourmaline is a uniquely well-suited host thanks to its wide stability range and ability to react to changing conditions by zoning (Dutrow and Henry, 2011).

Boron: The lion's share of stable isotope studies still falls to the boron isotopes ^{11}B and ^{10}B, whose natural abundance ratio is about 4:1. The $^{11}B/^{10}B$ ratios are reported as $\delta^{11}B$ in permil relative to a boric acid standard. In-situ boron isotope analyses of tourmaline are made by laser ablation inductively coupled plasma mass spectrometry (LA-ICPMS) or secondary ion mass spectrometry (SIMS). Most recent studies used the former because the instruments are less expensive and simpler to run. SIMS has the advantage of a smaller beam size and shallower penetration depth so it is the method of choice for fine-grained and complexly-zoned material. Several tourmaline standards exist for B-isotope analyses (Marschall 2021) and the "Harvard set" has also been characterized for O- and Li-isotope work (Wiedenbeck et al., 2021).

Boron isotope analyses of tourmaline can be regarded as routine, with several studies being published each year. Combined with major- and trace-element data, B-isotopes help decipher fluid sources and fluid-mediated processes of metamorphism (Krmicek et al., 2021; Chen et al., 2023). An ongoing focus is on granite-related systems and the magmatic-hydrothermal transition (Ribacki et al., 2022; Zhao et al., 2022; Hohf et al., 2023; Wu et al., 2023; Sun et al., 2024; Li et al., 2025). However, the latter studies and others of that kind suffer from a lack of reliable B-isotope fractionation factors between granitic melts and aqueous fluid. Experiments by Hervig et al. (2002) and Maner and London (2018) predicted a strong melt-fluid fractionation factor (-5‰ at 700°C). However, Cheng et al. (2022) determined a tourmaline-melt factor of +0.9‰ at 660°C, which combined with the tourmaline-fluid factor of -1 ‰ at 660°C (Meyer et al., 2008) predicts a very low melt-fluid fractionation. This is also in line with empirical studies and knowledge of boron coordination in tourmaline, granitic melt and aqueous fluid.

The diagnostic power of B-isotope data alone is limited (Marschall, 2021 and the trend now is toward combined isotope studies. Although still few in number, there examples below show the value of this approach:

***Oxygen*:** The stable isotopes of oxygen and their natural abundances are ^{16}O (99.76%), ^{17}O (0.04%) and ^{18}O (0.2%). The $^{18}O/^{16}O$ and $^{17}O/^{16}O$ ratios are expressed as $\delta^{18}O$ and $\delta^{17}O$, resp., relative to standard mean ocean water. All tourmaline studies to date dealt with $\delta^{18}O$ only. In-situ analyses in tourmaline are currently not possible by LA-ICPMS (but see Liu et al., 2025). SIMS can generate $\delta^{18}O$ values with a precision of 0.2 ‰ for a spot size of 10 microns, but a chemical matrix effect can cause much larger uncertainty (1-2 ‰; Marger et al., 2019; Wiedenbeck et al., 2021). A two permil uncertainty limits the usefulness of O-isotopes for geothermometry but the data can be critical to distinguish fluid sources and processes as shown by the combined B-O isotope studies of granite-related tin deposits by Hong et al. (2020) and Harlaux et al. (2021).

Lithium: The isotopes ^{7}Li and ^{6}Li have natural abundances of 92.4% and 7.6%, respectively; their ratio is expressed as $\delta^{7}Li$ relative to the lithium carbonate standard L-SVEC. Studies combining Li and B isotope analyses of tourmaline have so far been made using mineral separates and solution ICPMS (Chakraborty and Upadhyay, 2020; Xiang et al., 2020). Both studies showed that $\delta^{7}Li$ is more sensitive to changes in the system than $\delta^{11}B$ because minerals other than tourmaline can be important. Lithium isotopes can be analyzed by SIMS now that tourmaline standards are established (Wiedenbeck et al., 2021). Also, the LA-ICPMS method for Li isotope analyses in tourmaline was established by Lin et al. (2019). Applications of in-situ analyses have been slow in coming but with the current boom of interest in Li resources, this is likely to change soon.

Hydrogen: Deuterium ^{2}H and hydrogen ^{1}H have natural abundances of about 0.015% and 99.989%, respectively. The D/H ratio (δD relative to standard mean ocean water) varies in water and hydrothermal fluids by more than 100 permil. Tourmaline H- and B-isotope analyses reported by Adlahka et al. (2017) were used to distinguish fluid sources in the McArthur River uranium deposit. Zall et al. (2019) reported combined B-O-H isotope data from different tourmaline types associated with a two-mica granite. The signature of all three isotope systems concurred with a magmatic source. The cited studies employed mineral separates for the O- and H- analyses and in-situ methods for B-isotopes, which is not ideal for complex tourmaline paragenesis. In-situ analysis by SIMS is possible and exploratory work was done in the Potsdam lab (Xavier et al., 2013) but the 100% mass difference between the two isotopes causes challenges with matrix effects and secondary beam stability and hydrogen diffusion in tourmaline may also be an issue (Jibao and Yaquian, 2019). To the author's knowledge no tourmaline standards for H-isotope analyses have been properly characterized (the Harvard tourmalines have a single reference value and no homogeneity tests). This should be a priority topic for future work.

References

Adhlahka, E.E., Hattori, K., Davis, W.J. and Boucher, B. (2017) - Characterizing fluids associated with the McArthur River U deposit, Canada based on tourmaline trace element and stable (B, H) isotope compositions. *Chemical Geology*, 466, 417-4352017

Chakraborty, T. and Upadhyay, D. (2020) - The geochemical differentiation of S-type pegmatites: constraints from major–trace element and Li–B isotopic composition of muscovite and tourmaline. *Contributions to Mineralogy and Petrology,* 175, 60.

Chen, X., Jiang, S.J., Palmer, M.R., Schertl, H-P., Cambeses, A., Hernández-Uribe, D., Zhao, K., Lin, C. and Zheng, Y. (2023) - Tourmaline chemistry, boron, and strontium isotope systematics trace multiple melt–fluid–rock interaction stages in deeply subducted continental crust. *Geochimica et Cosmochimica Acta*, 340, 120-140.

Cheng, L., Zhang, C., Zhou, Y, Horn, I., Weyer, S., and Holtz, F. (2022) - Experiments reveal enrichment of ^{11}B in granitic melt resulting from tourmaline crystallisation. *Geochemical Perspectives Letters*, 20, 37-42.

Dutrow, B.L. and Henry, D.J. (2011) Tourmaline: a geologic DVD. *Elements*, 7, 301-306.

Harlaux M., Kouzmanov K., Gialli S., Marger, K., Bouvier, A-S., Baumgartner, L.P., Rielli, A., Dini, A., Chauvet, A., Kalinaj, M. and Fontboté, L. (2021) - Fluid mixing as primary trigger for cassiterite deposition: Evidence from in situ $\delta^{18}O$–$\delta^{11}B$ analysis of tourmaline from the world-class San Rafael tin (-copper) deposit, Peru. *Earth and Planetary Science Letters*, 563, 116889.

Hervig, R.L., Moore, G.M., Williams, L.B., Peacock, S.M., Holloway, J.R. and Roggensack, K. (2002) - Isotopic and elemental partitioning of boron between hydrous fluid and silicate melt, *American Mineralogist*, 87, 769-774.

Hohf, M., Trumbull, R.B., Cuadra, P. and Solé, M. (2023) - Tourmaline breccias from the Río Blanco-Los Bronces porphyry copper district, Chile: constraints on the fluid source and the utility of tourmaline composition for exploration. *Economic Geology*, 118, 779-800.

Hong, W., Fox, N., Cooke, D.R., Zhang, L. and Fayek, M. (2020) - B- and O-isotopic compositions of tourmaline constrain late-stage magmatic volatile exsolution in Tasmanian tin-related granite systems. *Mineralium Deposita*, 55, 53-78.

Jibao, G. and Yaquian, Q. (1997) - Hydrogen isotope fractionation and hydrogen diffusion in the tourmaline-water system. *Geochimica et Cosmochimica Acta*, 61, 4679–4688.

Krmíček, L., Novák, M., Trumbull, R.B., Cempírek, J. and Houzar, S. (2021) - Boron isotopic variations in tourmaline from metacarbonates and associated calc-silicate rocks from the Bohemian Massif: constraints on boron recycling in the Variscan orogen. Geoscience Frontiers, 12, 219-230

Li, L., Wang, L., Romer, R.L., Ma, C., Cao, L. and Tian, Y. (2025): Using tourmaline to trace Li mineralization in the Mufushan granitic batholith, South China. - Chemical Geology, 671, 122485.

Lin J., Liu Y., Hu, Z., Chen, W., Zhang, C., Zhao, K. and Jin, X. (2019) - Accurate analysis of Li isotopes in tourmalines by LA-MC-ICP-MS under "wet" conditions with non matrix-matched calibration. *Journal of Analytical and Atomic Spectrometry*, 34, 1145-1153.

Liu, Z, Lin, J., Jiang, X., Zhu, X., Liu, W., Liu, Y., Zhang, W. and Hu, Z. (2025) First attempt to determine oxygen isotopes in oxygen by MC-ICP-MS. Journal of Analytical Atomic Spectrometry, 40, 1192-1202.

Maner, J.L. and London, D. (2018) - Fractionation of the isotopes of boron between granitic melt and aqueous solution at 700 °C and 800 °C (200 MPa). *Chemical Geology*, 489, 16-27.

Marger, K., Luisier, C., Baumgartner, L.P., Putlitz, B., Dutrow, B.L., Bouvier, A-S. and Dini, A. (2019) - Origin of Monte Rosa whiteschist from in-situ tourmaline and quartz oxygen isotope analysis by SIMS using new tourmaline reference materials. *American Mineralogist*, 104, 1503-1520.

Marschall, H.R. (2021) - Tourmaline isotopes – ten years left behind. TUR2021 3rd International Conference on Tourmaline. *NATURA* 111 (1): 67-70.

Marschall, H.R. and Jiang, S.-Y. (2011) - Tourmaline isotopes: No element left behind. *Elements*, 7, 313–319.

Meyer, C., Wunder, B., Meixner, A., Romer, R.L. and Heinrich, W. (2008) - Boron-isotope fractionation between tourmaline and fluid: an experimental re-investigation. *Contributions to Mineralogy and Petrology*, 156, 259-267.

Ribacki, E., Trumbull, R.B., Lopez de Luchi, M.G. and Altenberger, U. (2022) - The chemical and B-isotope composition of tourmaline from intra-granitic pegmatites in the Las Chacras-Potrerillos Batholith, Argentina. *Canadian Mineralogist*, 60, 49-66

Sun, W., Zhao, Z. Mo, X, Dong, G., Li, X., Yuan, W., Wang, T., Wang, B., Pan, T., Han, J., Zheng, F. and Tang, Y. (2024) - Tourmaline as an indicator for pegmatite evolution and exploration: A case study from the Chakabeishan deposit, northeastern Tibetan Plateau. *Ore Geology Reviews*, 165, 105892.

Wiedenbeck M., Trumbull R. B., Rosner, M., Boyce, A., Fournelle, J.H., Franchi, A., Halama, R., Harris, C., Lacey, J.H., Marschall, H., Meixner, A., Pack, A., Pogge von Strandmann, P.A.E., Spicuzza, M.J., Valley, J.W. and Wilke, F.D.H. (2021) – Tourmaline reference materials for the in situ analysis of oxygen and lithium isotope ratio compositions. *Geostandards and Geoanalytical Research*, 45, 97-119.

Wu, Y-S, Zhao, K-D, Deng, X-H., Zhao, H-D., Santosh, M. and Chen, Y-J. (2023) - Chemistry and boron isotope composition of tourmaline as a robust tool to characterize the origin of porphyry molybdenum systems: The case of Donggebi deposit in East Tianshan, China. *Ore Geology Reviews*, 163, 105760.

Xavier, R.P., Trumbull, R.B., Wiedenbeck, M. and Monteiro, L.V.S. (2013) Sources of mineralizing fluids in Cu-Au systems from the Carajás Mineral Province (Brazil): constraints from in-situ microanalysis of hydrogen and boron isotopes in tourmaline. *12th SGA Biennial Meeting*, Uppsala, 12-15.

Xiang, L., Romer, R.L., Glodny, J., Trumbull, R.B. and Wang, R. (2020) - Li and B isotopic fractionation at the magmatic-hydrothermal transition of highly evolved granites. *Lithos*, 376-377.

Zall, F., Tahmasbi, Z., Jiang, S-Y., Danyushevsky, L.V. and Harris, C. (2019) - Elemental and B-O-H isotopic compositions of tourmaline and associated minerals in biotite-muscovite granite of Mashhad, NE Iran: Constraints on tourmaline genesis and element partitioning. *Lithos*, 324-325, 803-820.

Zhao, Z., Yang, X., Zhang, T., Lu, Y., Li, W. and Zhang, Z. (2022) - Geochemical characteristics and boron isotopes of tourmaline from the Baishaziling tin deposit, Nanling Range: Constraints on magmatic-hydrothermal processes. *Ore Geology Reviews*, 142, 104695.

Petrology of tourmaline in granitic pegmatites

Cempírek, J.*, Novák, M., Skřápková, L.

Department of Geological Sciences, Faculty of Science, Masaryk University, Kotlářská 2, 611 37 Brno, Czech Republic

*Corresponding author: jcemp@sci.muni.cz

Evolution of granitic pegmatites is a complex process that includes transition from the magmatic to hydrothermal stage, and spans over a large range of PT conditions from the magmatic stage (~700-400 °C) via early subsolidus (~400-300 °C) to the late subsolidus stage down to ~100-200 °C, and P from ~0.5 to ~5 kbar. High availability of B, Al, F and cations compatible with the tourmaline crystal structure in pegmatitic melts and related late-stage hydrothermal fluids, results in common tourmaline occurrence in pegmatites and their exocontacts. The large span of genetic conditions and large changes in local composition of tourmaline-forming systems during pegmatite solidification result in large textural-paragenetic variability of tourmaline and in wealth of mineral species of the tourmaline supergroup present in pegmatites. Textural and compositional trends of tourmaline are well known in the pegmatites affiliated to the LCT (Li-Cs-Ta) petrogenetic family, including simple barren, beryl-columbite± phosphate, Li-rich lepidolite-, elbaite-, petalite- and spodumene- subtypes, and miarolitic pegmatites (e.g., Jolliff et al., 1986; Novák & Povondra, 1995; Selway et al., 1999; Tindle et al., 2002, 2005). Tourmalines from NYF (Nb-Y-F) pegmatites (Novák et al., 2011), and primitive anatectic pegmatites (Gadas et al., 2012) have been only sporadically examined mainly due to scarcity of tourmalines in these types of pegmatites.

Due to its refractory behavior, tourmaline often serves as an indicator of geological processes in multi-stage mineral assemblages. While the evolution of primary tourmalines from pockets and from endocontact and exocontact zones is well studied, the role of subsolidus replacement assemblages is rather poorly known. The large number of paragenetic, textural, morphological, and compositional types of tourmalines in granitic pegmatites requires a very careful approach to sampling and thorough study of mineral assemblages, textural relations and mainly internal zoning in BSE images and especially element maps to get reliable conclusions.

Evolution of tourmaline in granitic pegmatites

We compare the evolution of tourmaline from barren pegmatites to those from the LCT family, as interaction with the host rock is usually limited; the evolution of tourmaline in NYF pegmatites is addressed in another talk at this event.

Barren pegmatites*:* Very simple evolution trend of tourmaline from Mg- to Fe,Al-rich (Li-free) compositions is typical for primitive pegmatites. In the late stage, an increase of Na and Mg/Fe results from system opening and reaction of residual fluids with fluids from host rocks.

Petalite- and spodumene-subtype pegmatites: Tourmaline from pegmatites of petalite and spodumene subtypes has been studied on a limited number of localities so far (e.g. Tindle et al. 2002, 2005). Tourmaline fractionation from schorl, through Al-rich schorl to fluor-elbaite and rare darrellhenryite observed in the petalite subtype, predominantly represents evolution of a highly fractionated Ca-poor system with limited interaction with the host rock (Tindle et al. 2002). On the other hand, the trend observed in the spodumene-subtype pegmatites (Teertstra et al. 1999, Tindle et al. 2005) shows a strong Ca,F-enrichment in the tourmaline from fractionated (aplite and lepidolite units), most likely due to Ca,F-complexation in the residual melt.

Lepidolite-subtype pegmatites: In complex-type lepidolite-subtype pegmatites (Selway et al. 1999, Skřápková and Cempírek 2021), complex melt and fluid evolution, as well as crystallization of multiple associated minerals (biotite, muscovite, amblygonite, petalite/spodumene, lepidolite), affect tourmaline composition. In early pegmatite zones, tourmaline crystallization starts with Mg-bearing Al-rich schorl and evolves to foitite to schorl to F-rich schorl. On the other hand, in the central Ab-Lpd zone, primary tourmaline is characterized by evolutional trend Ca-bearing fluor-elbaite → Mn-bearing darrellhenryite-rossmanite (up to 0.65 apfu WO) → fluor-elbaite. Metasomatic tourmaline that partly replaces the primary generations in all pegmatite zones (at crystal rims and along fractures), is rather uniform in composition which depends on the replaced mineral: Li-rich schorl to Fe-rich elbaite → fluor-elbaite →

fluor-elbaite → Fe-bearing fluor-elbaite. The textural-paragenetic evidence shows that all compositions with very high F and Na contents belong to secondary tourmalines, formed by metasomatic or hydrothermal replacement of earlier generations.

Elbaite-subtype pegmatites: Elbaite-subtype pegmatites (Novák & Povondra, 1995) are characterized by tourmaline showing strong enrichment in Mn (and in some cases F), low vacancy and dominant Na in early black tourmaline whereas composition of pink tourmaline in pockets ranges from elbaite to less common liddicoatite. In early zones, tourmaline typically starts as Mg-rich schorl, followed by Al-rich schorl to Li-bearing schorl. The characteristic Tur + Qtz intergrowths that evolve to dark prismatic crystals in pockets usually feature various degree of Mn-enrichment represented by Li,Mn-rich schorl to tsilaisite-celleriite-princivalleite with relatively low Li and F contents. The dark tourmaline at the base of the pegmatite pocket is usually followed by a metasomatic pink/red/violet Li,F-rich tourmaline (fluor-elbaite, elbaite) in pockets. Hydrothermal tourmaline assemblages are characterized by fibrous/acicular crystals or very frequent intergrowths of Li-tourmaline with quartz; an increase of Ca is typical for late stages of tourmaline formation, sometimes reaching the composition of fluor-liddicoatite. Late hydrothermal tourmalines may also form in border pegmatite zones, xenoliths and on exocontacts – primary biotite is replaced by Ti-rich Al-deficient schorl-dravite or Fe^{3+}-rich dutrowite, breakdown of early plagioclase and tourmaline can produce fluor-liddicoatite – liddicoatite – elbaite assemblage. The elbaite-subtype pegmatites are typical by very high B activity during most stages of their evolution, with high F+Li contents restricted to late magmatic (albite zone) and hydrothermal stages.

Conclusions: Novák (2021) concluded the information on tourmaline and its mineral assemblages necessary for direct comparison of analytical data from granitic pegmatites. The available data on tourmaline evolution confirm that the textural information is critical to understanding the information stored in tourmaline zoning, and its geochemical evolution as dissolution-reprecipitation process plays an essential role in evolution of pegmatite systems. Tourmaline geochemical evolution of tourmaline in barren, LCT (lepidolite, petalite, spodumene, elbaite subtypes) and NYF pegmatites is in many aspects similar. Major differences include mainly the initial enrichment in metals (Mg, Fe, Mn), effects of magmatic-hydrothermal transition, and in composition of late-stage hydrothermal tourmaline that results from interaction between fluids and earlier-formed minerals in the pegmatites and its host rocks. Tourmaline composition may serve as an important indicator of Li mobility in the pegmatite system.

Acknowledgement: This work was funded by the EU Horizon Li4Life project (101137932).

References

Gadas P., Novák M., Staněk J., Filip J. & Vašinová Galiová M. (2012) – Compositional evolution of zoned tourmaline crystals from pockets in common pegmatites, the Moldanubian Zone, Czech Republic. *The Canadian Mineralogist,* 50, 895-912.

Jolliff B. L., Papike J. J. & Shearer C. K. (1986) – Tourmaline as a recorder of pegmatite evolution: Bob Ingersol pegmatite, Black Hills, South Dakota. *American. Mineralogist,* 71, 472-500.

Novák M., 2021 – Tourmalines and pegmatites. *Tourmaline 2021, Book of abstracts,* 75-78.

Novák M. & Povondra P. (1995) – Elbaite pegmatites in the Moldanubicum: a new subtype of the rare-element class. *Mineralogy and. Petrolology,* 55, 159-176.

Novák M., Škoda R., Filip J., Macek I. & Vaculovič T. (2011) – Compositional trends in tourmaline from the intragranitic NYF pegmatites of the Třebíč Pluton, Czech Republic; electron microprobe, LA-ICP-MS and Mössbauer study. *The Canadian Mineralogist* 49, 359-380.

Selway J. B., Novák M., Černý P. & Hawthorne F. C. (1999) – Compositional evolution of tourmaline in lepidolite-subtype pegmatites. *European Journal of Mineralogy,* 11, 569-584.

Skřápková, L., & Cempírek, J. (2021) – The role of oxy-tourmalines and metasomatic mixing in evolution of lepidolite-subtype pegmatites. *Tourmaline 2021, Book of abstracts,* 99–100.

Teertstra, D. K., Černý, P., & Ottolini, L. (1999) – Stranger in paradise; liddicoatite from the High Grade Dike pegmatite, southeastern Manitoba, Canada. *European Journal of Mineralogy,* 11 (2), 227-235.

Tindle A. G., Breaks F. W. & Selway J. B., (2002) – Tourmaline in petalite-subtype granitic pegmatites: evidence of fractionation and contamination from the Pakeagama Lake and Separation Lake areas of northwestern Ontario, Canada. *The Canadian Mineralogist,* 40 (3), 753-788.

Tindle, A. G., Selway, J. B., & Breaks, F. W., (2005) – Liddicoatite and associated species from the McCombe spodumene-subtype rare-element granitic pegmatite, northwestern Ontario, Canada. *The Canadian Mineralogist*, 43(2), 769-793.

Crystallization of tourmaline in metaluminous granitic environment: an example from pegmatites of Třebíč Pluton, Czech Republic

Radek Škoda[1]*, Milan Novák[1], Renata Čopjaková[1], Eva Mrkusová[1], Adam Zachař[2]

[1]Department of Geological Sciences, Faculty of Science, Masaryk University, Kotlářská 2, 611 37, Brno, Czech Republic

[2]Czech Geological Survey, Leitnerova 204/22, 602 00 Brno, Czech Republic

*Corresponding author: rskoda@sci.muni.cz

Tourmaline-supergroup minerals crystallizing from peraluminous granitic environments are typically characterized by Al > 6 apfu (Henry & Guidotti, 1985) and commonly fall within the compositional space defined by schorl/dravite, oxy-schorl/oxy-dravite, and foitite/magnesio-foitite or towards Li-members for Li-rich pegmatites. On the other hand, tourmalines from metaaluminous granitic melts are less abundant and their composition usually exhibits Al≤6 apfu (e.g. Novák et al 2011, Bosi et al. 2017).

Tourmalines from intragranitic pegmatites of Třebíč pluton (melagranite to melasyenite) represent a typical example of crystallization from metaluminous environment. These relatively small pegmatites (10-150 cm thick) have an NYF signature and can be divided into: (i) geochemically primitive allanite-type pegmatites, and (ii) more evolved euxenite-type pegmatites. A characteristic feature of these pegmatites is the absence of muscovite or garnet, with actinolite locally present near the contact with the host rock. Typical minor to accessory primary minerals include tourmaline, allanite, ilmenite, titanite, REE-Nb-Ti-Ta oxides, beryl, phenakite, helvite/danalite, pyrite, arsenopyrite, zircon and axinite-group minerals. Their ASI ranges from metaluminous to slightly peraluminous compositions (1.01-1.09) for common to most evolved types, respectively (Čopjaková et al. 2013). Tourmaline crystalizes in several paragenetic types: (1) rare graphic intergrowths with quartz in the most evolved dykes, common (2) irregular coarse-grained aggregates 1-3 cm in size from coarse-grained units, (3) interstitial tourmaline, and (4) rare pseudomorphs after biotite.

In the most evolved slightly peraluminous pegmatites, the chemical composition of graphic tourmaline (1) evolves from schorl cores (~6 apfu Al) to Al-rich schorl (6.4-7.0 apfu Al) rims with increasing X-site vacancy (≤0.3 pfu) and $Fe_{tot}/(Fe_{tot}+Mg)$=0.95-0.98, (Fig 1.).

In the B-rich metaluminous dykes, the crystallization of tourmaline is limited by the availability of Al_2O_3 in the melt. Tourmaline (2) typically formed during the final stage of magmatic crystallization in these dykes, with initial composition in the cores corresponding to dravite: $Fe_{tot}/(Fe_{tot}+Mg)$ of 0.25–0.49, 5.95–6.14 apfu Al, 0.12–0.23 apfu Ca, and X-site vacancies less than 0.10 pfu (Fig 1.). Its crystallization leads to depletion of Al_2O_3 from the melt, and later tourmalines (2, 3) contain less Al (5.04–5.93 apfu), while Ti (0.20–0.55 apfu) and Ca (≤0.43 apfu) contents increase (Fig 1.). This is accompanied by almost no X-site vacancies and higher $Fe_{tot}/(Fe_{tot}+Mg)$ ratios (0.27–0.56). Additionally, these tourmalines exhibit increased Fe^{3+} content (Fe^{3+}/Fe_{tot}=0.14–0.26). Titanium and Ca show a strong negative correlation with Al content. Composition of these Al-depleted tourmalines evolves from Ti- and Fe^{3+}-rich schorl/dravite towards dutrowite/magnesio-dutrowite. The elevated contents of higher-charge cations (Ti^{4+}, Fe^{3+}, and Ca^{2+}), combined with the absence of X-site vacancies, serve to maintain at least 58 positive charges, ensuring electroneutrality of the tourmaline structure in a metaluminous environment. Notably high Fe^{3+} contents in tourmaline occur despite the presence of common minerals indicating low fO_2 (ilmenite, pyrite, and arsenopyrite), and the absence of magnetite. The local occurrence of late stage axinite further indicates a high boron activity in these dykes.

Similarly to tourmaline, beryl-group minerals from these pegmatites also show deviations from ideal stoichiometry. Due to a deficiency of Al in the melt, the octahedral site is partially occupied by Sc,

Mg, and Fe. Moreover, the incorporation of Na and Cs into the structural channels contributes to increasing the overall cationic charge, thereby maintaining electroneutrality. Beryl-group minerals occur in tourmaline-poor pegmatites, whereas tourmaline-rich pegmatites contain helvite to danalite instead.

The compositional features similar to tourmalines of Třebíč pluton pegmatites (low Al, low X-site vacancy, elevated Fe^{3+}, Ti^{4+}, Ca) were observed in tourmalines from other metaluminous to subaluminous environments, for example: Cancrinite Hill, Canada (~5.5 apfu Al, ~0.1 apfu Ti, ~1.3 apfu Fe^{3+}), Kragero, Norway (~4.7 apfu Al, ~0.2 apfu Ti, ~1.1 apfu Fe^{3+}), Mirošov, Czech Republic (~5.6 apfu Al, ~1.3 apfu Fe^{3+}). Hence, the incorporation of significant amounts of monovalent Li (if available) or a pronounced X-site vacancy in the tourmaline structure from low-Al systems is unlikely unless the charge deficit is compensated by the concurrent incorporation of Ti^{4+}, Fe^{3+}, or other suitable higher-valent cations; however, crystal-structural constraints must also be considered.

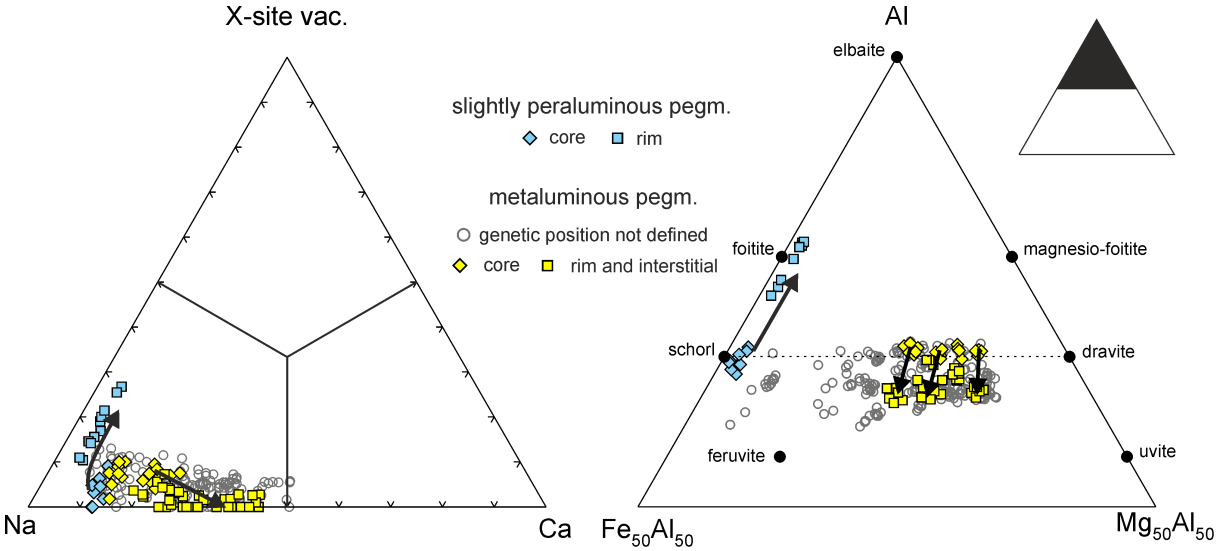

Figure 1. Ternary diagram showing the chemical composition of tourmalines from pegmatites of the Třebíč Pluton. Arrows indicate fractionation trends.

References:

Bosi, F., Skogby, H., Ciriotti, M. E., Gadas, P., Novák, M., Cempírek, J., Všianský, D., & Filip, J. (2017) – Lucchesiite, $CaFe^{2+}{}_3Al_6(Si_6O_{18})(BO_3)_3(OH)_3O$, a new mineral species of the tourmaline supergroup. *Mineralogical Magazine*, 81, 1–14.

Čopjaková, R., Škoda, R., Vašinová Galiová, M., & Novák, M. (2013). Distributions of Y+ REE and Sc in tourmaline and their implications for the melt evolution; examples from NYF pegmatites of the Třebíč Pluton, Moldanubian Zone, Czech Republic. *Journal of Geosciences*, 58, 113–131.

Henry, D. J., & Guidotti, C. V. (1985) – Tourmaline as a petrogenetic indicator mineral: an example from the staurolite-grade metapelites of NW Maine. *American mineralogist*, 70, 1–15.

Novák, M., Škoda, R., Filip, J., Macek, I., & Vaculovič, T. (2011) – Compositional trends in tourmaline from intragranitic NYF pegmatites of the Třebíč Pluton, Czech Republic: an electron microprobe, Mössbauer and LA–ICP–MS study. *The Canadian Mineralogist*, 49, 359–380.

Filip, J., Bosi, F., Novák, M., Skogby, H., Tuček, J., Čuda, J., Wildner, M. (2012) – Redox processes of iron in the tourmaline structure: example of the high-temperature treatment of Fe^{3+}-rich schorl. *Geochimical Cosmochimical Acta*, 86, 239-256.

New evidence that Li-bearing pegmatitic tourmaline from Elba Island, Italy, crystallized in two events

Federico Pezzotta[1,*], Andreas Ertl[2,3], Hans-Peter Meyer[4], Thomas Ludwig[4]

[1] MUM – Mineralogical Museum "Luigi Celleri", San Piero in Campo, Livorno, Italy
[2] Naturhistorisches Museum, Wien, Austria
[3] Institut für Mineralogie und Kristallographie, Universität Wien, Wien, Austria
[4] Institut für Geowissenschaften, Ruprecht-Karls-Universität Heidelberg, Heidelberg, Germany
* Corresponding author: *fpezzotta@yahoo.com*

The Rosina aplite-pegmatite dyke (up to 2 m wide) near San Piero in Campo, Elba, has a complex asymmetric zoning. It contains small to large pockets rich in accessory minerals (Pezzotta, 1994; Pezzotta et al., 1996; Pezzotta and Orlandi, 1998; Pezzotta and Guastoni, 2007). This locality is also known for beautiful large-zoned tourmaline crystals.

Multicolored tourmalines from the Elba Island often have darker colored terminations due to the incorporation of Fe and/or Mn. A tourmaline crystal found naturally broken in two fragments within a wide miarolitic cavity in the Rosina pegmatite (San Piero in Campo, Elba Island, Italy), and characterised by late-stage dark-coloured overgrowths was investigated by Altieri et al. (2023b). Microstructural and paragenetic observations, together with compositional and spectroscopic data (electron microprobe and optical absorption spectroscopy), provide evidence that the formation of the dark-colored and Mn-rich overgrowths could be the result of pocket rupture. Altieri et al. (2023b) argue that the two fragments were originally a single crystal which underwent natural breakage followed by the simultaneous growth of Mn-rich dark terminations at both breakage surfaces. A further investigation by Altieri et al. (2023a), on the basis of chemical and spectroscopic investigations, combined with structural and paragenetic observations of the cavities, propose a general genetic model in which, as a consequence of a pocket rupture event, chemical alteration of Fe- and Mn-rich minerals that formed early in the pegmatitic rock surrounding the cavities occurred through leaching processes, produced by the action of the highly reactive late-stage cavity fluids. Such processes could be responsible for the release of Fe and Mn in the geochemical system, allowing the formation of the latestage dark-colored terminations in the tourmaline crystals (Altieri et al., 2023a).

In this study a group of tourmaline samples collected 2008 in the Rosina Pegmatite by the first two authors (F.P. and A.E.), was examined. In particular, two zoned tourmaline crystals from two different pockets were characterized chemically, including the light elements. The crystallization of these crystals begins with Fe-rich and Mn-containing tourmaline in the pegmatite rock surrounding the cavities. Both samples examined have a total amount of ca. 13-15 wt.% FeO in this first zone. Then Fe decreases within the pocket while MnO increases up to ca. 8 wt%. Later, Mn decreases while Li increases (up to 1.7 wt% Li_2O). At the slightly darker termination of both crystals FeO is increasing, like what have been reported by Altieri et al. (2023a and 2023b).

A high correlation ($r^2 = 0.999$) between fluorine content and *X*-site charge (the *X* site can be occupied by Na, Ca, K or can be vacant) was found in the study of the crystal growth of a zoned tourmaline from a Li-pegmatite from the Himalaya Mine, San Diego co., California, USA (Ertl et al., 2010). In that study, it is also reported the case of a second crystal which is a Ca-rich and Mg-bearing tourmaline from a different pocket grown during the latest stages of crystallization of the cavity, which composition lies outside of such a correlation. As an explanation, Ertl et al. (2010) suggest an influence of the host rock on the growth of this late-stage crystal, which influenced the composition of the late-stage fluids and thus created a growth environment that differed from that of the first crystal formed in highly developed pegmatitic fractionated fluids.

Concerning the Rosina pegmatite crystals, when the fluorine content is plotted against the *X*-site charge for the first tourmaline examined, it can be seen that all zones, with the exception of the termination, show a positive correlation with $r^2 = 0.996$ (3 zones). Indeed, the termination lies slightly outside of this linear function. When the fluorine content is plotted against the *X*-site charge of the second tourmaline crystal examined, it can also be seen that all zones, with the exception of the termination, show a high positive correlation ($r^2 = 0.999$, 4 zones). Once again, in this crystal the

termination is clearly outside this function. These observations are here interpreted as an evidence that the terminations of the tourmaline crystals in the Rosina pegmatite grew during a different event than the previously grown crystals.

Hence, we agree with Altieri et al. (2023a) that the formation of the terminations of the tourmaline crystals from the Rosina pegmatite can be related to a dramatic physicochemical change in the crystallization environment as a consequence of an opening of the geochemical system. Moreover, the model reported in Altieri et al. (2023b) that the formation of the dark-colored Mn-rich overgrowths could be the result of a pocket rupture seems reasonable.

This research was funded in part (AE) by the Austrian Science Fund (FWF) project P 35585.

References

Altieri, A., Pezzotta, F., Andreozzi, G.B., Skogby, H. and Bosi, F. (2023a) - Genetic model for the color anomalies at the termination of pegmatitic gem tourmaline crystals from the island of Elba, Italy. *European Journal of Mineralogy*, 35, 755–771.

Altieri, A., Pezzotta, F., Skogby, H., Hålenius, U. and Bosi, F. (2023b) - Dark-coloured Mn-rich overgrowths in an elbaitic tourmaline crystal from the Rosina pegmatite, San Piero in Campo, Elba Island, Italy: witness of late-stage opening of the geochemical system. *Mineralogical Magazine*, 87, 130–142.

Ertl, A., Rossman, G.R., Hughes, J.M., London, D., Wang, Y., O'Leary, J.A., Dyar, M.D., Prowatke, S., Ludwig, T., Tillmanns, E. (2010) - Tourmaline of the elbaite-schorl series from the Himalaya Mine, Mesa Grande, California: A detailed investigation. *American Mineralogist*, 95, 24–40.

Pezzotta, F. (1994) - Helvite of a M.te Capanne pluton pegmatite (Elba island, Italy): chemical, X-ray diffraction data and description of the occurrence. *Atti dell'Accademia nazionale dei Lincei. Rendiconti*, 9, 355–362.

Pezzotta, F. and Guastoni, A. (2007) - Hambergite, helvite e pirofanite nelle pegmatiti elbane. *Rivista Mineralogica Italiana*, 3/2007, 166–168.

Pezzotta, F. and Orlandi, P. (1998) - Découvertes minéralogiques récentes dans les pegmatites de l'île d'Elbe. *Le Règne Minéral*, 4 (20) Les Éditions du Piat. 31–38.

Pezzotta, F., Hawthorne, F.C., Cooper, M.A. and Teertstra, D.K. (1996) - Fibrous foitite from San Piero in Campo, Elba, Italy. *Canadian Mineralogist*, 34, 741–744.

Natural Corrrosion Phenomena on and within Tourmaline Crystals from the Roof of the World: Records of Temporary Undersaturation

Paul Rustemeyer

Rustemeyer-gundelfingen@t-online.de

Tons of dark tourmalines from pegmatites in Pakistan and Afghanistan have been brought to the mineral market as by-products of the rare gem minerals. The author has searched this material since 40 years and thus found a great diversity of outer and inner corrosion phenomena, some of which will be presented in this contribution.

At the end of tourmaline growth there is often a period in which the fluid around the crystal becomes undersaturated. It then redissolves or etches the tourmaline, preferably at places with crystal defects or more easily dissoluble material. The geometry of these etching phenomena depends largely on the type of crystal face.

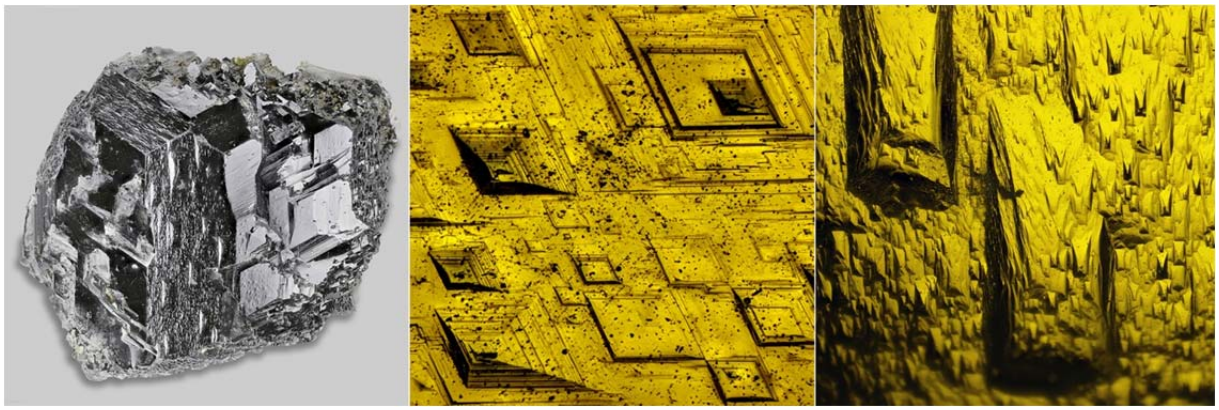

Figure 1. Examples of a 3cm wide etched Schorl crystal from Kunar valley, Afghanistan, with micrographs (1 mm wide) of etching pits and hillocks

Figure 2. Left: overview of etching pits and hillocks on different tourmaline faces, middle: corroded schorl from Skardu (3,5 cm wide), right: deeply eroded schorl, from Skardu with portions of rim layer intact, 3 cm wide

Very different architectures of stronger corroded tourmaline crystals have been discovered.

From several hundred tourmaline crystals from Pakistan and Afghanistan stacks of tourmaline thin sections perpendicular to the c-axis were prepared. Some of these show quite complex corrosion patterns, which will be illustrated by examples from 15 different crystals.

With the “stripe method” (Figure 3), the internal structure of crystals can be transferred from the cross-cuts to a profile parallel to the c-axis. From this profile a simplified growth history of the tourmaline crystal can be designed.
Corrosion took place in early, medium and late stages of tourmaline growth, some crystals whiteness two or more corrosion events.

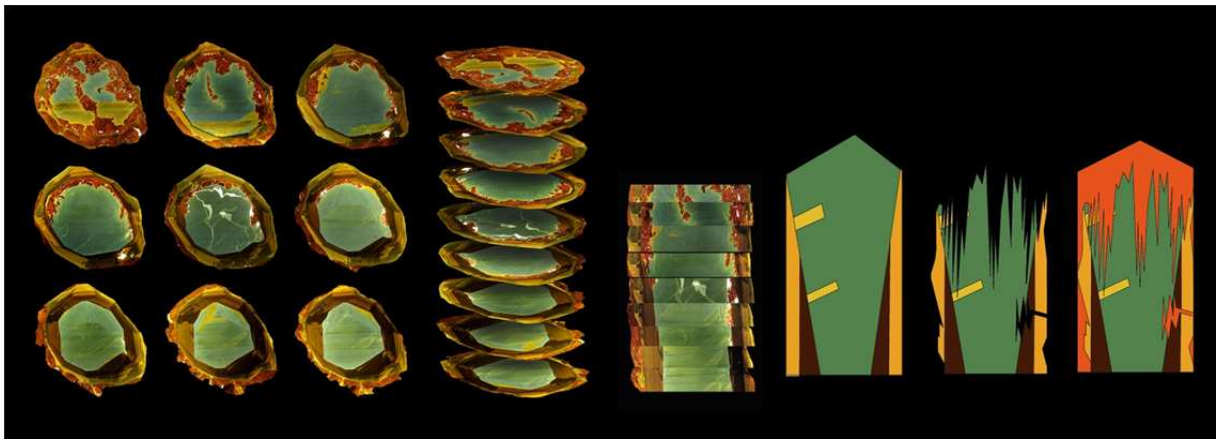

Figure 3. From thin sections to the growth history: Left: 9 slices of schorl from Skardu, Pakistan, 2,5 cm wide. Middle: perspective view of the stack of slices and the stack of stripes from across the middle of each slice. Right: the latter is transferred into a simplified growth history of the crystal

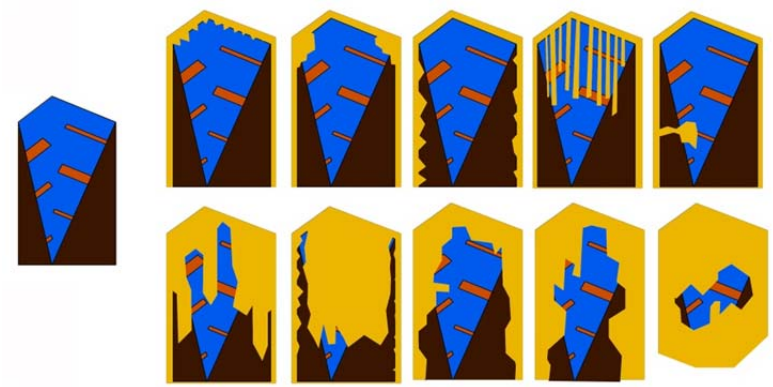

Figure 4. Examples of etched tourmaline morphologies (blue and brown), which have been overgrown (healed) with ocher tourmaline

Using this method of stacked slices a diversity of corrosion events could be discovered in outwardly inconspicuous crystals. 15 examples of such crystals will be presented, illustrating the diversity and different intensity of corroded and healed tourmaline. This inner architecture of crystals is a good recorder of the interrupted growth and dissolution history of tourmaline, giving valuable information on the timing and intensity of saturated and undersaturated fluid in the crystallizing pegmatite.

References

Heimann R.B.(1975) Auflösung von Kristallen, Springer 268 p
Rustemeyer, P. (2003): Faszination Turmalin, Spektrum Akad. Verl. 2003, 308 p.
Rustemeyer, P. (2015): Tourmaline – Fascinating Crystals with Fantastic Inner Worlds, 272 p.
Rustemeyer, P. (2022) The Inner Architecture of Tourmaline Crystals as inferred from the morphology of color zones in thin slices, J. Geoscience 67, 103-128

Miocene LCT and tourmaline-bearing pegmatites of Amter (Chefchaouen, Morocco): structural, textural and mineralogical insights

Matteo Giannoni[(1)], Andrea Dini[(2)], Mirko Bonechi[(3)], Federico Pezzotta[(4)]

[1] MCP srl, Milano, Italy; matteo.giannoni12@gmail.com
[2] Istituto di Geoscienze e Georisorse C.N.R., Pisa, Italy
[3] 3B Minerals, Via della Comunità Europea 22/24, Figline e Incisa Val D'Arno (FI), Italy
[4] MCP srl, Milano, Italy

The Beni Bousera massif, part of the Internal Rif domain in northern Morocco, consists of an exhumed peridotitic body derived from subcontinental lithospheric mantle and structured in a domiform geometry. In its southern portion, a rare set of Miocene LCT pegmatites intruded the serpentinized peridotites, providing a unique case of interaction between peraluminous melts and ultramafic rocks in the Appennino-Maghrebian chain.

These pegmatites emerged on the mineral market in 2017, mislabeled as from "Ouarzazate". Only in 2022 was the true locality identified near Amter. Two field campaigns between 2022 and 2023, coordinated by IGG-CNR, documented 270 pegmatitic veins and 112 microgranitoid bodies over a 30 km² area. Pegmatitic veins range from a few centimeters up to ~10 m in length and 1.5 m in thickness, displaying mainly prismatic morphologies.

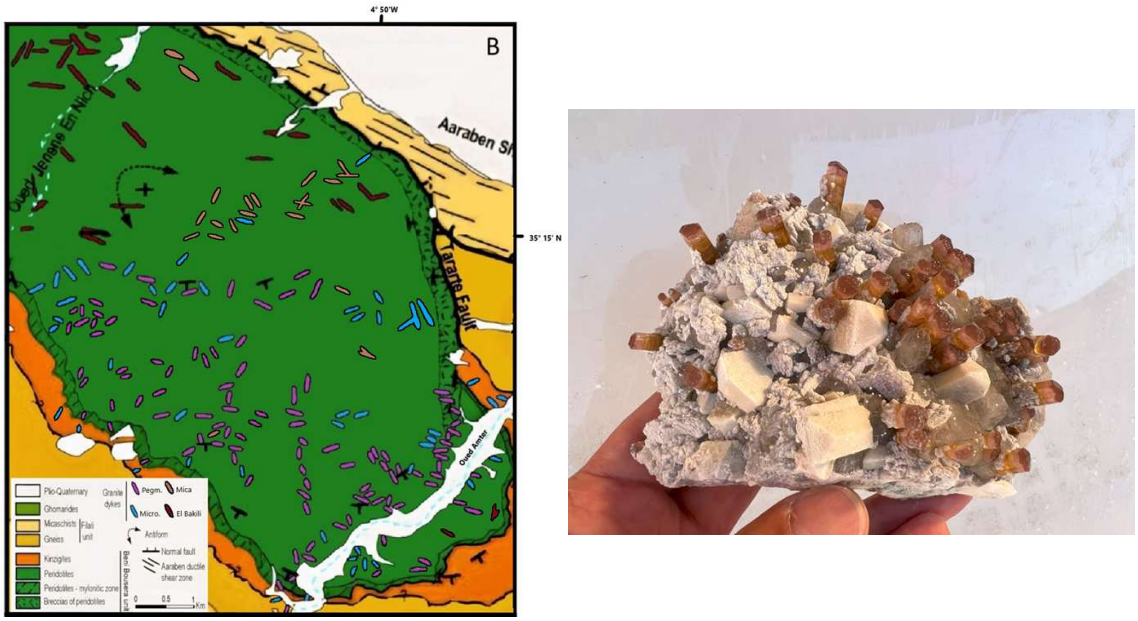

Figure 1 and 2 – 1) Geological map of the Amter pegmatite field (Mod. El Bakili et al., 2020). 2) Elbaite sample from Amter pegmatites.

Internally, the Amter pegmatites exhibit five distinct petrographic zones, each associated with characteristic tourmaline morphologies and compositions:

Dark mica-rich border zone: Dominated by blades of dark mica (biotite-siderophyllite), often altered to vermiculite. Tourmaline is scarce and Fe-rich, it occurs as a secondary generation.

Aplitic shell: Fine-grained albite and quartz with subordinate tourmaline classified as schorl (FeO: 13.1 wt%, MnO: 0.4 wt%, MgO: 1.0 wt%)

Cordierite-bearing graphic zone: Dominated by graphic intergrowths of quartz and feldspar with skeletal cordierite, often altered to muscovite and chlorite. Tourmaline appears as subhedral black crystals with a schorlitic composition (FeO: 12.5 wt%, MnO: 0.7 wt%, MgO: 1.4 wt%)

Tourmaline-rich zone: Marked by randomly oriented tourmaline and intergrowth with quartz. The chemical analyses show a foititic composition (FeO: 11.4 wt%, MnO: 1.5 wt%, MgO: 1.7 wt%)

Axial miarolitic zone: Hosts large, fan-shaped, isooriented tourmaline aggregates with c-axes perpendicular to the axial plane. Here, tourmaline shows a compositional evolution: FeO decreases from ~13 wt% to 7 wt% toward miarolitic cavities, while MnO increases from 0 to 4 wt%

This chemical evolution of tourmaline mirrors the fractionation and fluid evolution within the LCT pegmatitic system.

Contact zones between pegmatite and host peridotite show metasomatic rims composed of lizardite and smectite. Mineral reactions indicate serpentinization of enstatite and forsterite in the presence of silica- and H_2O-rich fluids derived from pegmatitic melts. Reaction rims are absent at microgranite contacts, suggesting distinct fluid regimes during crystallization.

The pegmatites' spatial arrangement and geometry are consistent with emplacement along inherited foliations and faults. Their dispersion as small, disconnected intrusions rather than continuous tabular bodies is interpreted as the result of emplacement during syn-tectonic deformation of the peridotitic host. All mapped pegmatites exhibit systematic textural-mineralogical zoning, supporting a closed-system crystallization model.

Geochemical and isotopic data (Rossetti et al., 2010, 2013) from pegmatitic and microgranitic bodies in the southern Beni Bousera massif ($^{87}Sr/^{86}Sr$ = 0.719–0.722; $\varepsilon Nd(t)$ = –10 to –11.5) indicate a crustal origin for the pegmatitic melts, consistent with partial melting of peraluminous metasedimentary protoliths. The melts are strongly peraluminous (A/CNK > 1), silica-rich (SiO_2 > 69 wt%), and poor in ferromagnesian components, pointing to anatexis involving dehydration of muscovite–biotite-bearing assemblages. Trace element data and the low CaO content (< 2 wt%) suggest a plagioclase-rich source, more likely a metagreywacke than a metapelite.

Field and structural evidence could suggest the existence of a granitic pluton emplaced at depth below the southern dome-shaped portion of the massif. This hidden plutonic root is proposed as both the magmatic source and the tectonic engine behind the emplacement of the pegmatite and microgranite dykes. The structural doming of the southern Beni Bousera, previously attributed solely to Alpine exhumation, may thus reflect magmatic inflation at depth. This hypothesis presents strong analogies with what is observed in the Tuscan Magmatic Province (Westerman et al., 2004), where the emplacement of granitic plutons triggered intense ductile-to-brittle deformation in the aureole.

References

El Bakili, A., Corsini, M., Chalouan, A., Munch, P., Romagny, A. (2020) - Neogene polyphase deformation related to the Alboran Basin evolution: new insights for the Beni Bousera massif (Internal Rif, Morocco). *Bulletin de la Société Géologique de France*, 191 (1), 10.

Rossetti, F., Theye, T., Lucci, F., Bouybaouene, M.L., Dini, A., Gerdes, A., Phillips, D., Cozzupoli D. (2010) - Timing and modes of granites magmatism in the core of the Alboran Domain, Rif Chain, northern Morocco: implications for the Alpine evolution F. Rossetti et al. / Gondwana Research 83 (2020) 157–182 181 of the Western Mediterranean. Tectonics 29, TC2017.

Rossetti, F., Dini, A., Lucci, F., Bouybaouenne, M., Faccenna, C. (2013) - Early Miocene strike-slip tectonics and granite emplacement in the Alboran Domain (Rif Chain, Morocco): significance for the geodynamic evolution of Western Mediterranean, Tectonophysics, Volume 608, 774-791, ISSN 0040-1951.

Westerman, D.S., Dini, A., Innocenti, F., Rocchi, S. (2004) - Rise and fall of a nested Christmas-tree laccolith complex, Elba Island, Italy. N. Petford & c. Breitkreutz (Ed.), Physical geology of high-level magmatic system. Geological Society London Special Publication, 234; 195-213.

Tourmaline nomenclature: An update and challenges

Henry, D.J.*[1]

[1]Department of Geology and Geophysics, Louisiana State University, Baton Rouge, LA, 70803 USA
* Corresponding author: *glhenr@lsu.edu*

The current systematic nomenclature for the tourmaline supergroup minerals began shortly after the First Tourmaline Conference in 1997 and has significantly advanced since then. Over the years, improvements in analytical techniques and the development of new methodologies have enabled more comprehensive determinations of the crystallography and chemical variability of tourmaline. According to data from GEOREF, over 8,100 papers have been published addressing various aspects of tourmaline, highlighting the growing interest and expanding knowledge in this mineral supergroup.

Two key concepts have significantly influenced the classification and understanding of tourmaline (e.g., Henry and Dutrow, 2018). The first is the recognition of two distinct OH-bearing anion sites: the *V* and *W* sites. In this framework, F^- exclusively occupies the *W* site, while O^{2-} shows a preference for the same site. This insight led to a revision of the general chemical formula of tourmaline to $X\,Y_3\,Z_6\,T_6\,(BO_3)_3\,O_{18}\,(V)_3\,(W)$, where the most common substituents are X = Na, Ca, K or (X-site vacancy); Y = Al, Li, Fe^{2+}, Mg, Mn^{2+}, Fe^{3+}, V^{3+}, Cr^{3+}, Ti^{4+}; Z = Al, Mg, Cr^{3+}, V^{3+}, Fe^{2+} and Fe^{3+}; T = Si, Al, B; V = OH^{1-}, O^{2-} and W = F^{1-}, O^{2}, OH^{1-} (Hawthorne and Henry 1999). In the *R3m* tourmaline structure, X**,** Y**,** Z**,** T**,** and B denote specific cation groups occupying the corresponding crystallographic sites (italicized), while the V-group anions are located at the *O(3)* site and the W-group anions at the *O(1)* site. These systematic relations prompted the IMA Subcommittee on Tourmaline Nomenclature to designate tourmaline as a supergroup mineral, divided into three primary groups based on the dominant cation or vacancy in the X site: the alkali, calcic, and X-site vacancy groups (Henry et al., 2011). The second key concept involves order-disorder phenomena among cations across multiple cationic sites, particularly in tourmalines where O^{2-} is dominant anion in the *W* site. A critical rule guiding species definition within this system is the dominant-valency rule, which states that for any relevant site, the dominant ion of the dominant valence state is used for nomenclature (Hatert and Burke, 2008). This principle is now standard practice in species establishment by the IMA-CNMNC (Bosi et al., 2019). Reflecting these conceptual advances and nomenclature refinements, the number of recognized tourmaline species has grown markedly—from 13 species in 1997 to 38 species by the Third Tourmaline Conference in 2021, and 42 species as of 2025 (see Table 1).

TABLE 1. Changes and additions to IMA-recognized tourmaline species since the TUR2021 Conference

year	Species	Formula	IMA proposal
2022	Lunaite discredited	Triclinic dimorphs of schorl and oxy-dravite e.g., schorl-1A	Proposal 21-L
2022	Ferro-bosiite	(Na) ($Fe^{3+}{}_3$Al) ($Al_4Fe^{2+}{}_2$) (Si_6O_{18}) (BO_3)$_3$ (OH)$_3$ (O)	IMA No. 2022-069
2023	Magnesio-dutrowite	(Na) ($Mg_{2.5}Ti_{0.5}$) (Al_6) (Si_6O_{18}) (BO_3)$_3$ (OH)$_3$ (O)	IMA No. 2023-015
2024	Ertlite	(Na) (Al_3) (Al_6) ($Si_4B_2O_{18}$) (BO_3)$_3$ (OH)$_3$ (O)	IMA No. 2023-086
2024	Fluor-rossmanite	(Na) (Al_2Li) (Al_6) (Si_6O_{18}) (BO_3)$_3$ (OH)$_3$ (F)	IMA No. 2023-111

Recent experimental studies involving uncommon cations, along with new analytical data from natural tourmaline samples, suggest that additional tourmaline species are likely to be identified in the future. A notable example of this expanding diversity is the discovery of tourmaline with K as the dominant cation at the *X* site within the alkali group—an occurrence that was previously considered rare. Berryman et al. (2015) successfully synthesized "potassium-dravite" at 4 GPa, and shortly thereafter, the K-dominant magnesian oxy-tourmaline species, maruyamaite, was identified in the UHP terrain of Kokchetav, Kazakhstan. In a similar vein, a Pb-analog of "oxy-uvite" was synthesized by Vereshchagin et al. (2020), and small amounts of natural Pb-dominant tourmaline have since been reported from several pegmatite deposits by Kubernátová and Cempírek (2021). Furthermore, ongoing experimental studies suggest that there are no crystallographic constraints preventing the formation of Ni-, Co-, or Cu-dominant tourmaline species in natural systems, paving the way for future discoveries (e.g. Vereshchagin et al., 2020).

An additional challenge is determining the most effective way to use diagrams to classify tourmaline species vs. characterization of the solid solutions that occur within them. These diagrams are essential for helping the broader public distinguish between species designations and the underlying crystal-chemical variations. For instance, when identifying oxy-tourmalines, the Al-Cr-Fe^{3+} ternary diagram is useful for determining species (Fig. 1a). In contrast, a diagram plotting Al(total) against X-site vacancy is more helpful for identifying chemical substitutions that may occur within the tourmaline solid solution (Fig. 1b).

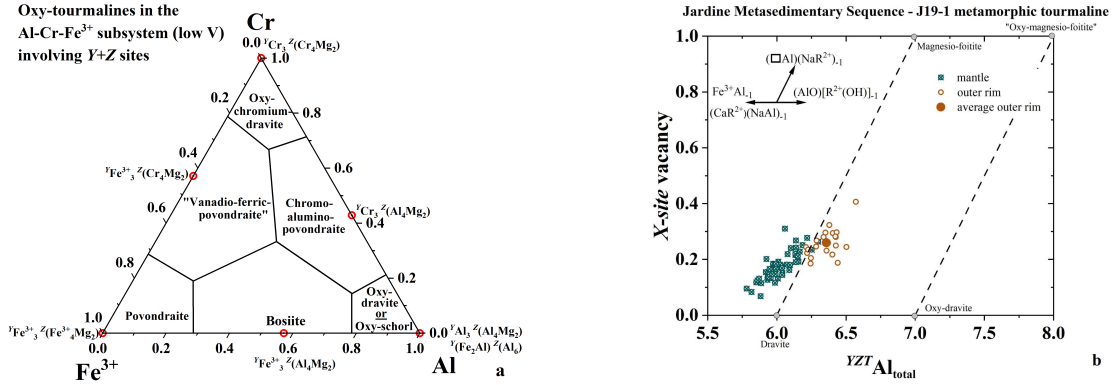

.FIGURE 1. Species vs. substitution diagram. (1a) Graphical limits of oxy-tourmaline species in the Al-Cr-Fe^{3+} subsystem considering Al-Cr-Fe^{3+} over the sum of the Y and Z sites i.e., unnecessary to determine ordering to define species (Henry and Dutrow 2018, Bosi et al. 2020). (1b) Data array in the Al vs. X-site vacancy diagram. The general orientation of the data arrays relates to the likely substitutions in different parts of the tourmaline grains. The locations of the end-member species are a projection onto the simplified composition space and the position in the diagram should not be used for species classification.

References

Bosi, F. (2018) Tourmaline crystal chemistry. American Mineralogist, 103, 298-306.

Bosi, F., Hatert, F., Hålenius, U., Pasero, M., Miyawaki, R., and Mills, S.J. (2019) On the application of the IMA−CNMNC dominant-valency rule to complex mineral compositions. Mineralogical Magazine, 83, 627-632.

Bosi, F., Altieri, A., Cámara, F., and Ciriotti, M.E. (2020) Chromium-rich vanadio-oxy-dravite from the Tzarevskoye uranium–vanadium deposit, Karelia, Russia: a second world-occurrence of Al–Cr–V–oxy-tourmaline. Mineralogical Magazine, 84, 797-804.

Hatert, F., and Burke, E.A.J. (2008) The IMA-CNMNC dominant-constituent rule revisited and extended. Canadian Mineralogist, 46, 717-728.

Hawthorne, F. C., and Henry, D. J. (1999) Classification of the minerals of the tourmaline group. European Journal of Mineralogy, 11, 201-215.

Henry, D. J., and Dutrow, B. L. (2018) Tourmaline studies through time: contributions to scientific advancements. Journal of Geosciences, 63, 77-98.

Henry, D.J., Novák, M., Hawthorne, F.C., Ertl, A., Dutrow, B.L., Uher, P., and Pezzotta, F. (2011) Nomenclature of the tourmaline-supergroup minerals. American Mineralogist, 96, 895-913.

Kubernátová, M. and Cempírek, J. (2021) Crystal chemistry of natural Pb-rich tourmalines. Natura, 111, 58-60.

Lussier, A., Ball, N. A., Hawthorne, F. C., Henry, D. J., Shimizu, R., Ogasawara, Y., and Ota, T. (2016) Maruyamaite, $K(MgAl_2)(Al_5Mg)Si_6O_{18}(BO_3)_3(OH)_3O$, a potassium-dominant tourmaline from the ultrahigh-pressure Kokchetav massif, northern Kazakhstan: Description and crystal structure. American Mineralogist, 100, 355-361.

Vereshchagin, O.S., Frank-Kamenetskaya, O.V., Rozhdestvenskaya, I.V., and Zolotarev, A.A. (2018) Incorporation of 3d elements in tourmalines: structural adjustments and stability. European Journal of Mineralogy, 30, 917-928.

Vereshchagin, O.S., Wunder, B., Britvin, S.N., Frank-Kamenetskaya, O.V., Wilke, F.D.H., Vlasenko, N.S., and Shilovskikh, V.V. (2020) Synthesis and crystal structure of Pb-dominant tourmaline. American Mineralogist, 105, 1589-1592.

Metamorphic and detrital tourmaline in the Archean meta-turbidites of the Beartooth Mountains, MT-WY, USA

Henry, D.J.*[1], David W. Mogk[2], Matthew P. Loocke[1] and Barbara L. Dutrow[1]

[1]Department of Geology and Geophysics, Louisiana State University, Baton Rouge, LA, 70803 USA; [2]Department of Earth Sciences, Montana State University, Bozeman, Montana 59717, USA
* Corresponding author: *glhenr@lsu.edu*

The Archean Jardine Metasedimentary Sequence (JMS) of the western Beartooth Mountains, northern Wyoming Province, Montana-Wyoming, USA, contains tourmaline-bearing lithologies in which metamorphic overgrowths nucleate on detrital tourmaline cores (Mogk et al. 2020). Tourmaline overgrowths preserve information about the prograde metamorphic history. Detrital tourmaline core compositions constrain the lithologic character of the upper continental crust prior to the deposition of the JMS. The JMS preserves sedimentary structures typical of turbidite sequences consistent with mid-to-distal submarine fan deposits on an active continental margin. The JMS turbidites were deposited after 2.9 Ga (youngest detrital zircon in the JMS) and before intrusion of cross-cutting granitic plutons at 2.8 Ga. U-Pb ages of JMS detrital zircons (2.9-3.6 Ga) suggest an ancient provenance for the protoliths. Medium-grade, low-pressure metamorphism (~550-600°C, 3-4 kbar) of JMS metapelitic rocks is characterized by a diagnostic assemblages of staurolite-andalusite-biotite ± garnet ± chlorite ± fibrolitic sillimanite associated with metamorphism at 2.8-2.9 Ga.

Synchronous metamorphic tourmaline overgrowths exhibit compositional asymmetry closest to the detrital core along the +c and -c poles with two metamorphic mantle zones (Zones 1 and 2). These zones are surrounded by an outer rim zone (Zone 3) (Figure 1). Representative compositions for each zone is given in Table 1. These compositional differences are temperature dependent and, based on tourmaline thermometry, Zone-1 tourmaline initially crystallized at ~350°C (next to detrital cores) and Zone 2 tourmaline crystallized at ~500°C (e.g. Sperlich et al. 1996, van Hinsberg and Schumacher 2007). The outer rim formed at peak metamorphic conditions of ~550-600°C.

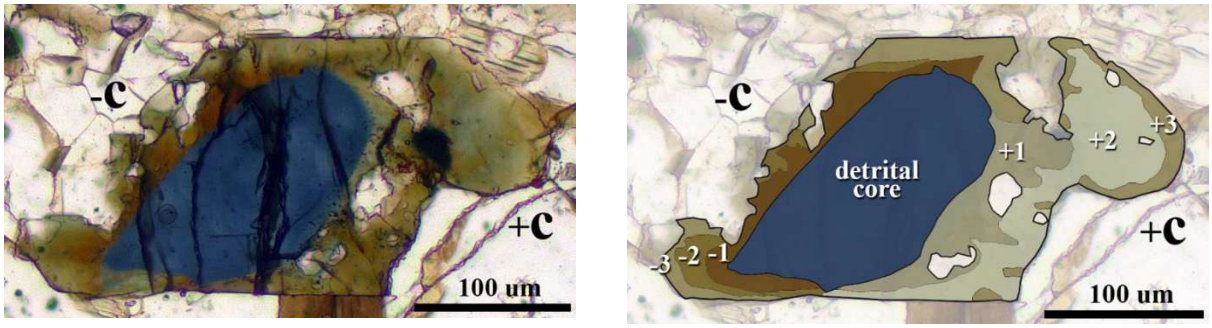

FIGURE 1. (left) Tourmaline with a detrital core and three metamorphic zones in plane polarized light. (right) Tourmaline with an interpretive overlay showing the core and three metamorphic zones.

TABLE 1. Representative tourmaline compositions for Zones 1, 2 and 3 (sample 8558)

Zone	
Zone 1 (-c)	$(Na_{0.78}\square_{0.19}Ca_{0.03})(Fe_{1.55}Mg_{01.05}Ti_{0.39})(Al_{5.58}Mg_{0.40}Cr_{0.01})Si_{6.01}(BO_3)_3O_3([OH]_{0.75}O_{0.24}F_{0.01})$
Zone 1 (+c)	$(Na_{0.70}\square_{0.28}Ca_{0.01})(Mg_{1.44}Fe_{1.26}Al_{0.24}Ti_{0.04}Cr_{0.03})(Al_{6.00})Si_{5.98}Al_{0.02}(BO_3)_3O_3([OH]_{0.94}O_{0.04}F_{0.02})$
Zone 2 (-c)	$(Na_{0.71}\square_{0.17}Ca_{0.11})(Mg_{1.72}Fe_{1.13}Ti_{0.15})(Al_{5.89}Mg_{0.07}Cr_{0.04})Si_{5.86}Al_{0.14}(BO_3)_3O_3([OH]_{0.97}O_{0.03})$
Zone 2 (+c)	$(Na_{0.69}\square_{0.26}Ca_{0.05})(Mg_{1.62}Fe_{1.11}Al_{0.17}Ti_{0.07}Cr_{0.03})(Al_{6.00})Si_{5.99}Al_{0.01}(BO_3)_3O_3([OH]_{0.83}O_{0.13}F_{0.04})$
Zone 3 rim	$(Na_{0.62}\square_{0.27}Ca_{0.11})(Mg_{1.63}Fe_{0.94}Al_{0.31}Ti_{0.09})(Al_{6.00})Si_{5.93}Al_{0.07}(BO_3)_3O_3([OH]_{0.70}O_{0.27}F_{0.02})$

Detrital tourmaline core compositions constrain potential protoliths of clastic material. Application of tourmaline provenance discriminant diagrams suggests lithologic sources of detrital cores include

peraluminous granitic rocks, weakly fractionated and oxidized granitic rocks, aluminous metapelites, Al-poor and Fe^{3+}-rich metapsammites, magnesian metasediments, and calc-silicate rocks. Thus, the crust formed and exposed at the surface during the 2.9-3.6 Ga interval contained a wide range of relatively evolved lithologies than are generally assumed for Mesoarchean and older crust.

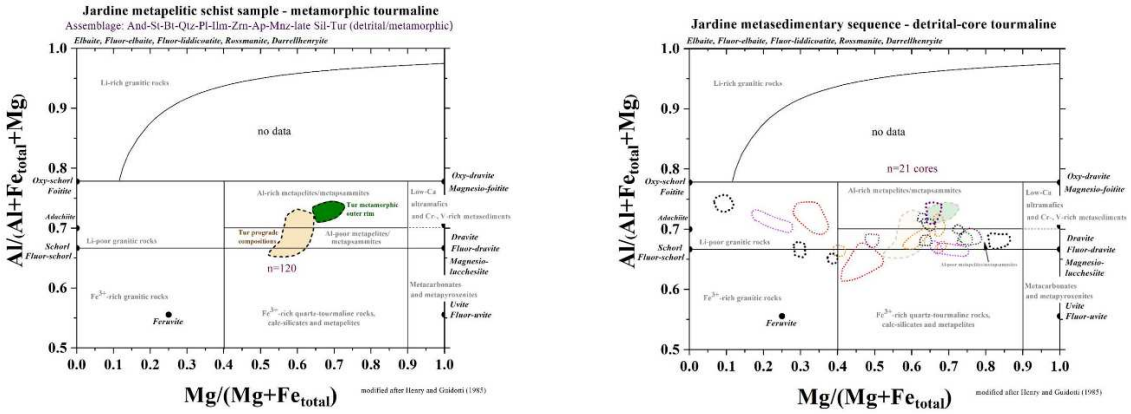

.FIGURE 2. Tourmaline provenance diagram for metamorphic tourmaline and detrital cores (Henry and Guidotti 1985, Henry and Dutrow 2018). (left) Compositional ranges for metamorphic tourmaline in zones 1 and 2 (combined) and zone 3 (outer rim). (right) Compositional ranges for individual detrital cores.

References

Henry, D.J. and Dutrow, B.L. (2018) Tourmaline studies through time: Contributions to scientific advancements. Journal of Geosciences, 63, 77-98. https://doi.org/10.3190/jgeosci.255.

Henry, D.J. and Guidotti, C.V. (1985) Tourmaline as a petrologic indicator mineral - an example from the staurolite-grade metapelites of NW Maine. American Mineralogist, 70, 1-15.

Mogk, D.W., Mueller, P.A. and Henry, D.J. (2020) The Archean geology of Montana. Montana Bureau of Mines and Geology Centennial Volume. Available online: https://mbmg.mtech.edu/pubs/GeologyOfMontana/ (accessed August 1, 2024).

Sperlich, R., Giere, R. and Frey, M. (1996) Evolution of compositional polarity and zoning in tourmaline during prograde metamorphism of sedimentary rocks in the Swiss Central Alps. American Mineralogist, 81, 1222-1236.

van Hinsberg, V.J. and Schumacher, J.C. (2007) Intersector element partitioning in tourmaline: a potentially powerful single crystal thermometer. Contributions to Mineralogy and Petrology, 153, 289-301.

The History of Zoned Tourmaline Crystals from Anjanabonoina and the Emergence of Public Exhibitions of Tourmaline Slice Collections

Paul Rustemeyer

Rustemeyer-gundelfingen@t-online.de

After the first mention (Lacroix 1908) of the inner beauty of zoned tourmaline slices from Anjanabonoina ~~cut across the c-axes~~, several natural history museums acquired tourmaline slices for their highly decorative qualities. After the two world wars, the pegmatite of Anjanabonoina was rediscovered by Julius Petsch. In 1972 he started delivering numerous large zoned tourmaline crystals but the gem-industry had no interest in strongly zoned material (Petsch 2015).
The Becker company in Idar-Oberstein then started to offer sliced crystals to natural history museums worldwide and later to the mineral collectors market. Around 1975 a tourmaline slice was offered to Friedrich Benesch, who was a priest, natural scientist, and anthroposophist, especially interested in minerals. He was amazed with the zoning in the tourmaline slices. With a group of amateurs he

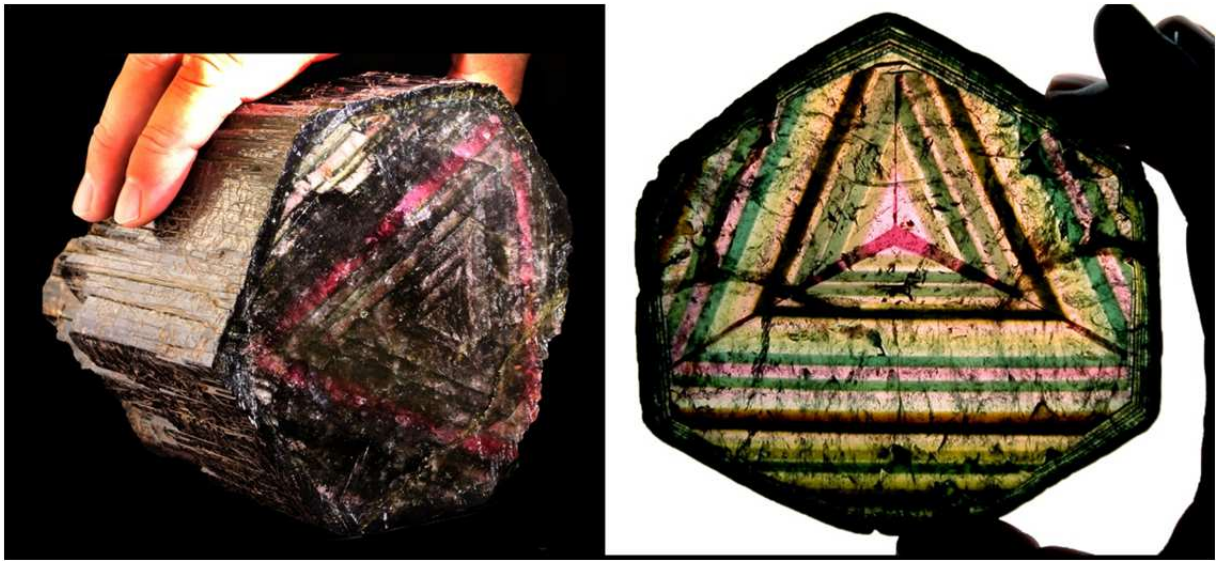

Figure 1. Liddicoatite crystal from Anjanabonoina (Museum MineTech, Paris) and a tourmaline slice from the collection "Das Turmalinzimmer"

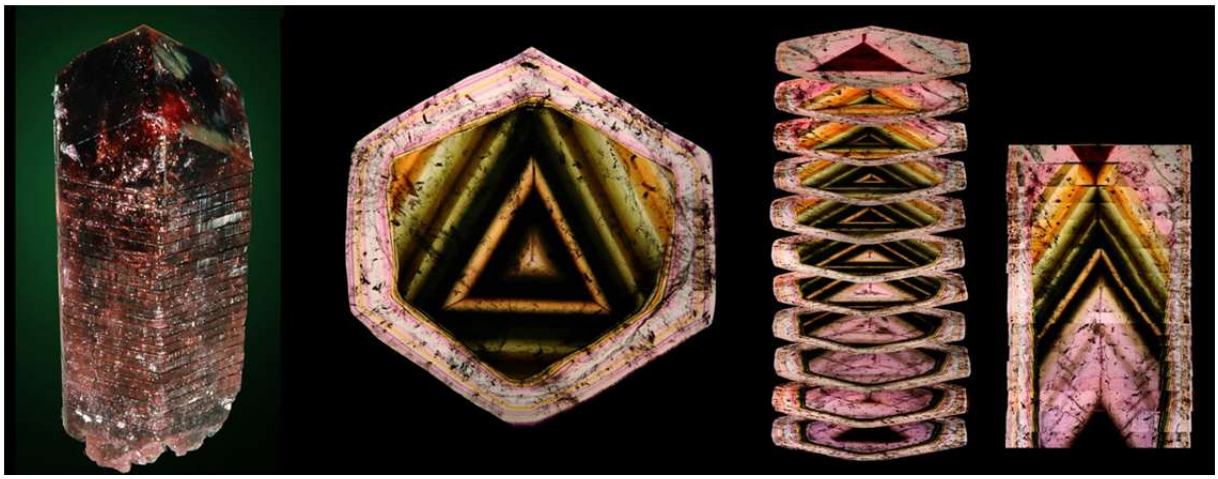

Figure 2. 18 cm-wide Liddicoatite crystal, a slice across the C-axis, a stack of such slices and a stack of stripes from across the center of each slice that mimic a cut along the C-axis; from the collection "Das Turmalinzimmer"

started to study the phenomena in the zoned slices. With his enthusiasm and charisma Benesch motivated numerous people in the anthroposophical community to collect tourmaline slices. And thus he had more and more slices to be studied and documented. The first public highlight of this initiative was the special exhibition at the Munich Show in 1985. Then in 1990 the large sized book “Der Turmalin” by F. Benesch was published. This helped a lot to bring the beautiful phenomena of Madagascar tourmaline to the public awareness.

Some individuals were motivated to collect numerous whole sets of tourmaline slices and to show their collection in public exhibitions. The slices of Dr. Bensech and Dr. Wöhrmann later came to the crystal museum in Riedenburg in Bavaria, and since the end of the 1980s M. Benner`s collection ”Das Turmalinzimmer” and D. Decker`s collection “Turamali” have been shown at mineral fairs and numerous other places.

The attention on the Madagascar tourmaline slices was one motivation to look “deeper” into dark tourmalines, and to grind them thin enough to hopefully find the same structures as in the slices from Anjanabonoina. The color zones in schorl far exceeded expectations: significantly more and new crystallographic phenomena were discovered with outstanding precision and in intense colors. These discoveries were presented in the 2003 Munich show together with slices from Anjanabonoina from the above-mentioned collections. This resulted in a more complete picture of the types of zoning within tourmaline crystals and the phenomena have been published in two books (Rustemeyer 2003 and 2015).

From 2007 on the travelling exhibition “Crystal Magic – fascinating structures in dark tourmaline crystals” combines an aesthetic view on tourmaline slices, crystals and “TourmalineArt” pictures with a holistic view on crystal growth phenomena. By now the exhibition has been shown in more than twenty-five natural history museums in Europe and seen by more than 700 000 visitors.

References

Benesch, F. (1990): Der Turmalin, Stuttgart, 379 p.

Lacroix, A. (1908) Les minéraux des filons de pegmatite à tourmaline lithique de Madagascar, Bulletin de Minéralogie, 1908

Petsch. J. (2015) Madagaskar : Die Wiederentdeckung einer Turmalinmine, Extra Lapis 41, 62 -65

Rustemeyer, P. (2003): Faszination Turmalin, Spektrum Akad. Verl. 2003, 308 p.

Rustemeyer, P. (2015): Tourmaline – Fascinating Crystals with Fantastic Inner Worlds, 272 p.

Ertlite, new tourmaline species with tetrahedral boron from Madagascar and Myanmar

Cempírek, J.*, Skřápková, L., Škoda R.

Department of Geological Sciences, Faculty of Science, Masaryk University, Kotlářská 2, 611 37 Brno, Czech Republic

*Corresponding author: jcemp@sci.muni.cz

Ertlite, ideally $NaAl_3Al_6(Si_4B_2O_{18})(BO_3)_3(OH)_3O$, is a new, very B-rich mineral of the tourmaline supergroup. It was found at two localities; the holotype in the Sahatany Valley, central Madagascar, and a co-type specimen from Sakangyi, Mogok Township, Mandalay Region, Myanmar (Cempírek et al. 2025).

At both localities, the mineral occurs as a late-stage hydrothermal phase in open pockets within highly fractionated, B-rich granitic pegmatites. The holotype occurs as pink to brownish grey or near colorless euhedral crystals and aggregates, up to 10 mm in diameter, associated with béhierite; they are zoned in BSE (Fig. 1), and have variable contents of Li_2O (0.29-0.84 wt.%) and B_2O_3 (13.3-16.53 wt.%). Co-type ertlite forms globular aggregates of white fibrous crystal; it is homogeneous in BSE.

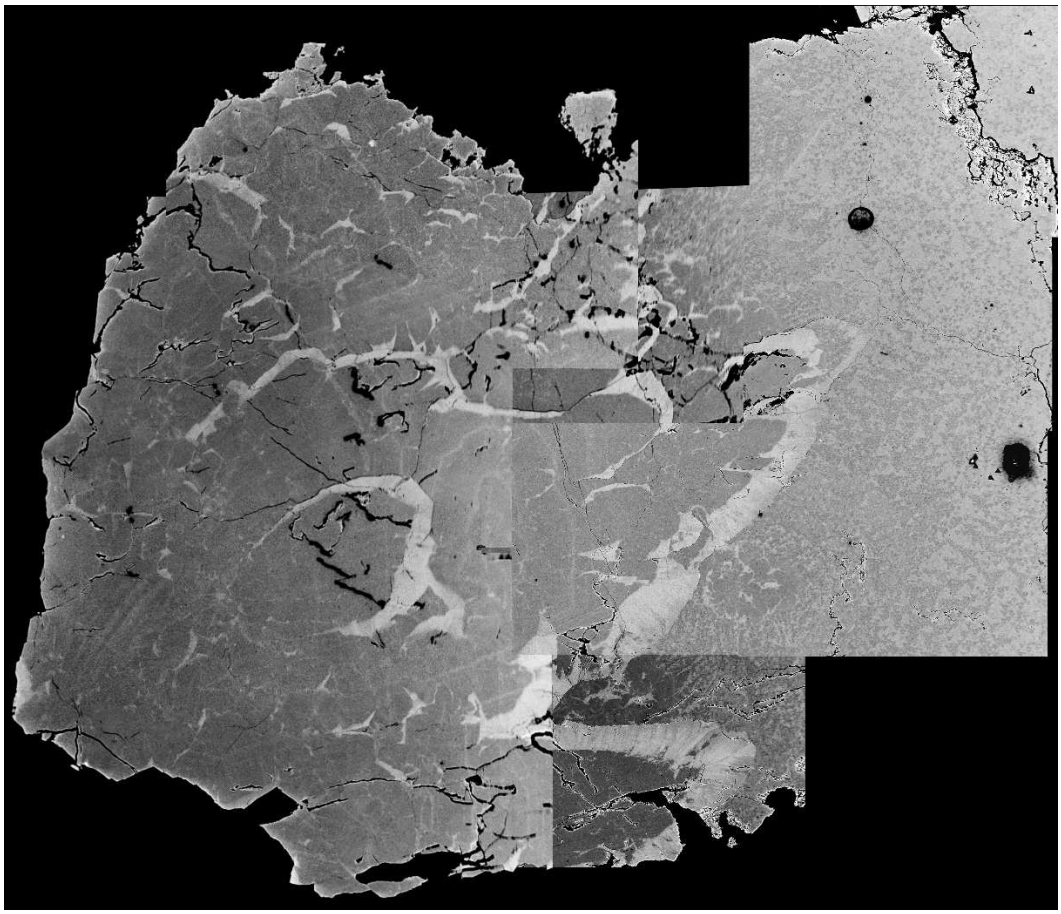

Figure 1: Collage of ertlite BSE images (image width ca. 3.5 x 3 mm).

Ertlite has trigonal symmetry, space group *R*3m, with a = 15.6509(8) Å, c = 7.0406(5) Å, V = 1493.55(19) Å3 (holotype) and a = 15.590(2) Å, c = 7.009(1) Å, V = 1475.3(4) Å3 (co-type, with the lowest unit-cell volume ever recorded for a natural tourmaline); Z = 3.

The crystal structures were refined to R1 = 2.01 % and 3.74 %, respectively, using room-temperature datasets collected with MoKα radiation. Crystal-chemical analysis obtained using electron probe microanalysis, laser ablation inductively coupled plasma mass spectroscopy, Raman spectrometry, and

crystal structure refinement resulted in the following empirical holotype and co-type formulae, respectively (for ordered V and W sites):

$^{X}(Na_{0.573}Ca_{0.220}\ _{0.207})_{\Sigma 1.000}\ ^{Y}(Al_{2.760}Li_{0.187}Mn_{0.051}Ti_{0.002})_{\Sigma 3.000}\ ^{Z}(Al_{6.000})\ ^{T}(Si_{4.526}B_{1.419}Al_{0.055})_{\Sigma 6.000}O_{18}$
$^{B}(BO_3)_3\ ^{V}(OH_{2.857}O_{0.143})_{\Sigma 3.000}\ ^{W}(O_{0.974}F_{0.026})_{\Sigma 1.000}$ (holotype);
$^{X}(Na_{0.743}Ca_{0.109}\ _{0.146}K_{0.002})_{\Sigma 1.000}\ ^{Y}(Al_{2.836}Li_{0.144}Mn_{0.002}Fe_{0.010})_{\Sigma 2.992}\ ^{Z}(Al_{6.000})\ ^{T}(Si_{4.053}B_{1.955})_{\Sigma 6.008}O_{18}$
$^{B}(BO_3)_3\ ^{V}(OH)_{3.000}\ ^{W}(O_{0.716}OH_{0.245}F_{0.039})_{\Sigma 1.000}$ (co-type).

Ertlite is an oxy-species that belongs to the sodic-group of the tourmaline supergroup. Ertlite is an oxy-species that belongs to the sodic-group of the tourmaline supergroup. The closest end-member compositions of valid tourmaline species are: olenite by the coupled substitution $^{T}Si^{4+} + {}^{V}O^{2-} \rightarrow {}^{T}B^{3+} + {}^{V}OH^{-}$ accompanied by the disorder exchange $^{V}O^{2-} + {}^{W}OH^{-} \rightarrow {}^{V}OH^{-} + {}^{W}O^{2-}$, alumino-oxy-rossmanite by the coupled substitution $^{X}\square + {}^{T}Si^{4+} + {}^{T}Al^{3+} \rightarrow {}^{X}Na^{+} + 2({}^{T}B^{3+})$, and darrellhenryite by the coupled substitution $^{Y}Li^{+} + 2({}^{T}Si^{4+}) \rightarrow {}^{Y}Al^{3+} + 2({}^{T}B^{3+})$.
Ertlite was approved by the IMA-CNMNC (IMA 2023-086); the name honors the tourmaline specialist Dr. Andreas Ertl-Winand. Ertlite is closely related to synthetic excess-boron tourmalines.
Holotype ertlite formed during a late stage of open pocket crystallization in a highly fractionated granitic pegmatite dike of lithium-caesium-tantalum-enriched type (LCT-type) of likely Pan-African age. Co-type ertlite crystallized in a very similar pegmatite environment.

References

Cempírek, J., Jonsson, E., Skřápková, L., Škoda, R., Kolitsch, U., Čopjaková, R., Groat, L.A., Kampf, A.R., Lussier, A.J., Hawthorne, F.C., Haifler, J., Holá, M., & Ende, M. (2025). Ertlite, $NaAl_3Al_6(Si_4B_2O_{18})(BO_3)_3(OH)_3O$, a new mineral species of the tourmaline supergroup. *American Mineralogist*; doi: https://doi.org/10.2138/am-2025-9816

Understanding tourmaline growth: A key requirement for meaningful interpretation of tourmaline zoning

Vincent van Hinsberg[1,2,*], Paul Rustemeyer[3], Annabelle Eng[4], Jeanne Paquette[2]

[1] Geotop Research Centre, McGill University, Montreal, Canada
[2] Earth and Planetary Sciences, McGill University, 3450 University Street, Montreal, Quebec, H3A0E8, Canada
[3] Private tourmaline researcher, Waldackerweg 7, 79194 Gundelfingen, Germany
[4] School of the Environment, McGill University, Montreal, Quebec, Canada
[*] Corresponding author: *hinsberg@eps.mcgill.ca*

Tourmaline grains, be they natural or synthetic, display near-ubiquitous colour and compositional zoning. This zoning is of two types: 1. Growth zoning (Fig. 1a), reflecting changes in the physical and/or chemical conditions of its growth environment; and 2. Sector zoning (Fig. 1a,b), which develops as a result of differential element uptake on different growth surfaces. Polar growth, where tourmalines of different composition, shape and colour form by simultaneous growth in different crystallographic directions can be regarded as a variant of sector zoning.

Tourmaline zoning is of great petrogenetic utility. Growth zoned tourmaline grains provide a time series of changing conditions in their growth environment and can therefore be used to track, for example, the evolution of a fractionating igneous body (Lussier & Hawthorne 2011), the changes in conditions in prograde metamorphism (van Hinsberg & Schumacher 2011), or record hydrothermal events and the compositional signature of ore forming fluids (Mlynarczyk & Williams-Jones 2006). Experimental data on the partitioning of major and trace elements between tourmaline and fluid and tourmaline and melt (*e.g.* von Goerne *et al.* 2011) allow for converting qualitative interpretations of compositional zoning to actual fluid and melt concentrations, and the changes therein over time.

Tourmaline sector zoning has similarly found petrogenetic applications. The fractionation of Ca and Ti in polar growth and hourglass sector zoning has been calibrated for use as a geothermometer (Henry & Dutrow 1996; van Hinsberg & Schumacher 2007). This follows from compositional contrasts between sectors decreasing with increasing temperature, as higher vibrational energies decrease sector element specificity. Sector zoning also provides insights into tourmaline crystallo-chemistry. Given that sectors form at the same time in a common environment, the physical and chemical conditions of growth are identical and differences in tourmaline composition therefore directly reflect crystallographic controls. This allows, for example, for identifying the exchange vectors that control element uptake and link surface structure to element preferences (*e.g.,* van Hinsberg & Marshall 2006).

Here, we focus on sector zoning and explore the diversity of sector zoning textures observed in tourmaline, the mechanisms responsible for their formation, and discuss the implications of sector zoning and its formation mechanisms for interpreting tourmaline compositions.

Sector zoning in tourmaline is directly tied to the anisotropy of its crystal structure, which leads to strong differences in the bonding environment exposed on surfaces parallel to its **c**-axis (the *m* and *a* faces) and those at varying angles to **c** (*e.g.* the *r, o, u* and *c* faces). Moreover, the lack of a mirror plane perpendicular to **c** coupled with the 6 tetrahedra all pointing in the same direction produces opposite polar charge in the **-c** and **+c** directions. This results in charge-controlled element fractionation, the intensity of which for any given growth face is directly controlled by its angle to **+c**. However, there are zoning textures in tourmaline that appear to be incompatible with this overall framework. These include so-called delta textures (*cf.* Rustemeyer 2022), as well as sector-like textures in growth zones forming in the **a** - **b** directions (Fig. 2). The latter are particularly difficult to explain as this growth is perpendicular to **c** and therefore not affected by tourmaline's polar properties. Lacking a viable mechanism for their formation, these types of zoning have been interpreted as disequilibrium growth, alteration or replacement. However, the common occurrence and similarities of these textures, their sharp sector contacts and confinement to growth zones (Fig. 2), and compositional systematics between the sectors suggest otherwise. Here, we will argue that all sector zoning textures, including delta textures and *m* and *a* zoning, can be understood from crystal growth mechanisms operating on tourmaline growth

faces and the preferential element uptake that results from the crystal structure exposure of each face. This provides the foundation for meaningful interpretation of tourmaline compositions and zoning.

Henry & Dutrow (1996) Metamorphic tourmaline and its petrologic applications. In Grew & Anovitz, Eds., Boron: Mineralogy, Petrology and Geochemistry 33, 503–557.

Lussier & Hawthorne (2011) Oscillatory zoned liddicoatite from Anjanabonoina, central Madagascar. II. Compositional variation and mechanisms of substitution. Canadian Mineralogist 49, 89-104.

Mlynarczyk & Williams-Jones (2006) Zoned tourmaline associated with cassiterite: implications for fluid evolution and tin mineralization in the San Rafael Sn–Cu deposit, Southeastern Peru. Canadian Mineralogist 44, 347-365.

Rustemeyer (2022) The inner architecture of tourmaline crystals, as inferred from the morphology of color zones in thin slices. Journal of Geosciences 67, 103-128.

van Hinsberg & Marschall (2006) Boron isotope and light element sector zoning in tourmaline: Implications for the formation of B-isotopic signatures. Chemical Geology 238, 141-148.

van Hinsberg & Schumacher (2007) Intersector element partitioning in tourmaline: a potentially powerful single crystal thermometer. Contributions To Mineralogy and Petrology, 153, 289–301.

van Hinsberg & Schumacher (2011) Tourmaline as a petrogenetic indicator mineral in the Haut-Allier metamorphic suite, Massif Central, France. Canadian Mineralogist 49, 177-194.

von Goerne, Franz & van Hinsberg (2011) Experimental determination of Na–Ca distribution between tourmaline and fluid in the system $CaO–Na_2O–MgO–Al_2O_3–SiO_2–B_2O_3–H_2O$. Canadian Mineralogist 49, 137–152.

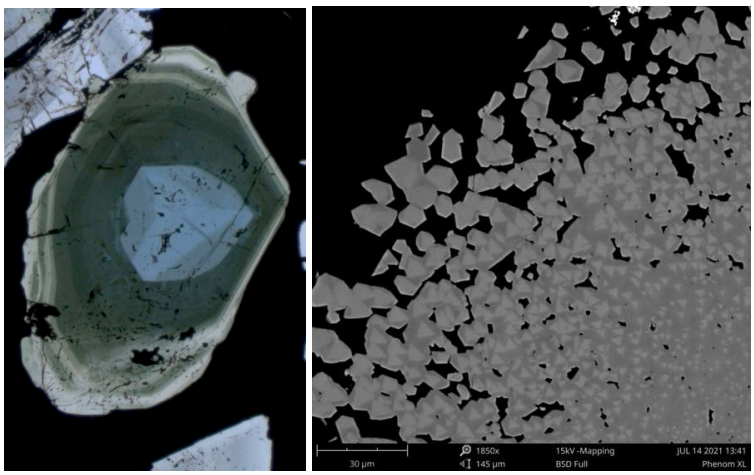

Fig 1 a. Concentric growth zoning in the a-sector olive-green mantle and rim of a tourmaline from a sulfidic ore deposit. The blue core represents the c^+-sector and contains further sector zoning in lighter and darker shades of blue. b. Triangular sector zoning in Fe-rich tourmaline synthesized at 600˚C and 200 MPa.

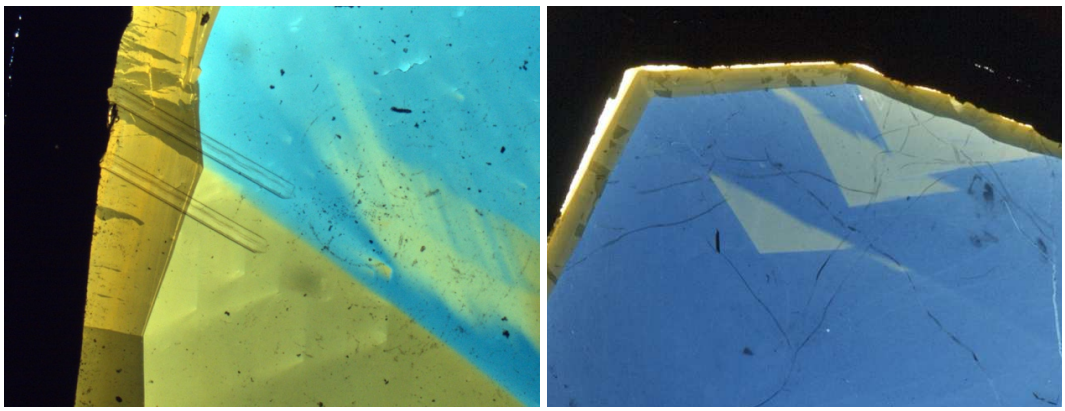

Fig. 2 Brown delta features in the blue c+-sector core of igneous tourmalines and patchy light and dark brown zoning in its a-sector rim. Delta and a-sector zoning boundaries connect at the core-rim interface. The faint lines in the left image are laser ablation troughs.